LOW-DIMENSIONAL TRANSITION METAL CHALCOGENIDES FOR ELECTRONICS APPLICATIONS

by

MATTHEW A. BLOODGOOD

(Under the Direction of TINA SALGUERO)

ABSTRACT

The chemistry and structure of low-dimensional materials are an important consideration for nanoscale, electronics applications. The oxidative chemistry of 2-dimensional 1*T*-$TiSe_2$ and 1*T*-$TaSe_2$ is explored in chapter II. Oxidation onset temperature, oxide layer thickness, and polymorph transitions associated with prolonged, ambient storage are discussed. The oxidative stability of 1*T*-$TiSe_2$ was found to be lower than that of 1*T*-$TaSe_2$ with each material reaching full oxidation at 400 and 600 °C after 1 h, respectively. A phase transition in $TaSe_2$ after prolonged storage in ambient conditions inspired further study of polymorphism. Investigation of the polymorphic, transitional pathways of 1*T*-$TaSe_2$ in chapter III revealed two previously unreported transitions. The first is a transition to the room temperature stable phase from 3*R* to 2*H*-$TaSe_2$, followed by a transition to the metastable 4*H*(*x*) polymorphs (*x* = *a* or *c*). Polymorphism investigation is continued with the study of the NbS_3 system described in chapter IV. Two newly established polymorphs of NbS_3, along with high-resolution characterization, are reported. These studies are integral advances in knowledge for the advancement of nanoscale electronics.

INDEX WORDS: transition metal dichalcogenide, transition metal trichalcogenide, chemical vapor transport, polymorphism, polytypism, niobium trisulfide, tantalum diselenide, titanium diselenide

LOW-DIMENSIONAL TRANSITION METAL CHALCOGENIDES FOR ELECTRONICS APPLICATIONS

by

MATTHEW A BLOODGOOD

BS, Clemson University, 2010

A Dissertation Submitted to the Graduate Faculty of The University of Georgia in Partial Fulfillment of the Requirements for the Degree

DOCTOR OF PHILOSOPHY

ATHENS, GEORGIA

2018

LOW-DIMENSIONAL TRANSITION METAL CHALCOGENIDES FOR ELECTRONICS APPLICATIONS

by

MATTHEW A BLOODGOOD

Major Professor:	Tina Salguero
Committee:	John Stickney
	Jin Xie

Electronic Version Approved:

Suzanne Barbour
Dean of the Graduate School
The University of Georgia
May 2018

DEDICATION

This work is dedicated to my loving family whose unwavering support has brought me through this journey. This is dedicated to my wife, Jenny, as she will always be to me. To my mom and Dad, who have far more confidence in me than me and inspire me to work harder. To my brothers, for being there for us when we needed them most. To my wife's parents, for their support and assistance whenever we needed it. To my extended family, for helping during my time at Emory without a second thought. To the Liver and Kidney Transplant Teams at Emory Hospital, for bringing me back from the brink and then working with me through the rest.

Lastly, most importantly (and again) this is dedicated to you Jenny. The one who inspires me every day. Inspires me to work harder and be a better me. Inspires me to think more, be humble, and be cognizant of others.

ACKNOWLEDGEMENTS

I would like to first acknowledge my family and their support throughout grad school, trying to keep my hopes up when things got tough. A special thank you to my mom, dad, brothers, mother- and father in-laws, and, especially, my wife for their unwavering support. I would like to acknowledge my fellow graduate students in the Salguero lab for helping me through my time at UGA. More specifically, I would like to acknowledge specific individuals for guidance and general help around lab including: Tim Pope, Matt Davidson, Darrah Johnson-McDaniel, Roshini Ramachandran, Greg Neher, Nick Nguyen, and Yassamin Ghafouri. A special shout-out goes to Yassamin for asking as many questions as possible, keeping me on my toes. I would also like to acknowledge my advisor for her unwavering interest in the accurate pursuit of knowledge. Without her penetrating questions, I would have flagged and wavered.

Lastly, I would like to acknowledge all those who supported me through the dark time that was the Fall of 2013. Acknowledging my new group mates (Tim, Matt, Darrah, Roshini, Greg) for their help while I was relegated to the hospital even though they barely knew me. In addition, the liver transplant team at Emory is also acknowledged here for bringing me back and keeping me amongst the living.

TABLE OF CONTENTS

Page

CHAPTER 1

INTRODUCTION AND LITERATURE REVIEW

Nanomaterials

Current, societal advancement depends heavily on contemporary innovations in technology. Technology is prevalent throughout our everyday lives, ranging from travel to health to the distribution and dissemination of knowledge. Many of the technological achievements are concerned with the optimization of speed versus size. As our devices continue to decrease in size, technological evolution reaches an impasse where new materials are required in place of further engineering. Scientists and engineers thus have turned to the field of nanomaterials to solve the minimization hurdle. As technological improvements move electronics further into the nanoscale regime, new materials will be required for continuing progression.

According to the National Institute of Environmental Health Sciences, nanomaterials are considered to be any material that has at least one spatial dimension less than 100 nm in length.[1] Nanomaterials can be found in a variety of sizes, shapes, and dimensionalities. There are four general classifications for nanomaterials: zero-dimensional (0D) structures, such as quantum dots, one-dimensional (1D) rods and wires, two-dimensional (2D) nanosheets and ribbons, and three-dimensional (3D) particle-like structures. Nanoscale dimensionalities can be seen in the general representations in Figure 1.1. Incredibly, the physical, electronic, and optical properties of a material can change as the shape and/or size varies from bulk to lower dimensionality.[2] This phenomenon is evident in a multitude of different materials, including the renowned examples of

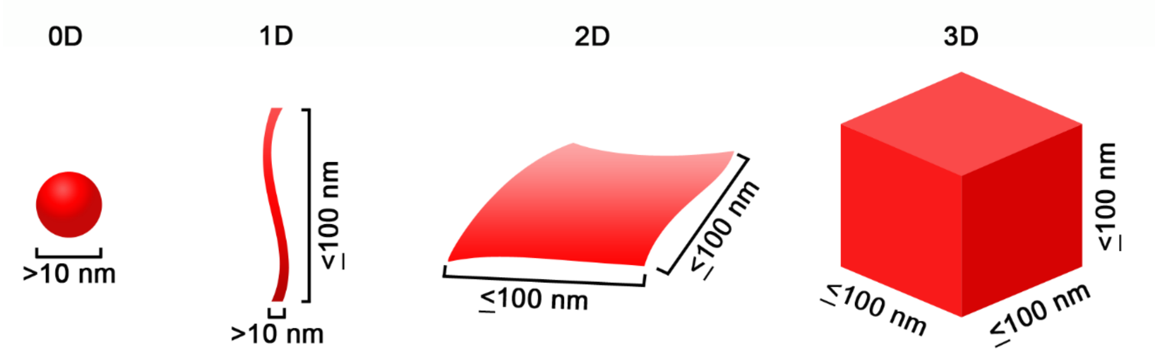

Figure 1.1 General depictions of nanoscale dimensionality as represented by a quantum dot (0D), nanowire (1D), nanosheet (2D) and a cubic particle (3D).

gold and graphene. Graphene, arguably the most widely studied two-dimensional material, is a layered van der Waals material that can be mechanically exfoliated from bulk graphite by methods as simple as layer removal with clear tape; this method can produce monolayer graphene.[3] As graphite is reduced to single layer graphene, the electrical and thermal conductivity significantly increase resulting in an atomically thin conductor.[4-5] Gold is another example of a material with anomalous properties as particle size decreases. The intriguing surface plasmon resonance and optical properties have been well documented, revealing a distinct relationship between particle radius and absorption wavelength.[6] Plasmonic nanoparticles, such as gold, have recently been popularized for use in medical applications like cholesterol sensing,[7] drug delivery,[8] and cancer treatment.[6, 9]

Another important phenomenon associated with low-dimensional (1D and 2D) materials is the presence of charge density waves (CDWs). Charge density waves have been known for many years; however, only recently have we been able to study atomic phenomena such as CDWs with high resolution techniques.[10] They are an intriguing phenomenon occurring in a variety of materials, especially low-dimensional materials,[10] including blue bronzes,[11-12] metal chalcogenide halides,[12] and transition metal di-[13-14] and trichalcogenides.[12, 15] A CDW is a periodic modulation of electrons which creates standing waves of charge throughout a material. These standing waves of charge can be accompanied by modest structural distortions resulting in what is known as a Peierls distortion, which can significantly affect the electrical conductivity.[12, 16] A material can exhibit multiple degrees of CDW commensuration resulting in up to three distinct phases. These phases are temperature-dependent and are classified as commensurate (C), nearly commensurate (NC), or incommensurate (IC).[17-18] An illustration of these CDW phases in $NbSe_2$ can be seen in Figure 1.2a. A C-CDW phase is indicative of a complete, unbroken CDW throughout an entire material, not merely a single or surface layer. In transition metal dichalcogenides specifically, CDWs are accompanied by lattice distortions forming 12-pointed stars with a thirteenth metal atom at the center of each star where the cumulative charge collects.[13, 17-18] Both the NC- and IC-CDW phases result from increasing degradation of the cohesive standing wave in the C-CDW phase. The NC-CDW phase contains C-CDW pockets surrounded by the incommensurate metallic phase,[17] whereas the IC-CDW phase lacks periodicity that is commensurate with the underlying lattice.[15, 19] For example, the lattice vectors in the IC-CDW phase of 1*T*-$TaSe_2$ undergo a reduction of the supercell, but also a nearly 14° rotation.[18] An STM image of the NC-CDW phase of $NbSe_2$ can be seen in Figure 1.2c. Beyond these three CDW phases, a high temperature metallic phase exists with no charge density modulations or lattice distortions. All of these phases can be obtained through temperature variation with the C-CDW being at low temperatures and the metallic phase at high temperatures.[12] Additionally, CDWs can be forced to flow through a material with the application of a voltage, resulting in interesting charge transport phenomena. A high-quality sample, however, is needed for unimpeded charge transport because CDWs have been shown to pin to defects and vacancies in the crystal lattice.[12]

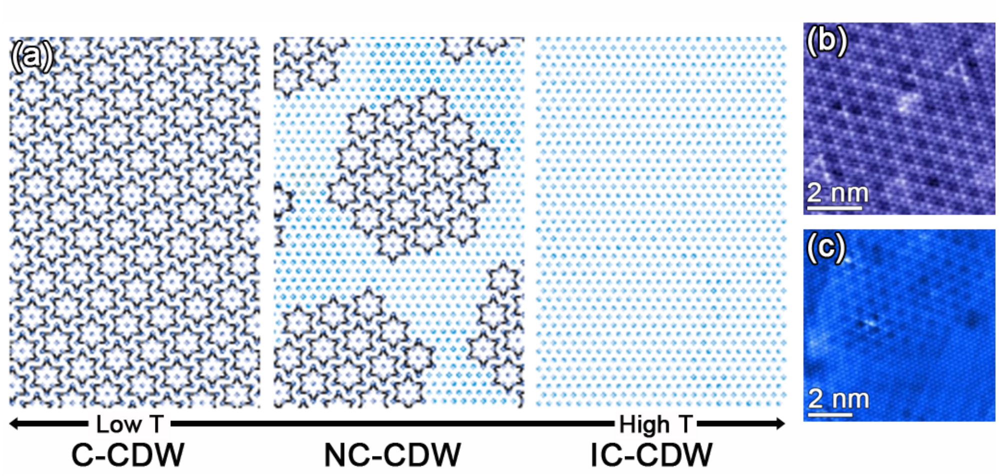

Figure 1.2 (a) Illustration of the three charge density wave states: commensurate (C-CDW), nearly commensurate (NC-CDW), and incommensurate (IC-CDW). [Adapted from 17]. Scanning tunneling microscopy images of the (b) C-CDW and the (c) NC-CDW of $NbSe_2$. [Adapted from http://hoffman.physics.harvard.edu/].

Many low-dimensional materials present interesting properties as the nanometer scale is achieved, which has led to the discovery of important solid-state physics phenomena. These phenomena allow for property tuning in materials, making them ideal for nanoscale devices.[12, 20-21] Monolayer graphene-based, low-dimensional devices have been thoroughly studied for various transistor applications[22]; however, monolayer graphene presents several issues for device implementation. For a device such as a logic gate, a degree of semiconductivity is necessary to obtain both the ‘on’ (conducting) and ‘off’ (insulating) states, which cannot be achieved by graphene due to its metallic nature.[22] Transition metal chalcogenide materials are one solution to the dimensional and electrical hurdles posed by the technological march of progress.[14] These materials can be synthesized through several methods utilizing either a top-down or bottom-up approach.

The approach used for this work concentrated on the bottom-up method known as the chemical vapor transport (CVT) method. This method utilizes a volatile complexing agent known as a transport agent, together with a fixed temperature gradient, to grow up to cm-sized, bulk crystals.[18] Transport agents include a variety of materials and compounds including halogens, chalcogens, and volatile metal halides.[23] Of these, iodine is most commonly used for both the transition metal di- and trichalcogenides.[24] This method also presents some starting material versatility, in that high purity elements or a pre-formed material can be transported for crystal growth.[25] In a CVT reaction, the starting materials are commonly placed in the higher temperature zone known as the 'source' zone. During heating, the transport agent volatilizes to the vapor phase where complexation with the starting materials occurs. The newly formed, volatile complexes then transport through diffusion toward the lower temperature, 'growth' zone where reaction of the starting materials results in the crystal growth.[24] Figure 1.3 shows a simple schematic of a CVT

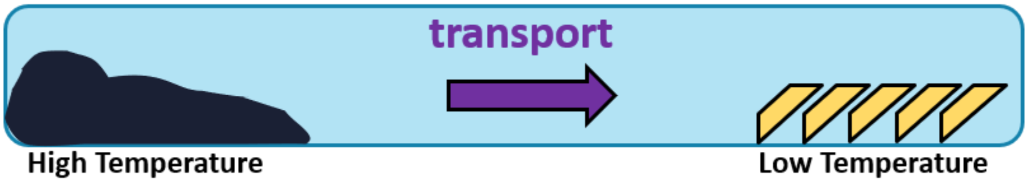

Figure 1.3 Schematic of chemical vapor transport reaction. The starting materials are represented on the left in the high temperature "source" zone. After transport agent complexation, the starting materials are transported to the cooler "growth" zone represented by the golden plates on the right.

process. This method has been thoroughly proven to produce high quality crystals for a variety of materials in relatively high yield, including halides, chalcogenides, nitrides, and others.[25]

Overall, low-dimensional materials present a viable solution to the continuing miniaturization of technology. Growth of high-quality, crystalline materials, along with improving manipulation techniques, permit usage in future electronics that require increasing power-to-size ratios and decreasing application size. Future applications hinge on the anomalous properties observed in a wide range of materials, i.e. graphite, gold, blue bronzes, and transition metal chalcogenides, as their size is decreased to the nanoscale, or to a monolayer in the case of layered materials. Device evolution may harness the CDW, unique electrical, and anomalous optical properties observed in low-dimensional materials for future electronics applications.[26]

Transition Metal Dichalcogenides

Transition metal dichalcogenides (TMDs) are a class of 2D, van der Waals materials containing a transition metal and chalcogenide, specifically S, Se, or Te. To date, there are numerous TMDs reported in the scientific literature that most commonly contain the early transition metals; some of the more well-known TMD materials include MoS_2, TaS_2, WSe_2, $NbSe_2$, and $TiSe_2$.[14] MoS_2 is arguably the most widely studied TMD with an extensive literature base beginning in the 1940's; it has been used as a solid lubricant in tribological applications since that time.[27-28] Recent technological breakthroughs and discoveries, i.e. the discovery of monolayer graphene, however, have caused a resurgence of interest in TMDs due to their unique structural and electronic properties.[2] Much like graphene, many TMDs possess thickness dependent property variation, such as charge density wave behavior,[16, 29] conductivity,[2, 16] and bandgap.[2, 30] Transition

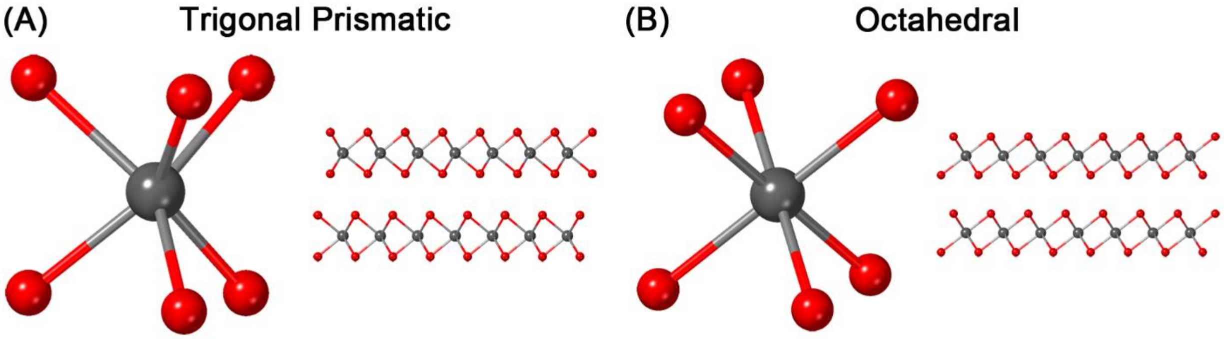

Figure 1.4 The two metal coordination geometries observed in transition metal dichalcogenides: (A) trigonal prismatic coordination, and (B) octahedral coordination geometry. The metal atoms are shown in gray, while the chalcogen atoms are represented by the red atoms. Each coordination is also represented within their respective layers.

metal dichalcogenides exhibit a range of electronic properties resulting in materials ranging from small band gap semiconductors (MoS_2, WSe_2) to irregular semimetals (TiS_2 and $TiSe_2$) to metallic-like conductors (VS_2, $NbSe_2$, TaS_2).[14] The wide array of electronic properties is a direct result of the composition, structural arrangement, and metal coordination environment.

The class of materials that is TMDs is broadly defined by their general structure consisting of six-coordinate metal layers in an X-M-X arrangement, where X represents a chalcogen and M the transition metal.[18] Structural layers are held together by relatively weak van der Waals forces which span a nearly 3 Å gap between layers, i.e. the van der Waals gap, as estimated from the crystal structures.[31] The transition metal atoms in TMDs can be found in one of two coordination geometries: trigonal prismatic or octahedral; these two coordination geometries can be seen in Figure 1.4. In both coordination geometries, the transition metal is surrounded by six chalcogen atoms resulting in layers of contiguous, MX_6 units. The six-coordinate metal atoms for all the transition metal dichalcogenides with this structure are found as M(4+) as found in x-ray photoelectron spectroscopy (XPS) studies.[32-33] Often, only a single metal coordination is found in each TMD crystal; however, both geometries have been found within the same TMD crystal as alternating layers, e.g. in 6*R*-$TaSe_2$.[34] Although this type of mixing has been reported, there have not been reports on mixed metal coordination geometry within a single layer even when doping with another transition metal.[35] The available diversity in coordination geometry, in addition to layer stacking variability, result in the rich polymorphism observed throughout the TMD systems.

The layers can be arranged in various ways resulting in several structurally distinct variations known as polymorphs and polytypes. Although these two terms are often used interchangeably, they are distinctly different. Polymorphism is generally defined as a complete structural change of a material, while polytypism, a subset of polymorphism, is a structural rearrangement within a material, i.e. global variation versus local variation. $CaCO_3$ is a quintessential example of polymorphism possessing multiple observed phases (calcite, aragonite, vaterite) with varied structures, but the same formula unit.[36] Conversely, polytypism is observed in many layered materials through a simple change in layer stacking order. SiC, for example, exhibits extensive polymorphism and polytypism with layer variation as well as stacking variation.[37] Polymorphism in many layered materials, including TMDs, is now represented using Ramsdell notation. Ramsdell notation was introduced to simplify and standardize the nomenclature of SiC which has prolific polymorphism.[37] Phases designated using Ramsdell notation include a number-letter combination that refers to specific details pertaining to the unit cell, e.g. 3*C*, 4*H*, 6*R*. The number represents the formula units found in the unit cell, while the letter represents the observed symmetry (*C* = cubic, *H* = hexagonal, *R* = rhombohedral).[37] For example, 3*C*-SiC contains three formula units with cubic symmetry in the unit cell. Thus, highly polymorphic systems can easily account for not only structural layer variations but also stacking order variation. Depending on the arrangement of layers, numerous variations can be obtained, e.g. 1*T*, 4*H*, 6*R*, 13*H*, etc, resulting in rich polymorphic systems.[31]

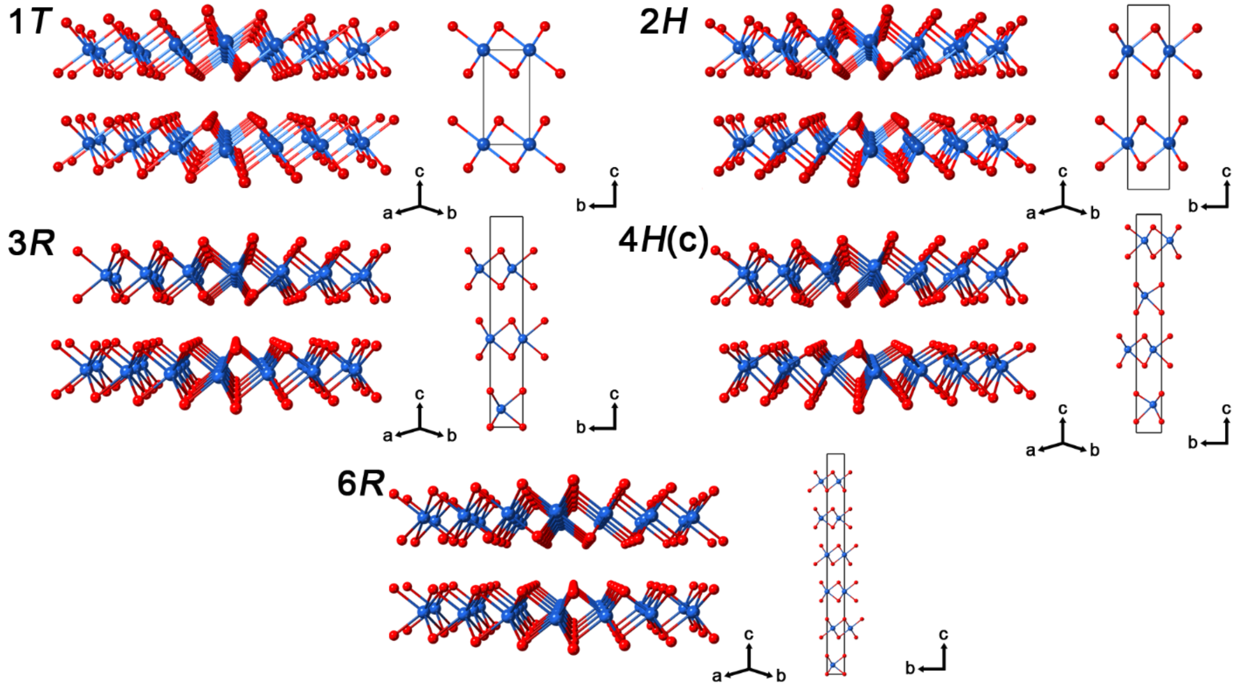

Figure 1.5 The five most common polymorphs observed for the $TaSe_2$ system are shown. Each polymorph is represented by a (111) perspective view showing two selected layers of the unit cell, and a (100) view of the unit cell revealing the stacking order within each unit cell. Only whole formula units are shown in each unit cell. The Ta atoms are shown as blue, and the Se atoms as red.

$TaSe_2$ is an excellent example of a rich polymorphic system. In $TaSe_2$, numerous polymorphs are known, including the 1*T*, 2*H*, 3*R*, 4*H*, and 6*R* phases; however, the most commonly observed phases are the 1*T*, 2*H*, and 3*R* polymorphs.[31] The five phases of $TaSe_2$ can be seen in Figure 1.5 illustrating the structural variations between polymorphs. 1*T*-$TaSe_2$ is unique among the known $TaSe_2$ polymorphs because it is the only polymorph to exclusively contain the octahedral metal coordination. Additionally, alignment of the Ta atoms of each progressing layer leads to the most compact $TaSe_2$ unit cell. These features are true of all other 1*T*-MX_2 structures, as exemplified by the 1*T* Ti, Zr, and Hf TMDs. This coordination also appears in specific polymorphs of other TMDs, such as 1*T*'-WTe_2 and 1*T*-MoS_2.[38] Except for the group 4 TMDs, the 1*T* polymorph is a metastable phase achieved through temperature modulation or intercalation.[18, 31, 38] At room temperature, many TMDs are found in a trigonal prismatic phase which includes the 2*H*, 3*R*, and 4*H* phases, shown in Figure 1.5. These phases differ simply by variations in stacking order resulting in extended unit cells.[31] The polymorphism in $TaSe_2$ continues beyond these single metal-coordination phases with phases containing alternating geometries. For example, 4*H*(b) and 6*R*-$TaSe_2$ both contain alternating octahedral and trigonal prismatic layers (Figure 1.5).[39] The alternating layer configuration found in these phases is highly irregular and only found in the $NbSe_2$, TaS_2, and $TaSe_2$ system.[31]

Amazingly, the slight structural changes associated with polymorphism in TMDs has a profound effect on the electronic properties. Property variation between polymorphs is prominent in the TaX_2 systems, where X = S or Se. Both TaS_2 and $TaSe_2$ are found in the silver/black 2*H* phase at room temperature but transform to the golden 1*T* phase at high temperature, i.e. > 850 °C.[31] Not only does the electronic structure change resulting in the observed color change, but some properties vary as well. For example, 1*T*-TaS_2 passes through three CDW transitions: the first at 180 K from C-CDW to NC-CDW, then at 350 K from NC-CDW to IC-CDW, and finally at 550 K from IC-CDW to the metallic phase.[16, 40] In contrast, 2*H*-TaS_2 experiences only two CDW transitions from a C-CDW to IC-CDW phase at 90 K, and then from the IC-CDW phase to the metallic phase at 123 K.[40] Magnetic susceptibility varies between polymorphs of $TaSe_2$, where 1*T*-

$TaSe_2$ is diamagnetic and the 2*H*, 3*R* and 4*H*(a) phases are all paramagnetic.[41] Molybdenum ditelluride is another excellent example of this phenomenon. $MoTe_2$ is commonly found in the stable, 2*H* polymorph but transforms to 1*T*-$MoTe_2$ upon heating above 900 °C.[42] This transformation is accompanied by a decrease in electrical resistivity, resulting in metallic conductivity.[43]

Compositionally, the choice of transition metal and the chalcogenide can have a profound effect on the electrical properties of the TMD. Property variation with chalcogen exchange is most prominent in the group IV and VI TMDs. Many of the disulfides and diselenides are small bandgap semiconductors, including those of Zr, Hf, Mo, and W, whereas some of the corresponding ditellurides act as metallic or semimetallic conductors. For example, both WS_2 and WSe_2 are semiconducting materials with band gaps ~ 1 – 2 eV;[44-45] however, WTe_2 has been found to be semimetallic.[14] This is also the case for Hf and Mo where two of the $MoTe_2$ polymorphs, β and T_d-$MoTe_2$, are metallic whereas the third, α-$MoTe_2$, is a semiconductor.[42, 46-47] Interestingly, the Ti-based TMDs are the exception in group IV and show more metallic character in both the diselenide and ditelluride, with TiS_2 being the only semiconductor.[14] Both Nb and $TaTe_2$ have been reported to be metallic, matching the analogous disulfides and diselenides.[48] Substituting the transition metal also has a similar effect even within the same group; the group 4 TMDs are an archetypal example of this phenomenon. The diselenides of both Zr and Hf are known to be indirect bandgap semiconductors,[14] whereas $TiSe_2$ is considered as semimetallic, although the true nature of $TiSe_2$ is still being debated.[49] Transitioning from group 4 to 5 to 6, a general trend arises for electrical conductivity. In general, the group 4 and 6 TMDs are semiconductors when observed in their room-temperature-stable polymorphs, e.g. 1*T*-ZrS_2, 1*T*-$HfSe_2$, 2*H*-$MoSe_2$, and 2*H*-WS_2.

In contrast, the group 5 TMDs, including VX_2, NbX_2, and TaX_2, are metallic throughout their polymorph ranges.[14]

Much like other low-dimensional materials, the electrical properties in transition metal dichalcogenides can be tuned with decreased layer thickness.[29] Monolayers of various TMDs have been observed after growth by chemical vapor deposition.[50] However, crystal growth by CVT requires a paring down, or exfoliation, of the bulk material. Much like in the case of graphene, exfoliation techniques have been developed and demonstrated for a variety of TMDs.[40, 51] The most simple method of exfoliation is mechanical exfoliation which consists of physically removing TMD layers, the most popular technique utilizes layer removal by adhesive tape.[52] Using this method, one can achieve TMD flakes that are down to a monolayer in thickness.[53] This method, however, results in a variety of observed TMD thicknesses and sizes, which has led to the development of liquid-based methods. There have been several liquid exfoliation studies including techniques including like chemical intercalation,[54] electrochemical means,[55] as well as exfoliation by agitation in simple solvents.[56] The described exfoliation techniques have led to the significant property discoveries and brought attention back to TMDs and low-dimensional materials in general.

Transition Metal Trichalcogenides

Due to their renown, many parallels are drawn between the transition metal di- and trichalcogenides, however, there several differences as well. Like transition metal dichalcogenides, the transition metal trichalcogenides (TMTs) are a class of layered, van der Waals materials considered to be quasi-1-dimensional in nature.[12, 57] This considered pseudo-dimensionality is a direct result of the unique, interchain interactions in the chain structure that defines the material class.[12] The transition metal di- and trichalcogenides also share a similar history in that both have been studied over the past 50 or more years, but have experienced a strong resurgence in interest over the past decade or so.[27, 40, 57-58] Many of the properties observed in TMDs can also be found in TMTs, including metallic-like conductivity, charge density waves, and superconductivity.[12, 15, 57] However, the similarities between these two material classes begin to diverge when considering general structures and dimensionality.

Both classes of materials are composed of MX_6 units (M = the transition metal and X = chalcogen), but where TMDs are composed of layers of edge-shared MX_6 units with two possible metal coordination geometries, TMTs consist of face-sharing, MX_6 units arranged into infinite chains, i.e. a theoretical 1D structure. Additionally, the TMTs contain only one metal coordination geometry, trigonal prismatic.[12] The TMT chain structure can be seen in Figure 1.6. These infinite

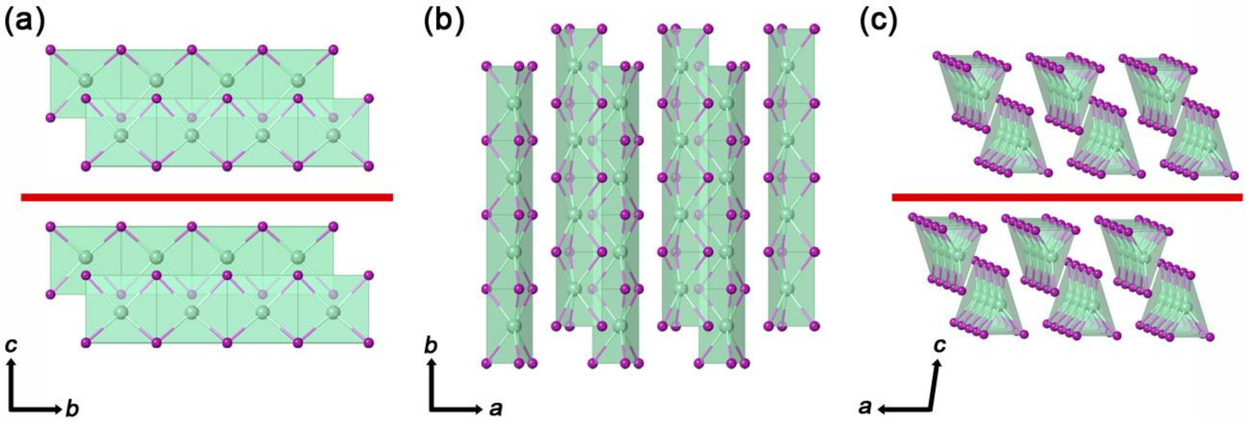

Figure 1.6 Three views of the $ZrSe_3$ crystal structure. The layered nature of the transition metal trichalcogenides is clearly demonstrated when viewed down the a-axis (a), while the chain structure is demonstrated when viewed down the c-axis (b) or with a perspective view (c). The van der Waals gap is also visible in (a) and (c) between the layers of chains as indicated by the solid, red lines.

chains can be found arranged into three general orientations: the $ZrSe_3$-, $TaSe_3$- and $NbSe_3$-type structures; these designations originate from the first material for which each respective structure was solved.[15] Each of the known transition metal trichalcogenides has been found in only one of these structural orientations. Table 1.1 contains the known TMTs and their general structures, which indicates that most of these materials are found in the $ZrSe_3$-type structure. The group 5 transition metal trichalcogenides are found in either the $TaSe_3$ or $NbSe_3$ structures, with NbS_3 being the exception to this trend.

Table 1.1 The known transition metal trichalcogenides categorized by the general structure types, $ZrSe_3$, $TaSe_3$, and $NbSe_3$. The tantalum trichalcogenides and $NbSe_3$ are the structural exceptions being found in the $TaSe_3$-type ($TaSe_3$) or $NbSe_3$-type (TaS_3, $NbSe_3$) structures.

Structure	$ZrSe_3$[59]	$TaSe_3$	$NbSe_3$
Material	TiS_3, ZrS_3, $ZrSe_3$, $ZrTe_3$, HfS_3, $HfSe_3$, $HfTe_3$, NbS_3[60]	$TaSe_3$[61]	TaS_3,[62] $NbSe_3$[63]

The three general structure types are differentiated from one another by the variation in the number of ‘chain types’ within the unit cell, where the $ZrSe_3$-type contains one, the $TaSe_3$-type contains two, and the $NbSe_3$-type contains three ‘chain types’. Figure 1.7 shows the three general structures and illustrates chain type variation with the three, color-coordinated chains from $NbSe_3$. Each ‘chain type’ is defined by the shortest X-X distance of the cross-sectional MX_6 trigonal prisms of the MX_3 chains. These chalcogen pairing distances are short enough that Krönert and Plieth anticipated selenium-selenium bonds in $ZrSe_3$ in 1965.[64] Simultaneously, Bjerkelund and

Kjekshus reported similar bonding in $TaSe_3$; however, confusion arose when calculating the 'general (8 – N) rule', which involves valence, crystal structure features, and electrical properties like conductivity.[61] It was originally thought that the group 5 transition metals would ionize predictably, producing a valence of 5.[65] Later XPS studies confirmed the presence of chalcogen bonds, revealing chalcogen pairs with a (2^-) charge, $(X_2)^{2-}$.[66-67] It was further shown that the group 5 transition metals formed a $4d^1$ electron configuration resulting in a M^{4+} oxidation state,[12, 66, 68] an idea first proposed for NbS_3 due to its close structural relation to $ZrSe_3$, the only group 5 TMT to be found with that structure.[60] The formula for all of the transition metal trichalcogenides was then widely accepted as $(M)^{4+}(X)^{2-}(X_2)^{2-}$, which maintained charge neutrality yet incorporated all the atoms that create the unique chain structure.

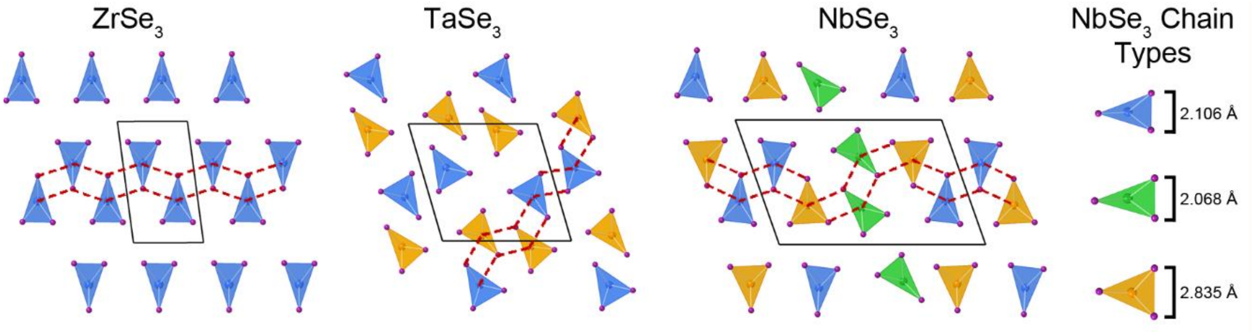

Figure 1.7 The three general structures of transition metal trichalcogenides ($ZrSe_3$, $TaSe_3$, and $NbSe_3$) showing a single unit cell and surrounding chains. The chain colors within each unit cell represent the different chain types. The three chain types for the $NbSe_3$ structure are also defined at right. The X-X distance in each type of chain depends upon both the metal and chalcogen atoms.

The infinite chains of the transition metal trichalcogenides are arranged in layers formed from the strong interchain forces between neighboring chains, resulting in a transition metal coordination of 8 rather than 6.[12, 61] These layers create the van der Waals gaps of the material,[69] see Figure 1.7. Exfoliation along these gaps can result in a morphology that is more 2D nature[12] than the anticipated 1D morphology by a cursory inspection of the crystal structure. Many TMTs are found to form in morphologies somewhere between true 1D and 2D materials resulting in this class being designated as "quasi-1D" materials. This quasi-one-dimensionality is observed as very high aspect ratio morphologies including nanoribbons and wires that can range from a few nanometers to ~100 μm in width and up to several centimeters in length. Bulk transition metal trichalcogenides are synthesized under similar conditions to those used for the creation of bulk TMD crystals as mentioned earlier. Chemical vapor transport is most commonly used for bulk crystal growth utilizing a variety of transport agents including excess chalcogen, chalcogen chlorides, and halogens, with iodine being the most common. Crystals are commonly grown directly from the high purity elements at temperatures generally lower than the corresponding TMDs.[23] With increased temperature, the transition metal trichalcogenides begin to diverge from the MX_3 stoichiometry by a loss of chalcogen, resulting in degradation to the corresponding dichalcogenide.[23, 70] Synthetic conditions are also an important factor when considering the purity and ending polymorph of the desired TMT.

Unlike the transition metal dichalcogenides, there are only a few TMTs known to exhibit polymorphism. The niobium and tantalum trisulfides are great examples of this polymorphism revealing at least two distinct phases each. For example, tantalum trisulfide has been found in two different polymorphs: a monoclinic phase,[62] and an orthorhombic phase.[65] Astoundingly, TaS_3 has recently been reported exclusively in the orthorhombic phase, when a mixture of phases was originally reported.[15] This has raised the question of the "disappearing polymorph" phenomenon famously seen in pharmaceutical court proceedings.[71] Polymorph isolation, however, remains a significant crystal growth hurdle due to the overlapping growth conditions.[72] This is similar to the 2*H* and 3*R* polymorphs of $TaSe_2$ where both polymorphs can be found in very similar growth conditions with the 2*H* phase being the predominantly isolated phase.[31] For the niobium and tantalum trisulfides, the proper growth conditions for each of the known polymorphs overlaps with the growth conditions of the other polymorph resulting in the formation of both polymorphs in the same reaction vessel.[72] In both systems, the general structure remains relatively unchanged, although, slight structural distortions create a new unit cell. Tantalum trisulfide is believed to undergo a chain rearrangement, although the structure is still unknown,[12, 15] whereas the intrachain rearrangement in niobium trisulfide has been confirmed recently, see Chapter IV.[73] Polymorph isolation is an important undertaking due to the property variation between phases, as demonstrated in both of the described systems.[12, 15, 72] Electrical property variation is also observed as the elements in the transition metal trichalcogenides are changed.

The transition metal trichalcogenides exhibit similar electrical properties to those observed in TMDs including variable electrical conductivity, superconductivity, and CDWs.[12, 15, 57] Many of the known TMTs have been found to be semiconductors, including the group 4 sulfides and selenides[15] as well as specific polymorphs of NbS_3, all of which possess the $ZrSe_3$-type structure, see Chapter IV.[57, 73] Niobium trisulfide, in particular, is interesting due to the presence of alternating Nb-Nb distances, resulting in corrugated chains unique to the transition metal trichalcogenides.[73] These semiconductors possess small bandgaps ranging from ~0.2 – 2.0 eV making them viable contenders for visible light applications.[57, 74] Much like the transition metal dichalcogenides, recent literature has demonstrated the capacity for property tuning in semiconductor transition metal trichalcogenides when moving from the bulk to few layers.[26, 75-76] This capability, however, still remains relatively unexplored in these quasi-1D materials. There are also several TMTs that possess metallic conductivity, including TaS_3,[77] $TaSe_3$,[78] $NbSe_3$,[79] and $HfTe_3$.[80] Confusingly, the literature is still unsettled for $ZrTe_3$, which has been reported as both a semiconductor[81] and a metal/semimetal.[82-83] Several of the transition metal trichalcogenides also exhibit CDW transitions; these materials include TaS_3, $NbSe_3$, $ZrTe_3$, $HfTe_3$, and specific phases of NbS_3.[12, 15, 57]

The high aspect ratio also leads to varied surface energies from those found in TMDs. These different surface energies have been observed to lead to unique topologies, including rings and tubes in NbS_3, TaS_3, $NbSe_3$, and $TaSe_3$.[73, 84-86] The ring topology was first discovered in 1989 by Ter Haar and coworkers.[87] However, the mechanism for the formation of this unique topology is still not firmly established. More recently, Tanda et al. reported their theory that ring formation occurs in the presence of chalcogen droplets, where the TMT ribbons grow around the droplet

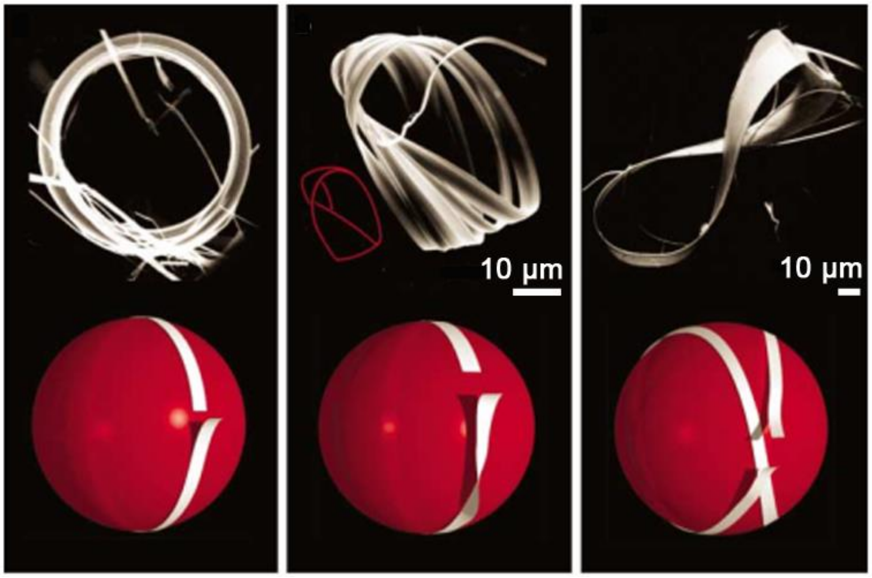

Figure 1.8 Various ring topologies of $NbSe_3$ formed by ribbon formation around a droplet of liquid chalcogen. The ribbon connects to itself, fully encompassing the chalcogen sphere creating a single, continuous ring or Möbius strip. Adapted from [71].

eventually connecting to create a singular loop.[88] This process is demonstrated in Figure 1.8. Enyashin and Ivanovskii reported a first principles study in 2006 investigating the formation of rings and Mobius strips in NbS_3.[89] The authors found that these topologies were more energetically favorable when the TMT ribbons were below a certain chain length with little to no twisting. These new topologies are particularly interesting for the study of CDWs in a closed system.

The distinct structure of transition metal trichalcogenides presents a unique platform for further chemistry, particularly intercalation chemistry. According to Rouxel, ionic mobility of the intercalant increases with decreasing dimensionality allowing for 3D mobility of intercalated ions in a 1D structure and implying a higher ease of intercalation.[12] High ion mobility promotes TMTs as an excellent candidate for intercalation applications, such as Li-ion or group II ion batteries.[12, 90] Chianelli and Dines first reported the topological insertion of Li^+ into the group 4 and Nb trichalcogenides resulting in a lattice expansion in the a and c directions, implying that the chains remained intact. Typical lithium loading was approximately 3 equivalents giving the formula Li_3MX_3.[91] The following year, Murphy and Trumbore reported similar results for $NbSe_3$ and TiS_3 cathodes with the accommodation of up to 3 Li^+ ions for both materials with full or partial reversibility of intercalation, respectively.[92] The partial reversibility in TiS_3 is the consequence of a lithium-chalcogen reaction resulting in a modified structure which hinders intercalation reversibility.[12] Although TiS_3 reveals a reactionary setback, transition metal chalcogenides are prime candidates for extensive intercalation chemistry, although this area of study remains largely unexplored.

Research Goals

The work reported here increases our understanding of the structure-property relationships in low-dimensional, transition metal chalcogenide systems. This dissertation explores the electrically-interesting transition metal chalcogenides $TiSe_2$, $TaSe_2$, and NbS_3, thereby providing insight into the structural, oxidative and chemical behaviors of these materials—vital details for enabling future applications. Together with collaborators at the University of California, Riverside, we characterized the physicochemical and electrical properties of transition metal chalcogenide materials; the specific compositions examined include TaS_2, $TaSe_2$, $TaSe_3$, NbS_3 and $ZrTe_3$.

For future microelectronics applications, it is important to understand not only how a material will conduct electricity, but how it will react to environmental conditions. Chapter II explores the oxidative behavior of 1T-$TiSe_2$ and 1T-$TaSe_2$ upon heating. This process is especially important when considering sustained conductivity because the corresponding oxides are significantly less conductive than the selenides. Both materials in this study displayed initial surface oxidation at 300 °C after 1 h, followed by complete oxidation with increased temperature. Interestingly, cursory oxidation could be removed by mechanical exfoliation to reveal un-oxidized transition metal dichalcogenide, this capability is important for producing oxide-free surfaces during device fabrication.

Chapter III focuses on the phase transitions of 1T -$TaSe_2$ with elevated temperature. Many of the $TaSe_2$ are well established, however, two new polymorph transitions were discovered. The two transitions represent a reversion to the room temperature stable 2H phase, before then experiencing a partial transition to the metastable 4$H(x)$-$TaSe_2$ phases, where $x = a$ or c. These transitions provide further insight into the stability and phase transition behavior of 1T-$TaSe_2$ during heating.

Chapter IV describes the NbS_3 system in detail, including two new polymorphs. Previous work in the literature has provided ill-defined structural characterization, yet well-defined electrical data, for the three polymorphs. Thus, chapter IV discusses the synthetic conditions required to obtain NbS_3 polymorphs and presents single crystal X-ray diffraction structural data that clearly defines these structures for the first time.

References

1. What it is and how is it works. https://www.nano.gov/nanotech-101/what (accessed July 25, 2017).

2. Wang, Q. H.; Kalantar-Zadeh, K.; Kis, A.; Coleman, J. N.; Strano, M. S., *Nat. Nano* **2012,** *7* (11), 699-712.

3. Hulman, M.; Haluška, M.; Scalia, G.; Obergfell, D.; Roth, S., *Nano Lett.* **2008,** *8* (11), 3594-3597.

4. Fugallo, G.; Cepellotti, A.; Paulatto, L.; Lazzeri, M.; Marzari, N.; Mauri, F., *Nano Lett.* **2014,** *14* (11), 6109-6114.

5. Kholmanov, I. N.; Magnuson, C. W.; Aliev, A. E.; Li, H.; Zhang, B.; Suk, J. W.; Zhang, L. L.; Peng, E.; Mousavi, S. H.; Khanikaev, A. B.; Piner, R.; Shvets, G.; Ruoff, R. S., *Nano Lett.* **2012,** *12* (11), 5679-5683.

6. Huang, X.; El-Sayed, M. A., *J. Adv. Res.* **2010,** *1* (1), 13-28.

7. Saxena, U.; Goswami, P., *J. Nanopart. Res.* **2012,** *14* (4), 813.

8. Garrido, C.; Simpson, C. A.; Dahl, N. P.; Bresee, J.; Whitehead, D. C.; Lindsey, E. A.; Harris, T. L.; Smith, C. A.; Carter, C. J.; Feldheim, D. L.; Melander, C.; Margolis, D. M., *Future Med. Chem.* **2015,** *7* (9), 1097-1107.

9. Cabuzu, D.; Cirja, A.; Puiu, R.; Grumezescu, A. M., *Curr. Top. Med. Chem.* **2015,** *15* (16), 1605-1613.

10. Zhu, X.; Cao, Y.; Zhang, J.; Plummer, E. W.; Guo, J., *P. Natl. Acad. Sci. USA* **2015,** *112* (8), 2367-2371.

11. Nikiforov, M. P.; Isakovic, A. F.; Bonnell, D. A., *Phys. Rev. B* **2007,** *76* (3), 033104.

12. Rouxel, J., *Crystal chemistry and properties of materials with quasi-one-dimensional structures : a chemical and physical synthetic approach*. Dordrecht ; Boston : D. Reidel Pub. Co. ; Hingham, MA, U.S.A. : Sold and distributed in the U.S.A. and Canada by Kluwer Academic Publishers, c1986.: 1986.

13. Wilson, J. A.; Di Salvo, F. J.; Mahajan, S., *Phys. Rev. Lett.* **1974,** *32* (16), 882-885.

14. Chhowalla, M.; Shin, H. S.; Eda, G.; Li, L.-J.; Loh, K. P.; Zhang, H., *Nat. Chem.* **2013,** *5* (4), 263-275.

15. Monceau, P., *Adv. Phys.* **2012,** *61* (4), 325-581.

16. Liu, G.; Debnath, B.; Pope, T. R.; Salguero, T. T.; Lake, R. K.; Balandin, A. A., *Nat. Nano* **2016,** *11* (10), 845-850.

17. Yoshida, M.; Suzuki, R.; Zhang, Y.; Nakano, M.; Iwasa, Y., *Sci. Adv.* **2015,** *1* (9).

18. Samnakay, R.; Wickramaratne, D.; Pope, T. R.; Lake, R. K.; Salguero, T. T.; Balandin, A. A., *Nano Lett.* **2015,** *15* (5), 2965-2973.

19. Thomson, R. E.; Burk, B.; Zettl, A.; Clarke, J., *Phys. Rev. B* **1994,** *49* (24), 16899-16916.

20. Minoru Osada, T. S., *J. Mater. Chem.* **2009,** *19*, 9.

21. Yoffe, A. D., *Solid State Ionics* **1990,** *39* (1), 1-7.

22. Renteria, J.; Samnakay, R.; Jiang, C.; Pope, T. R.; Goli, P.; Yan, Z.; Wickramaratne, D.; Salguero, T. T.; Khitun, A. G.; Lake, R. K.; Balandin, A. A., *J. Appl. Phys.* **2014,** *115* (3), 034305.

23. Srivastava, S. K.; Avasthi, B. N., *J. Mater. Sci.* **1992,** *27* (14), 3693-3705.

24. SchÄFer, H., CHAPTER 2 - Experimental and Theoretical Principles. In *Chemical Transport Reactions*, Academic Press: 1964; pp 5-34.

25. SchÄFer, H., CHAPTER 3 - The Transport of Solid Substances and Its Special Applications. In *Chemical Transport Reactions*, Academic Press: 1964; pp 35-98.

26. Jin, Y.; Li, X.; Yang, J., *Phys. Chem. Chem. Phys.* **2015,** *17* (28), 18665-18669.

27. Godfrey, D.; Nelson, E. C., Oxidation Characteristics of Molybdenum Disulfide and Effect of Such Oxidation on its Role as a Solid-Film Lubricant. Aeronautics, N. A. C. f., Ed. Lewis Flight Propulsion Lab; Cleveland OH, United States, 1949; p 30.

28. Ross, S.; Sussman, A., *J. Phys. Chem.* **1955,** *59* (9), 889-892.

29. Goli, P.; Khan, J.; Wickramaratne, D.; Lake, R. K.; Balandin, A. A., *Nano Lett.* **2012,** *12* (11), 5941-5945.

30. Lopez-Sanchez, O.; Lembke, D.; Kayci, M.; Radenovic, A.; Kis, A., *Nat. Nano* **2013,** *8* (7), 497-501.

31. Lieth, R. M. A.; Terhell, J. C. J. M., Transition Metal Dichalcogenides. In *Preparation and Crystal Growth of Materials with Layered Structures*, Lieth, R. M. A., Ed. Springer Netherlands: Dordrecht, 1977; pp 141-223.

32. Yan, Z.; Jiang, C.; Pope, T. R.; Tsang, C. F.; Stickney, J. L.; Goli, P.; Renteria, J.; Salguero, T. T.; Balandin, A. A., *J. Appl. Phys.* **2013,** *114* (20), 204301.

33. Stewart, T. B.; Fleischauer, P. D., *Inorg. Chem.* **1982,** *21* (6), 2426-2431.

34. Kadijk, F.; Huisman, R.; Jellinek, F., *Recl. Trav. Chim. Pays-B.* **1964,** *83* (7), 768-775.

35. Luo, H.; Xie, W.; Tao, J.; Pletikosic, I.; Valla, T.; Sahasrabudhe, G. S.; Osterhoudt, G.; Sutton, E.; Burch, K. S.; Seibel, E. M.; Krizan, J. W.; Zhu, Y.; Cava, R. J., *Chem. Mater.* **2016,** *28* (6), 1927-1935.

36. Boulos, R. A.; Zhang, F.; Tjandra, E. S.; Martin, A. D.; Spagnoli, D.; Raston, C. L., *Sci. Rep. UK* **2014,** *4*, 3616.

37. Ramsdell, L. S., *Am. Mineral.* **1947,** *32* (1-2), 64-82.

38. Lin, Y.-C.; Dumcenco, D. O.; Huang, Y.-S.; Suenaga, K., *Nat. Nanotechnol.* **2014,** *9*, 391.

39. Huisman, R.; Jellinek, F., *J. Less-Common Met.* **1969,** *17* (1), 111-117.

40. Hossain, M.; Zhao, Z.; Wen, W.; Wang, X.; Wu, J.; Xie, L., *Recent Advances in Two-Dimensional Materials with Charge Density Waves: Synthesis, Characterization and Applications*. 2017; Vol. 7, p 298.

41. Bjerkelund, E.; Kjekshus, A., *Acta Chem. Scand.* **1967,** *21* (2).

42. Zandt, T.; Dwelk, H.; Janowitz, C.; Manzke, R., *J. Alloy. Compd.* **2007,** *442* (1), 216-218.

43. Sankar, R.; Narsinga Rao, G.; Muthuselvam, I. P.; Butler, C.; Kumar, N.; Senthil Murugan, G.; Shekhar, C.; Chang, T.-R.; Wen, C.-Y.; Chen, C.-W.; Lee, W.-L.; Lin, M. T.; Jeng, H.-T.; Felser, C.; Chou, F. C., *Chem. Mater.* **2017,** *29* (2), 699-707.

44. Braga, D.; Gutiérrez Lezama, I.; Berger, H.; Morpurgo, A. F., *Nano Lett.* **2012,** *12* (10), 5218-5223.

45. Boscher, N. D.; Carmalt, C. J.; Parkin, I. P., *J. Mater. Chem.* **2006,** *16* (1), 122-127.

46. Vellinga, M. B.; de Jonge, R.; Haas, C., *J. Solid State Chem.* **1970,** *2* (2), 299-302.

47. Lucovsky, G.; White, R. M.; Benda, J. A.; Revelli, J. F., *Phys. Rev. B* **1973,** *7* (8), 3859-3870.

48. Brixner, L. H., *J. Inorg. Nucl. Chem.* **1962,** *24* (3), 257-263.

49. Ozaydin, H. D.; Sahin, H.; Kang, J.; Peeters, F. M.; Senger, R. T., *2D Mater.* **2015,** *2* (4), 044002.

50. Gao, J.; Li, B.; Tan, J.; Chow, P.; Lu, T.-M.; Koratkar, N., *ACS Nano* **2016,** *10* (2), 2628-2635.

51. Huang, Y.; Sutter, E.; Shi, N. N.; Zheng, J.; Yang, T.; Englund, D.; Gao, H.-J.; Sutter, P., *ACS Nano* **2015,** *9* (11), 10612-10620.

52. Li, H.; Lu, G.; Wang, Y.; Yin, Z.; Cong, C.; He, Q.; Wang, L.; Ding, F.; Yu, T.; Zhang, H., *Small* **2013,** *9* (11), 1974-1981.

53. Hajiyev, P.; Cong, C.; Qiu, C.; Yu, T., *Sci. Rep. UK* **2013,** *3*, 2593.

54. Zeng, Z.; Yin, Z.; Huang, X.; Li, H.; He, Q.; Lu, G.; Boey, F.; Zhang, H., *Angew. Chem. Int. Edit.* **2011,** *50* (47), 11093-11097.

55. Yoshida, M.; Ye, J.; Nishizaki, T.; Kobayashi, N.; Iwasa, Y., *Appl. Phys. Lett.* **2016,** *108* (20), 202602.

56. Coleman, J. N.; Lotya, M.; O'Neill, A.; Bergin, S. D.; King, P. J.; Khan, U.; Young, K.; Gaucher, A.; De, S.; Smith, R. J.; Shvets, I. V.; Arora, S. K.; Stanton, G.; Kim, H.-Y.; Lee, K.; Kim, G. T.; Duesberg, G. S.; Hallam, T.; Boland, J. J.; Wang, J. J.; Donegan, J. F.; Grunlan, J. C.; Moriarty, G.; Shmeliov, A.; Nicholls, R. J.; Perkins, J. M.; Grieveson, E. M.; Theuwissen, K.; McComb, D. W.; Nellist, P. D.; Nicolosi, V., *Science* **2011,** *331* (6017), 568-571.

57. Island, J. O.; Molina-Mendoza, A. J.; Barawi, M.; Biele, R.; Flores, E.; Clamagirand, J. M.; Ares, J. R.; Sánchez, C.; van der Zant, H. S. J.; D'Agosta, R.; Ferrer, I. J.; Castellanos-Gomez, A., *2D Mater.* **2017,** *4* (2), 022003.

58. McTaggart, F.; Wadsley, A., *Aust. J. Chem.* **1958,** *11* (4), 445-457.

59. Brattas, L.; Kjekshus, A., *Acta Chem. Scand.* **1972,** *26* (9), 3441-3449.

60. Kadijk, F.; Jellinek, F., *J. Less-Common Met.* **1969,** *19* (4), 421-430.

61. BJERKELUND, E.; KJEKSHUS, A., *Acta. Chem. Scand.* **1965,** *19* (3), 11.

62. Meerschaut, A.; Rouxel, J.; Haen, P.; Monceau, P.; Nunez-Regueiro, M., *J. Phys. Lett.-Paris* **1979,** *40*, 3.

63. Hodeau, J. L.; Marezio, M.; Roucau, C.; Ayroles, R.; Meerschaut, A.; Rouxel, J.; Monceau, P., *J. Phys. C Solid State* **1978,** *11* (20), 4117.

64. Krönert, W.; Plieth, K., *Z. Anorg. Allg. Chem.* **1965,** *336* (3-4), 207-218.

65. Bjerkelund, E.; Kjekshus, A., *Z. Anorg. Allg. Chem.* **1964,** *328* (5-6), 235-242.

66. Rijnsdorp, J.; Jellinek, F., *J. Solid State Chem.* **1978,** *25* (4), 325-328.

67. Jellinek, F.; Pollak, R. A.; Shafer, M. W., *Mater. Res. Bull.* **1974,** *9* (6), 845-856.

68. Endo, K.; Ihara, H.; Watanabe, K.; Gonda, S.-I., *J. Solid State Chem.* **1981,** *39* (2), 215-218.

69. Wilson, J. A., *Phys. Rev. B* **1979,** *19* (12), 6456-6468.

70. Kurdi, M.; Marie, A.-M.; Danot, M., *Solid State Commun.* **1987,** *64* (4), 395-399.

71. Bučar, D.-K.; Lancaster, R. W.; Bernstein, J., *Angew. Chem. Int. Edit.* **2015,** *54* (24), 6972-6993.

72. Cornelissens, T.; Van Tendeloo, G.; Van Landuyt, J.; Amelinckx, S., *Phys. Status Solidi A* **1978,** *48* (1), K5-K9.

73. Bloodgood, M. A.; Wei, P.; Aytan, E.; Bozhilov, K. N.; Balandin, A. A.; Salguero, T. T., *APL Mater.* **2018,** *6* (2), 026602.

74. Li, M.; Dai, J.; Zeng, X. C., *Nanoscale* **2015,** *7* (37), 15385-15391.

75. Lipatov, A.; Wilson, P. M.; Shekhirev, M.; Teeter, J. D.; Netusil, R.; Sinitskii, A., *Nanoscale* **2015,** *7* (29), 12291-12296.

76. Island, J. O.; Buscema, M.; Barawi, M.; Clamagirand, J. M.; Ares, J. R.; Sánchez, C.; Ferrer, I. J.; Steele, G. A.; van der Zant, H. S. J.; Castellanos-Gomez, A., *Adv. Opt. Mater.* **2014,** *2* (7), 641-645.

77. Farley, K. E.; Shi, Z.; Sambandamurthy, G.; Banerjee, S., *Phys. Chem. Chem. Phys.* **2015,** *17* (28), 18374-18379.

78. Stolyarov, M. A.; Liu, G.; Bloodgood, M. A.; Aytan, E.; Jiang, C.; Samnakay, R.; Salguero, T. T.; Nika, D. L.; Rumyantsev, S. L.; Shur, M. S.; Bozhilov, K. N.; Balandin, A. A., *Nanoscale* **2016,** *8* (34), 15774-15782.

79. Hor, Y. S.; Xiao, Z. L.; Welp, U.; Ito, Y.; Mitchell, J. F.; Cook, R. E.; Kwok, W. K.; Crabtree, G. W., *Nano Lett.* **2005,** *5* (2), 397-401.

80. Denholme, S. J.; Yukawa, A.; Tsumura, K.; Nagao, M.; Tamura, R.; Watauchi, S.; Tanaka, I.; Takayanagi, H.; Miyakawa, N., *Sci. Rep. UK* **2017,** *7*, 45217.

81. Stöwe, K.; Wagner, F. R., *J. Solid State Chem.* **1998,** *138* (1), 160-168.

82. Hu, Y.; Zheng, F.; Ren, X.; Feng, J.; Li, Y., *Phys. Rev. B* **2015,** *91* (14), 144502.

83. Khumalo, F. S.; Hughes, H. P., *Phys. Rev. B* **1980,** *22* (4), 2078-2088.

84. Tanda, S.; Kawamoto, H.; Shiobara, M.; Sakai, Y.; Yasuzuka, S.; Okajima, Y.; Yamaya, K., *Physica B* **2000,** *284–288, Part 2*, 1657-1658.

85. Matsuura, T.; Yamanaka, M.; Hatakenaka, N.; Matsuyama, T.; Tanda, S., *J. Cryst. Growth* **2006,** *297* (1), 157-160.

86. Tsuneta, T.; Tanda, S., *J. Cryst. Growth* **2004,** *264* (1–3), 223-231.

87. Trumbore, F. A.; Ter Haar, L. W., *Chem. Mater.* **1989,** *1* (5), 490-492.

88. Tanda, S.; Tsuneta, T.; Okajima, Y.; Inagaki, K.; Yamaya, K.; Hatakenaka, N., *Nature* **2002,** *417*, 397.

89. Enyashin, A. N.; Ivanovskiĭ, A. L., *Phys. Solid State+* **2006,** *48* (4), 780-785.

90. Yuan, W.; Günter, J. R., *Solid State Ionics* **1995,** *76* (3), 253-258.

91. Chianelli, R. R.; Dines, M. B., *Inorg. Chem.* **1975,** *14* (10), 2417-2421.

92. Murphy, D. W.; Trumbore, F. A., *J. Electrochem. Soc.* **1976,** *123* (7), 960-964.

CHAPTER 2

OXIDATION OF TITANIUM AND TANTALUM DISELENIDE CRYSTALS

Matthew A. Bloodgood, Timothy R. Pope, Rameez Samnakay, Alexander A. Balandin, Tina T. Salguero. *To be submitted to the Journal of Physical Chemistry C.*

Abstract

Titanium and tantalum diselenides have interesting electronic properties in both bulk and exfoliated forms, however, these materials are susceptible to oxidation limiting their applicability. This chapter describes the chemistry and oxidation of millimeter-sized crystals of 1*T*, 2*H*, and 3*R*-$TaSe_2$ and 1*T*-$TiSe_2$. The optimal, transport concentration range for growing crystals free of iodine impurities was found for chemical vapor transport. Crystals of both 1*T*-$TiSe_2$ and 1*T*-$TaSe_2$ heated in air demonstrated noticeable surface oxidation after heating for 1 hour beginning at 300 °C with oxide layers 550-670 nm and 250-300 nm thick, respectively. Additionally, heating at $\geq$300 °C as well as prolonged exposure at room temperature in air resulted in a polymorph transformation in $TaSe_2$. Both oxidation and polymorph transformation, however, are limited to the crystal surface when heated below 600 °C or left in ambient conditions. Surface can then be removed through simple mechanical exfoliation methods enabling the recovery of unoxidized, crystalline transition metal diselenide.

Introduction

The current intensity of attention on transition metal dichalcogenides is remarkable. The interesting properties of MX_2 compositions (M = transition metal, X = S, Se, Te) include superconductivity,[1-2] charge density waves,[2-4] and anisotropic optical behavior,[5] and recent work has demonstrated that many of these properties can be tuned at the nanoscale.[6-8] MoS_2, for example, transitions from a 1.2 eV indirect bandgap found in the bulk to a 1.8 eV direct bandgap upon reaching a monolayer in thickness, thus allowing for moderate bandgap tuning within a single material.[9-10] Additionally, the charge density wave (CDW) transition temperature of 1*T*-$TiSe_2$ has been shown to increase from 200 K (bulk T_c) to nearly 240 K as the sample thickness is reduced below 100 nm.[7, 11] In another instance, Tsen 2015 observed a continuous variation in resistivity corresponding to the nearly commensurate to commensurate CDW transitions in 1*T*-TaS_2 as the sample thickness is decreased.[12] The array of property tunability arises from the diverse class of transition metal dichalcogenides.

The diversity of MX_2 materials is further enriched by structural polymorphism. Although $TiSe_2$ adopts only the 1*T* form, $TaSe_2$ has numerous polymorphs including 1*T*, 2*H*, and 3*R* forms (Figure 2.1).[13] According to Ramsdell notation,[14] the numerical prefix describes the number of X–M–X layers per unit cell (i.e., 2*H* has two X–M–X layers per unit cell whereas 3*R* has three), and the italicized letter indicates the crystal system (*T* = trigonal, *H* = hexagonal, *R* = rhombohedral).

In the isostructural 1*T*-$TiSe_2$ and 1*T*-$TaSe_2$, the metal centers adopt an octahedral coordination geometry with the three selenium atoms above the metal centers rotated 60° relative to the three below within the Se–M–Se layer (Figure 2.1a,b). For $TiSe_2$, the 1*T*- structure is the only form observed from room temperature to >850 °C.[15] $TaSe_2$ possesses multiple metastable

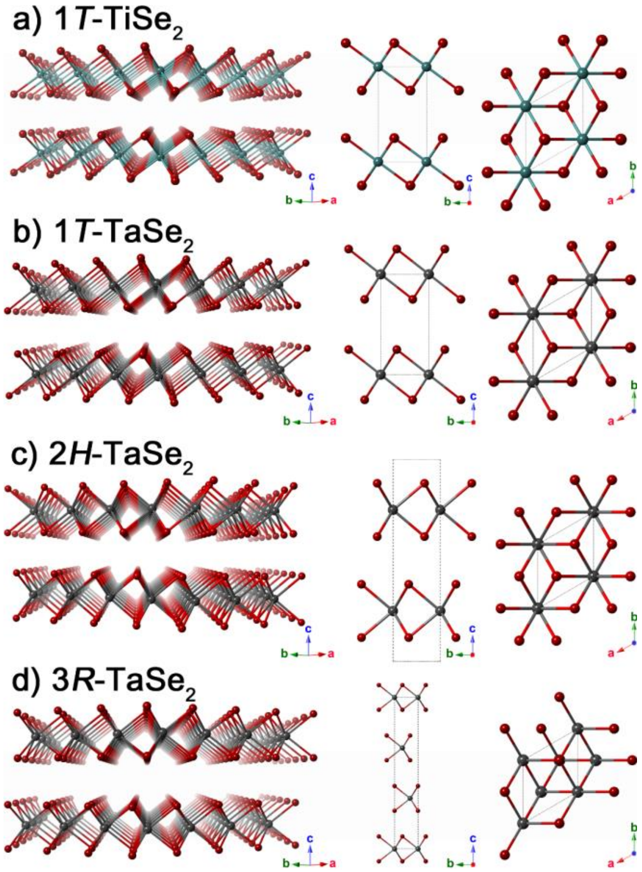

Figure 2.1 Crystal structures of TiSe$_2$ and TaSe$_2$ polymorphs: a) 1*T*-TiSe$_2$, b) 1*T*-TaSe$_2$, c) 2*H*-TaSe$_2$, and d) 3*R*-TaSe$_2$. The views on the left highlight the layered nature of these materials and the van der Waals gap between each layer. The views in the center and on the right show the structures down the a- and c-axes, respectively.

polymorphs, including 1*T* and 3*R*, with 2*H*-TaSe$_2$ as the room temperature stable polymorph. In contrast to the 1*T* polymorphs, 2*H* and 3*R*-TaSe$_2$ exhibit trigonal prismatic coordination geometries about the tantalum centers, which results in alignment of the intralayer selenium atoms (Figure 2.1c,d). The 2*H*-TaSe$_2$ structure consists of a two-layer AcA BcB repeating pattern of Se–Ta–Se layers; like the 1*T* form, the tantalum atoms remain aligned and the trigonal prisms of selenium atoms are rotated 60° with respect to each other (Figure 2.1c). The 3*R*-TaSe$_2$ structure has a three-layer stacking pattern in which the metal centers are off-set from the Se–Ta–Se layers above and below (Figure 2.1d). Thus, 2*H*- and 3*R*-$TaSe_2$ are properly considered polytypes (only the stacking arrangement of layers differs), whereas the major difference between the 1*T* and 2*H*,3*R* polymorphs is the coordination geometry of the transition metal.

These structural differences lead to highly varied electronic properties in the $TaSe_2$ and other MX_2 systems. In $TaSe_2$ for example, various CDW states are present below 120 K in 2*H*-$TaSe_2$, while 1*T*-$TaSe_2$ is in a commensurate CDW state at room temperature and undergoes a commensurate to incommensurate CDW transition at ~475 K.[16] These transitions significantly affect the resistivity behavior of the 1*T* and 2*H* polymorphs at 300 K as reported by Wilson 1974 even though both phases are metallic in nature.[17] A polymorph change in the $MoTe_2$ system is also accompanied by a significant change in the electronic properties. With increased temperature, 2*H*-$MoTe_2$ changes to the metallic phase 1*T*-$MoTe_2$.[18] To maintain these electronic properties, the oxidative stability of MX_2 materials must be accounted for.

The oxidation of MX_2 materials is an important experimental consideration that results in undesired material degradation. Whereas oxidation studies in the older literature focus on the mechanical properties of MX_2 materials used as lubricants,[19,20] recent studies are motivated by how oxidation impacts material processing and electronic properties in light of device applications.[21] MoS_2 is generally considered to be the most stable MX_2 composition with respect to oxidation, yet Gao 2016 demonstrated the poor air stability of MoS_2 and WS2 monolayers, which are strongly affected by oxidation along grain boundaries and the adsorption of organic contaminants; the result was quenching of the direct gap photoluminescence.[22] Furthermore, Wang 2017 found that in aqueous environments, oxidative dissolution consumes MoS_2 nanosheets and contributes to aggregation/restacking phenomena.[23] Liu 2015 observed significant surface oxidation in WSe_2 at 400 °C after only 1 h and total surface oxidation at 2 h.[24] Woods 2017 showed that magnetoresistance in WTe_2 became suppressed by the formation of a ~2 nm thick amorphous surface oxide layer at ambient conditions, which causes decreased electron and hole mobilities.[25]

Group 4 and 5 transition metal-based MX_2 materials are even more susceptible to oxidation. For example, Chae 2016 observed the total loss of electrical performance from HfS_2-based FET devices within 2 days at ambient conditions.[26] El-Bana 2013 encountered the undesired photo-oxidation of $NbSe_2$ to Nb_2O_5 under laser heating.[27] In addition, Tsen 2015 found that 1*T*-TaS_2 exfoliated in air showed no CDW structure in the electron diffraction due to the formation of a ~2 nm thick layer of amorphous oxide, which is proposed to lead to strong surface pinning that interferes with charge ordering.[12] Thus it is apparent that oxidation affects all MX_2 materials, and few-layer or monolayer samples with high surface areas are especially sensitive to degradation originating at structural defects.

MX_2 oxidation can be a double-edged sword, however. A growing number of recent reports highlight the use of controlled MX_2 oxidation to tune material properties in a beneficial way. Yamamoto 2015 found that WSe_2 could undergo self-limiting oxidation at temperatures below 100 °C under ozone exposure. The oxidation, confined to the top-most surface layers, resulted in highly hole-doped WO_x–WSe_2 heterostructurse.[28] Li 2016 similarly showed that exposure of WSe_2 to a low-power remote oxygen plasma caused selective oxidation of the topmost layer.[29] Lu 2015 also have demonstrated that laser thinning of WSe_2 in air leads to the filling of selenium vacancies with oxygen, which passivates the material and improves its properties.[30] With TiS_2, Cucinotta 2015 used partial oxidation to prepare $TiS_{2-x}O_x$ alloys with engineered band gaps.[31] From a different perspective, Chen 2017 consider the enhanced oxidative degradation of MoS_2 nanoflakes in acidic tumor environments as complementary to photothermal cancer therapy.[32] In several further examples, the oxidation of MX_2 materials is taken to completion, as in the conversion of TiS_2 nanodiscs into TiO_2 nanodiscs,[33] the transformation of few-layer TaS_2 into high-quality Ta_2O_5 atomic films,[34] and the local oxidation nanolithography of metallic MX_2 surfaces.[35] In all these instances, oxidation is used as an advantageous form of chemical modification.

In this chapter, the oxidation of 1*T*-$TiSe_2$, 1*T*-$TaSe_2$, and 2*H*,3*R*-$TaSe_2$ crystals is described. There are several reasons for interest in this particular subset of MX_2 materials: (1) The majority of prior work has focused on group 4 metal MX_2 compositions rather than those based on groups 4 and 5, and it is useful to better understand the oxidation chemistry of these more reactive MX_2 materials. (2) The inclusion of 1*T*-$TiSe_2$ and 1*T*-$TaSe_2$ allows us to directly compare the stability of isostructural MX_2 materials. (3) The inclusion of 1*T*-$TaSe_2$ and 2*H*,3*R*-$TaSe_2$ allows us to directly compare the stability of different polymorphs with the same MX_2 composition. In previous work, we examined 2*H*-$TaSe_2$ crystals after exposure to air by x-ray photoelectron spectroscopy (XPS).[36] Such aged samples showed peaks corresponding to the native oxide of tantalum, Ta_2O_5. Fortunately, this oxidized surface material could be removed by mechanical delamination, which indicated that Ta_2O_5 does not penetrate throughout the crystal. Now further details about the oxidation of $TaSe_2$ are presented here. The experiments included heating crystals of each MX_2 system in air at 100 – 600 °C for 1 h as well as exposure to air at and below 200 °C for 6 h. The oxide layer thicknesses were examined and established after oxidation of the crystal surfaces. In addition, we monitored $TaSe_2$ samples over time to detect structural changes triggered by oxidation.

Experimental Methods

Growth of 1*T*-$TiSe_2$, 1*T*-$TaSe_2$, 2*H*-$TaSe_2$, and 3*R*-$TaSe_2$ crystals. 1*T*-$TiSe_2$, 1*T*-$TaSe_2$, 2*H*-$TaSe_2$, and 3*R*-$TaSe_2$ were synthesized from crystalline titanium (Sigma, ≥99.99%), tantalum powder (STREM, 99.98%), and selenium powder (STREM, 99.99%) using the chemical vapor transport method with iodine (J.T. Baker, 99.9%) at ~4 mg cm^{-3} as the transport agent. For 1*T*-$TiSe_2$, the titanium and iodine were first placed into a quartz ampule followed by Se. In the case of $TaSe_2$, Ta and Se powders were first ground together before being placed into an ampule with iodine. The quartz ampules were evacuated and backfilled three times with Ar, before being sealed under vacuum. For the 1*T* reactions, the filled quartz vessels were then placed in a two-zone tube furnace at 975 °C with a ~100 °C gradient for 168 or 336 h before quenching in ice water. 2*H*-$TaSe_2$ was synthesized in a two-zone furnace at 800 °C with a 100 °C gradient for 336 h followed by a controlled cool (~1 °C min^{-1}), whereas 3*R*-$TaSe_2$ was synthesized in a two-zone furnace at 750 °C for 120 h before quenching in salted, ice water.

Preparation of oxidized crystals. 1*T*-$TiSe_2$ and 1*T*-$TaSe_2$ crystals were placed in alumina crucibles in a box furnace and ramped at 10 °C min^{-1} before holding at the specified temperatures for 1 or 6 h. Heating temperatures for 1 h included 100, 200, 300, and 400 °C for 1*T*-$TiSe_2$ and 100, 200, 300, 400, and 600 °C for 1*T*-$TaSe_2$; crystals were air-quenched from these temperatures. For the 6 h duration, crystals from both systems were heated at temperatures ranging from 100 to 200 °C. The furnace was permitted to cool to room temperature naturally after holding at the specified temperature for the given time. Afterwards, the oxidized crystals were stored in an Ar-filled glovebox to prevent any further oxidation. For oxide layer thickness measurements, crystals of 1*T*-$TiSe_2$ were heated at 300 and 400 °C for 1 h, whereas 1*T*-$TaSe_2$ crystals were heated at 300 and 600 °C for 1 h, and 300 °C for 6 h. Heated crystals were then glued into an Eppendorf top in an “on-edge” orientation before encasing in epoxy (Buehler, Epothin 2). After curing for 24 h, the epoxy was quickly polished with 600-grit sandpaper to reveal the crystal edges. These samples were carbon coated for SEM/EDS analysis.

Characterization details. Powder X-ray Diffraction was carried out on a Bruker D8 Advance diffractometer with a Co-Kα radiation source. Powders were prepared by gentle grinding in isopropyl alcohol before drying and pressing into an aluminum mount. The data were collected from 10–80° 2θ at a rate of 0.1 s per step at 40 mA and 40 kV. Scanning Electron Microscopy and Energy Dispersive Spectroscopy data were acquired on a FEI Teneo FE-SEM with an Oxford Instruments X-MAX^N detector operated between 5 and 20 keV. Raman spectroscopy data were acquired using a Renishaw InVia microscope. Studies were carried out at 50x magnification under 785 nm irradiation with a laser power between 5 μW and 5 mW.

Results and Discussion

Chemical Vapor Transport of 1*T*-$TiSe_2$, and 1*T*-, 2*H*-, and 3*R*-$TaSe_2$. Chemical vapor transport (CVT) is accomplished by heating stoichiometric amounts of elemental transition metal and chalcogenide at high temperatures in an air-free environment[37-38] producing large, high-quality crystals.[39-40] The elemental powders are first ground together and placed in a fused quartz ampule along with a transport agent, typically 3–5 mg cm^{-3} of I_2. Oxygen and water are removed from the system through evacuation/inert gas purging cycles; excessive sublimation of I_2 during evacuation is prevented using a dry ice/acetonitrile bath (–41 °C). After the final evacuation, the ampule is sealed and heated in a two-zone furnace with a fixed gradient. The end of the ampule containing the ground sample is placed in the higher temperature zone, which is typically 50–100 °C hotter than the lower temperature zone. The transport agent first vaporizes before complexing with the source material, vaporized, and then slowly transports to and deposits in the lower temperature zone of the ampule resulting in crystal growth. After 1–2 weeks, the CVT grown crystals can reach lateral dimensions of a few centimeters.

The quality and size of the crystal growth are strongly dependent on the temperature as well as the temperature gradient.[37] Additionally, the polymorph is determined by not only the temperature, but also the cooling rate after completion.[38, 41] $TiSe_2$ and $TaSe_2$ crystal growth differ in this regard due to the lack of observed polymorphs for $TiSe_2$. While $TaSe_2$ exhibits several well-documented polymorphs, $TiSe_2$ crystallizes only in the 1*T* form.[13] 1*T*-$TiSe_2$ crystals can form in a range of temperatures from 640 °C to temperatures in excess of 950 °C.[13]

The many phases of $TaSe_2$ can be differentiated through, not only, growth temperature, but also varied cooling rates; in some cases, variation of both parameters is required to produce metastable polymorphs.[42] The room-temperature stable 2*H* and 3*R* phases are an example of the latter case. With a reaction temperature between 500 and 800 °C, a slow cooling rate ($1\ ^\circ\ \mathrm{min}^{-1}$) results in nearly phase-pure 2*H*-$TaSe_2$, whereas rapid quenching results primarily in 3*R*-$TaSe_2$ with some 2*H*-$TaSe_2$.[37] The 3*R* phase of $TaSe_2$, can also be obtained from annealing 1*T*-$TaSe_2$ between 300 and 500 °C under inert or vacuum conditions, as described by Bjerkelund et. al.[42] The high-temperature 1*T*-$TaSe_2$ polymorph results from growth temperatures exceeding 900 °C, however, rapid quenching is required to isolate this phase. Figure 2.2 shows PXRD patterns of the 1*T*-$TiSe_2$ and 1*T*-$TaSe_2$ crystals obtained after rapid quenching from 975 °C after CVT. The defined peaks in both patterns indicate a large, highly crystalline product with the $TaSe_2$ pattern showing only a small amount of a second polymorph (2*H*-$TaSe_2$). A second polymorph can result because quenching in ice water is not instantaneous, thus allowing some slower-cooling polytypes, 2*H* or

3R-TaSe$_2$, to form. Fortunately, the color differences between the room temperature stable and high temperature stable polymorphs permits easy separation: 1T-TaSe$_2$ crystals can be identified and separated due to their distinctive golden color.[43]

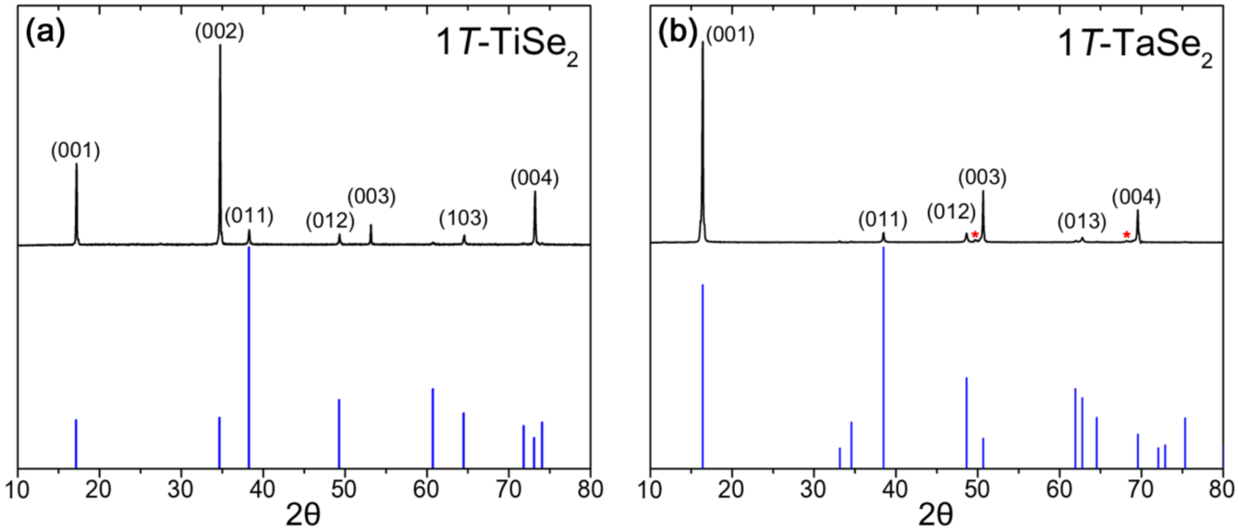

Figure 2.2 PXRD patterns of (a) 1T-TiSe$_2$ and (b) 1T-TaSe$_2$ ground crystals from the growth region of the CVT vessel showing defined peaks that indicate larger crystalline domains with a strong orientation effect along the (00ℓ) layer planes. Droplines are known peak positions for 1T-TiSe$_2$ (ICDD 04-006-9253) and 1T-TaSe$_2$ (ICDD 04-003-4189) and the red asterisks indicate trace amounts of 2H-TaSe$_2$.

Crystals of both materials were examined by scanning electron microscopy (SEM) and energy dispersive x-ray spectroscopy (EDS). Figure 2.S2 shows SEM images of 1T-TiSe$_2$, 1T-TaSe$_2$, 2H-TaSe$_2$, and 3R-TaSe$_2$ crystals after CVT growth with no oxide impurities or inclusion of the transport agent. These high-quality crystals are characterized by smooth surfaces and sharp edges. The EDS data for 1*T*-$TiSe_2$ and 1*T*-$TaSe_2$ crystals are summarized in Table 2.S1. These data show that the actual stoichiometry in both systems matches the theoretical stoichiometry to within 2 atomic %, thus retaining a nearly stoichiometric 1:2 ratio.

To achieve the synthesis of high-quality crystals, care must be taken to not use an excessive amount of transport agent. Figure 2.3 presents SEM images of 1*T*-$TaSe_2$ crystals produced by CVT with an "ideal" and "excessive" amount of I_2 transport agent. Crystals grown using an ideal amount of I_2 transport agent (3–5 mg cm^{-3}) show smooth surfaces and edge sites (Figure 2.3a); some of these crystals are composed of tantalum and selenium only, although, about one quarter of the crystals exhibit some iodine doping. Indeed, DiSalvo 1976 found the incorporation of 0.3 atomic % I_2 in $TiSe_2$ crystals when using 1.5 mg cm^{-3} I_2 for CVT growth.[44]

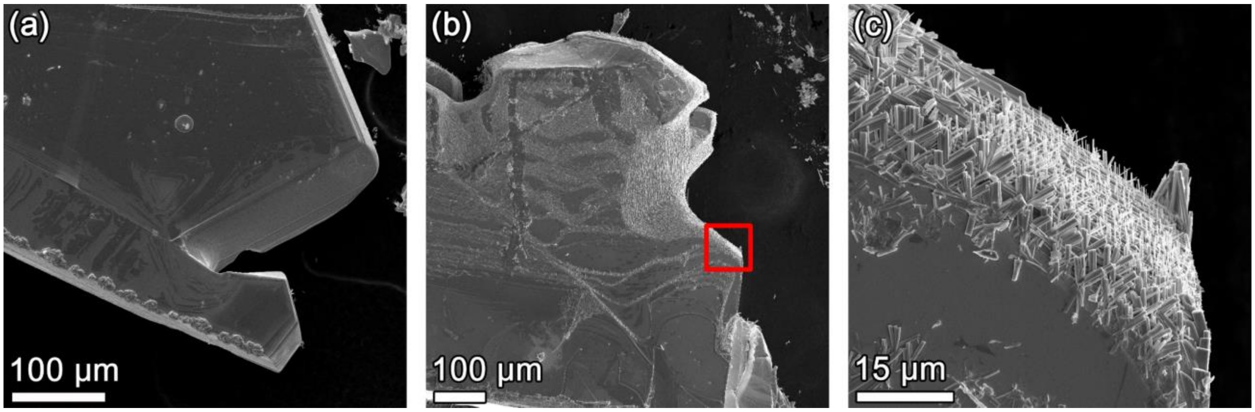

Figure 2.3 SEM images of 1*T*-$TaSe_2$ after CVT growth using (a) "ideal" and (b,c) excessive I_2. The red box in panel (b) indicates the magnified area in panel (c).

When excessive I_2 is used (6–10 mg/cm^{-3}), small rod-like crystals form at the edge sites on about 85% of the observed crystals (Figure 2.3b). The iodine-containing rods were found to be approximately 1–4 μm wide and up to 30 μm in length as seen by SEM (Figure 2.S3). EDS (Table 2.S1) revealed incorporation of iodine at over 9.5 atomic % in the dissociated rods. This stoichiometry does not match any previously reported discrete Ta-Se-I phases [e.g., $(TaSe_4)_2I$].[45] These data show that relatively high concentrations of transport agent can lead to iodine-containing phase(s). Thus, it is important to consider not only the stoichiometric ratio of metal to chalcogenide, but also the concentration of I_2 transport agent used during CVT growth.

Surface Oxidation at Elevated Temperatures. Because oxidation negatively affects the performance of materials used in electronic devices, it is important to quantify the extent of oxidation in varying environmental conditions. $TiSe_2$ and $TaSe_2$ were characterized to further understand surface oxidation of MX_2 systems using Raman spectroscopy, EDS, and SEM methods. Prior reports utilizing thermal gravimetric analysis (TGA) indicate that many bulk MX_2 materials have oxidation temperatures exceeding 500 °C.[19] Thus, oxidation across a range of temperatures (100–600 °C) with varying times were studied to understand when oxidation occurs and to what extent. Figure 2.4 shows the Raman spectra of 1*T*-$TiSe_2$ and 1*T*-$TaSe_2$ crystals heated at various temperatures for 1 h in air. For both 1*T*-$TiSe_2$ and 1*T*-$TaSe_2$, no noticeable change in peak position or width is seen for the samples heated at 100 °C and 200 °C, and both spectra match well to a room temperature reference sample as seen in Figure 2.S4a. However, after being heated at 300 °C for 1 h, a distinct change is observed in the spectra of both materials.

At 300 °C, 1*T*-$TiSe_2$ (Figure 2.4a) shows the emergence of a strong, now dominating peak at 252 cm^{-1} corresponding to the A_{1g} peak of Se;[46] this peak also contains the significantly diminished E_g stretch of 1*T*-$TiSe_2$ at 233 cm^{-1} as revealed by the peak asymmetry. The peak at ~196 cm^{-1}, matching to the A_{1g} peak of 1*T*-$TiSe_2$, also becomes significantly more pronounced at this temperature.[11] The strong Se peak results from Se leaving the structure, implying the onset of oxidation. After heating at 400 °C, a strong peak emerges at 143 cm^{-1} along with smaller peaks at 398, 517, and 640 cm^{-1}, while the 1*T*-$TiSe_2$ and Se peaks are completely diminished. These new peaks correspond to the Raman spectrum of anatase TiO_2, the expected phase of TiO_2 at this temperature.[47] This oxidation regime is quite similar to that observed by Long 2017 for the oxidation of TiS_2 in an ambient or O_2 environment. Interestingly, those authors point to moisture removal as a critical factor for mitigation of surface oxidation.[48]

Similarly, 1*T*-$TaSe_2$ (Figure 2.4b) shows a broad peak emerge at 248 cm^{-1} after 1 h at 300 °C, which may correspond to either amorphous Se A_{1g}, as observed in 1*T*-$TiSe_2$ at the same temperature, or Ta_2O_5. Additionally, the Raman spectrum experiences a dramatic change between ~140 and ~200 cm^{-1} resulting in a distinct spectrum: the peak at 192 cm^{-1} is completely diminished, the peak at 165 cm^{-1} has increased in intensity, and the peaks at 150 and 175 cm^{-1} have decreased in intensity. The peak 1*T*-$TaSe_2$ at 233 cm^{-1} experiences a shift to 229 cm^{-1} as well as a decrease in intensity. This new spectrum matches well to 3*R*-$TaSe_2$ (Figure 2.S4a) implying that the 1*T* to 3*R* phase transition has taken place. Further increasing the temperature to 400 °C reveals another significant change with all peaks between 140 and 200 cm^{-1} being either significantly or completely diminished, while new peaks have appeared at 138 and 206 cm^{-1}. Interestingly, the peak at 248 cm^{-1} seems to diminish in intensity, however, this may be due to the increased intensity of the peak that has shifted to 255 cm^{-1}. The Raman spectrum now matches to the room temperature 2*H*-$TaSe_2$ indicating that a second phase transition has occurred.[36] Once a temperature of 600 °C is reached, the Raman spectrum matches previously reported data for orthorhombic tantalum oxide (Ta_2O_5).[49-50] X-ray diffraction confirms that the Ta_2O_5 is in the orthorhombic phase (Figure 2.S4b). It is interesting that the observed Raman spectrum more closely resembles the orthorhombic instead of hexagonal phase of Ta_2O_5 since the hexagonal phase was observed by Cartamil-Bueno

2015 upon laser oxidation of 2*H*-$TaSe_2$.[51] However, their observation of the hexagonal phase may result from the relatively short (0.1-0.2 s) exposure time versus our longer oxidation time. According to a study by Perez 2017, the features at 115, 482, and 715 cm^{-1} after heating at 600 °C can be attributed to orthorhombic Ta_2O_5.[52] Our results here also differ from the amorphous oxide observed by Nguyen 2017 obtained after extended ambient storage.[53]

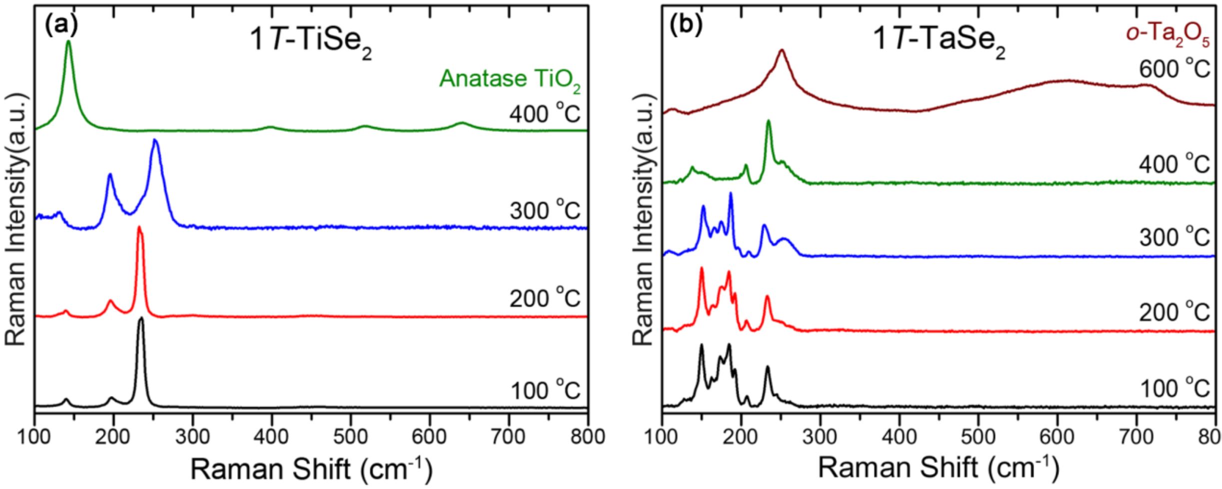

Figure 2.4 Raman spectra of (a) 1*T*-$TiSe_2$ and (b) 1*T*-$TaSe_2$ after heating single crystals in ambient atmosphere at increasing temperatures for 1 h. Complete transformation from the metal chalcogenide to the metal oxide is seen at 400 and 600 °C for 1*T*-$TiSe_2$ and 1*T*-$TaSe_2$, respectively.

At these elevated temperatures, it is also important to establish the extent of surface oxidation. Further studies were carried out for both 1*T*-$TiSe_2$ and 1*T*-$TaSe_2$ at the onset of oxidation (300 °C) and the temperature at which the surface was fully oxidized (400 and 600 °C, respectively) for 1 h, as found by Raman spectroscopy (Figure 2.5). Crystals from both systems were exposed to elevated temperatures before encasing in an epoxy mold with the c-axis of each crystal perpendicular to the epoxy surface, or an “on-edge” orientation to allow for cross-sectional characterization. SEM images of each crystal edge with corresponding EDS maps can be seen in Figure 2.6. From the obtained SEM images, the oxide layer thickness at each temperature was measured. At 300 °C, 1*T*-$TiSe_2$ was found to have an oxide layer approximately ~550-670 nm in thickness, while 1*T*-$TiSe_2$ heated at 400 °C possessed an oxide layer that varied in thickness depending on the crystal surface. The oxide layer exhibiting a regular thickness, Figure 2.6b, varied from ~4.7 µm to nearly 6.7 µm. Interestingly, there were areas with large variations in the oxide layer which were attributed to the quality of the crystal surface as seen in Figure 2.S7. 1*T*-$TaSe_2$ was also heated at 300 °C and possessed an oxide layer approximately 250-300 nm in thickness, less than 50% of the depth seen in 1*T*-$TiSe_2$ under the same conditions. In the crystals heated at 300°C, a separation between the oxide layer and the unoxidized crystal is evident most likely due to volume differences between the MX_2 and the oxide as observed by El-Bana 2013[27] and Chamlagain 2017.[34] In 1*T*-$TaSe_2$ heated at 600 °C for 1 h, an oxide layer was present, however, the oxidation continued beyond the surface oxide layer throughout the entire crystal, Figure 2.6d. The oxide layer at this temperature was approximately 1.5-2 µm in thickness. From this data, we conclude that these MX_2 materials will completely oxidize, leaving only the respective metal oxides, given significant time and thermal energy in air analogous to the complete oxidation reported previously for TaS_2 at 300 °C after 3 h.[34] In this study, the thermal energy was sufficient to induce complete oxidation of the 1*T*-$TiSe_2$ and 1*T*-$TaSe_2$ at 400 and 600 °C, respectively.

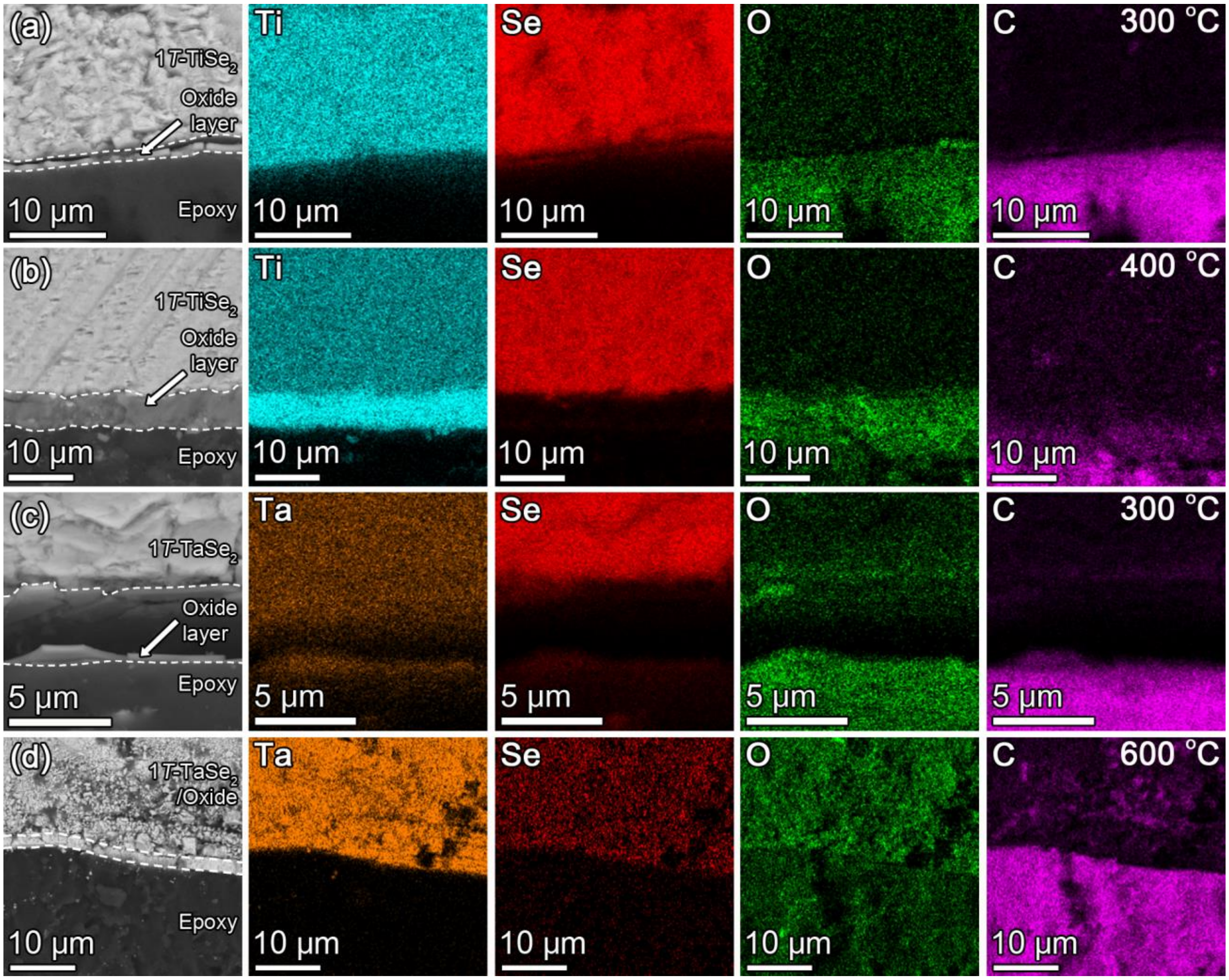

Figure 2.6 Cross-sectional SEM images and EDS maps of 1*T*-$TiSe_2$ at (a) 300 and (b) 400 °C, and 1*T*-$TaSe_2$ at (c) 300 and (d) 600 °C in epoxy molds. The dashed, white lines in the SEM images outline the area containing the surface oxide layer and any gap resulting from surface delamination.

The oxidative behavior of these materials over extended periods of time is important for many applications. Thus, six-hour heating intervals at various temperatures in air were carried out for 1*T*-$TiSe_2$, 1*T*-$TaSe_2$, and 2*H*-$TaSe_2$. Studies monitoring the oxidation behavior of 1*T*-$TiSe_2$ over 6 h intervals were first carried out followed by a comparison of 1*T* and 2*H*-$TaSe_2$ oxidation.

1*T*-$TiSe_2$ was heated for 6 h at 100, 125, 150, 175, and 200 °C; these temperatures were chosen due to the lower oxidative stability of 1*T*-$TiSe_2$ observed in the 1 h study. No deviation in the Raman spectra was observed between 100 and 175 °C, however, after heating at 200 °C for 6 h, the E_g peak of $TiSe_2$ at 233 cm^{-1} was greatly diminished and a new peak at 255 cm^{-1} became the dominant peak in the spectrum, analogous to the peak changes seen after heating at 300 °C for 1 h. The Raman spectra of 1*T*-$TiSe_2$ at 100 and 200 °C after 6 h can be seen in Figure 2.7. Backscatter SEM images of crystals after heating at 100 and 200 °C can be seen in Figure 2.S6b highlighting the $TiSe_2$ and TiO_2 areas. Surface oxidation after heating at 100 and 200 °C for 6 h is indicated by surface darkening in these images, while exposed areas, previously under the oxidized surface, exhibit a significantly lighter appearance. The oxidation after heating at 200 °C is much more pronounced as seen in both the SEM and Raman.

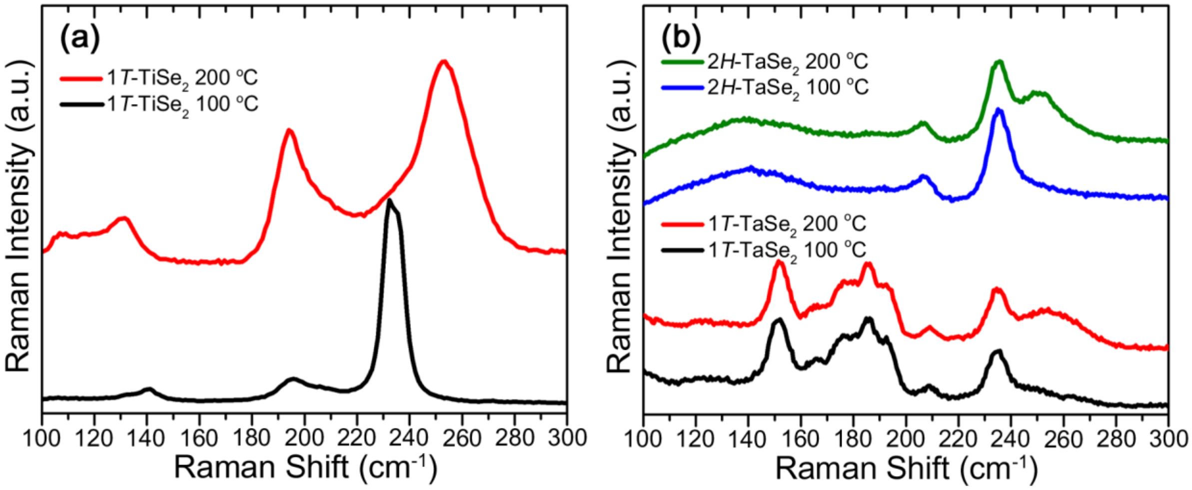

Figure 2.7 Raman spectra of (a) 1*T*-$TiSe_2$, and (b) 1*T*,2*H*-$TaSe_2$ crystals after exposure to 100 °C or 200 °C under ambient atmosphere for 6 hours. 1*T*-$TiSe_2$ displays a large degree of oxidation with the peak at 250 cm^{-1}, while both 1*T*- and 2*H*-$TaSe_2$ show less oxidation with a shoulder arising at 250 cm^{-1}.

EDS was performed on the oxidized and exposed surface sites of crystals at each temperature point; EDS results are summarized in Table 2.2. A trend of increased oxygen levels (from 26.2 to 55.3 atomic %) with temperature was observed in the atomic percentages of oxygen on the 1*T*-$TiSe_2$ surface. Surface oxidation is observed after heating for 6 h starting at 100 °C. Interestingly, the atomic percentage of oxygen under the oxidized surface remains low at all temperature points closely retaining the original 1:2 ratio of titanium to selenium. The SEM and EDS analyses confirm that oxidation is confined to the surface of the crystal when exposed to these temperatures in an ambient environment for 6 h. It is interesting, however, that surface oxidation is evident by SEM, yet not clearly visible in the Raman spectra until reaching 200 °C. This may be the result of an amorphous TiO_2 layer formation before crystallization at higher temperatures analogous to the crystallization of Ta_2O_5.[52]

Table 2.2 Atomic percentages of 1*T*-$TiSe_2$ as determined by EDS. Oxidized and exposed, fresh surface sites are shown for heating at 100, 125, 150, 175 and 200 °C for 6 h.

		Oxidized Surface			Exposed Surface		
		Ti	Se	O	Ti	Se	O
1*T*-$TiSe_2$	100 °C	25.7 %	48.2 %	26.2 %	31.6 %	60.3 %	0.7 %
	125 °C	18.9 %	38.3 %	42.8 %	32.4 %	59.8 %	4.7 %
	150 °C	21.0 %	40.4 %	38.7 %	32.1 %	63.5 %	4.4 %
	175 °C	18.9 %	30.8 %	50.3 %	33.9 %	61.5 %	4.6 %
	200 °C	22.6 %	22.0 %	55.3 %	31.9 %	65.3 %	2.8 %

The Raman spectrum of 1*T*-$TaSe_2$ after 6 h of 100 °C exposure also remained unchanged when compared to the unoxidized crystals. EDS was performed on both surface and edge sites as summarized in Table 2.3. The surface showed negligible oxygen content and maintained a 2:1

ratio of selenium to tantalum. At the edges, however, EDS revealed that 39.9% of the atoms were oxygen, indicating that oxidation occurs preferentially at these sites. This reactivity is expected because coordinately unsaturated metal atoms are present at edge sites. The edge-site oxidation is like that seen in 1*T*-$TiSe_2$, although, $TiSe_2$ seems to oxidize much more rapidly as evidenced by the atomic percentages of oxygen at 200 °C.

Table 2.3 Atomic percentages determined by EDS for surface and edge sites of $TaSe_2$ samples heated to 100 or 200 °C under ambient atmosphere for 6 h.

		Surface			Edge		
		Ta	Se	O	Ta	Se	O
1*T*-$TaSe_2$	100 °C	32.6%	67.4%	0.0%	19.6%	40.5%	39.9%
	200 °C	24.3%	55.4%	20.3%	24.8%	34.4%	40.8%
2*H*-$TaSe_2$	100 °C	28.1%	71.9%	0.0%	20.2%	43.9%	35.9%
	200 °C	30.4%	58.7%	10.9%	23.3%	46.6%	30.1%

After 6 h of heating 1*T*-$TaSe_2$ samples at 200 °C in air, significant oxidation was observed at the crystal edges (40.8 atomic % oxygen), while some oxidation was observed on the surface (20.3 atomic %. oxygen). Additionally, small crystallites were observed to grow from edge sites (Figure 2.8a,b) that were composed of 95.5 atomic % of selenium, indicating that displaced selenium migrates and crystallizes on the outer surface as the 1*T*-$TaSe_2$ is oxidized. These crystallites were mainly observed at or near edge sites. To characterize oxide layer formation, 1*T*-$TaSe_2$ crystals were heated at 300 °C for 6 h for a direct comparison to crystals heated at the same temperature for 1 h. SEM revealed an oxide layer that was similar in appearance, with moderate delamination from the remaining $TaSe_2$. Although, the oxide layer was ~1.6-1.8 µm in thickness, a nearly six-fold increase when compared to the oxide layer observed after heating at 300 °C for 1 h. This oxide layer, however, was quite similar in thickness to that observed after heating at 600 °C for 1 h. The SEM images and corresponding EDS maps of the 300 °C, 6 h heating can be found in Figure 2.S7.

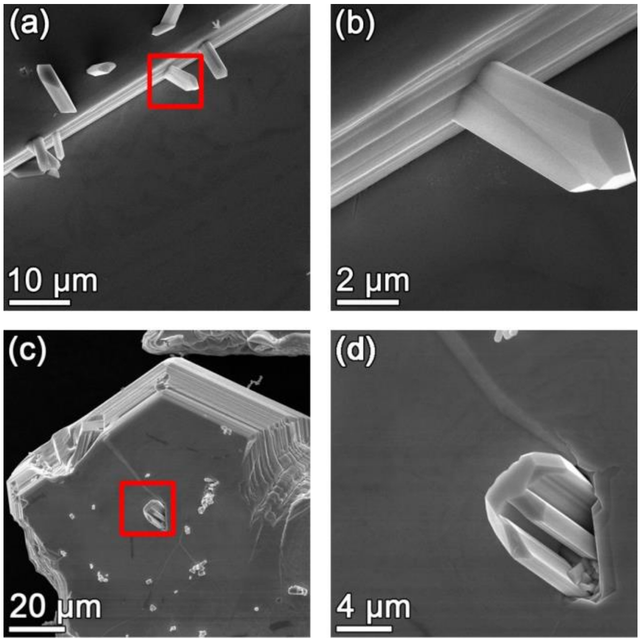

Figure 2.8 Crystals of $TaSe_2$ heated under ambient atmosphere at 200 °C for 6 h. Se crystals (a,b) emerge from edges in 1*T*-$TaSe_2$ after oxidation, while crystals of *o*-Ta_2O_5 (c,d) protrude from defect or edge sites of 2*H*,3*R*-$TaSe_2$. The red box in (a) and (c) indicate the areas shown in (b) and (d), respectively.

Crystals comprised of a mixture of two polytypes, 2*H*,3*R*-$TaSe_2$, were also heated in air for 6 h at 100 °C and 200 °C. As with the 1*T*-$TaSe_2$ form, at 100 °C no surface oxidation was observed by EDS analysis, however, a similar amount of oxidation was observed at the edge sites (35.9 atomic % oxygen). After heating 2*H*,3*R*-$TaSe_2$ crystals at 200 °C for 6 h, minor surface oxidation was observed (10.9 atomic % oxygen), while edge sites showed relatively significant oxidation (30.1 atomic % oxygen) like the analogous 1*T* crystals. However, the SEM images in Figure 2.8c,d clearly show crystals growing from defects and edges of the crystals. In contrast to the protrusions found on the 1*T*-$TaSe_2$ crystals heated at 200 °C, these protrusions showed little selenium (6.6 atomic %) and were mostly composed of tantalum (45.8 atomic %) and oxygen (47.6 atomic %).

It is interesting that different MX_2 materials, and even polymorphs of the same MX_2, show different oxidation behaviors. As discussed above, the oxidation of titanium and tantalum diselenide forms a layer of metal oxide on the surface, while excess selenium migrates out of the structure before crystallizing. Selenium was seen to crystallize on the outer surfaces, mainly at edge sites, in 1*T*-$TiSe_2$ and 1*T*-$TaSe_2$; in contrast, protrusions of tantalum oxide were observed forming at edge and defect sites in 2*H*,3*R*-$TaSe_2$. Raman spectroscopy of both $TiSe_2$ and $TaSe_2$ crystals shows no obvious change after heating at 100 °C for 6 h. After heating at 200 °C for 6 h however, 1*T*-$TiSe_2$, 1*T*-$TaSe_2$ and 2*H*-$TaSe_2$ all show the growth of a peak around 250 cm^{-1} (Figure 2.7) like those seen in the 1 h oxidation studies in Figure 2.5. The 250 cm^{-1} can be attributed to the A_{1g} peak of Se,[46] but also matches relatively well with the Ta_2O_5 peak around 255 cm^{-1}.[52] This finding indicates that samples of all three materials are not surface stable for an extended time in air, even at relatively low temperatures. Yu 2015 verified this with optical contrast versus the number of layers in few-layered 1*T*-TaS_2 flakes under ambient conditions. A decreasing, linear trend of the number of layers was observed with decreased contrast implying oxidative degradation over time.[54]

Related MX_2 oxidation studies on other well-known systems reveal similar results with varied oxidation stability. Moore et al. addressed the oxidation of several systems including the selenides of Ta, W, Mo, Re, and Nb observed with TGA. It was found that the oxidation onset temperatures were 579, 541, 479, 435, and 410 °C, respectively, significantly above the 300 °C oxidation found in this study.[19] This discrepancy most likely arises from the short amount of time at each temperature throughout the TGA analysis when compared to the 1 and 6 h hold times used in this study. Godfrey and Nelson monitored the oxidation of MoS_2 films for extended times with XRD finding no film oxidation below ~400 °C after 30 min, however, complete oxidation was observed at 482 °C after 30 min based on the observed color change.[20] These observations of MoS_2 reveal a similar oxidation rate, yet higher onset temperature than 1*T*-$TiSe_2$, but a much quicker, oxidation rate than 1*T*-$TaSe_2$. The relative humidity of ambient air also has been shown to greatly influence oxidation in these materials which could account for some of the differences between oxidation temperatures reported here and previously.[19, 55] Moore et al. demonstrated this comparing oxidation in dry and "moist" air[19]; this experiment was carried out with a relative humidity between 60 and 80%.

A self-limiting oxidation at temperatures below 100 °C under ozone exposure in WSe_2 was found by Yamamoto and coworkers. Oxidation was confined to the top-most surface layers with oxidation beginning at edges and surface defect sites.[28] Liu and coworkers found significant surface oxidation in WSe_2 beginning at 400 °C after 1 h starting at edges and working over the surface with total surface oxidation after 2 h.[24] Both sets of results for WSe_2 are quite similar to our observations reported here for 1*T*-$TiSe_2$ and 1*T*-$TaSe_2$.

The use of a capping material is one way to effectively mitigate oxidation effects in low-dimensional materials. Graphene and *h*-BN are two such capping materials; *h*-BN has been demonstrated as an efficacious capping agent for two-dimensional materials.[56-57] Shin and coworkers successfully demonstrated not only the elimination of oxidation, but also the reduction in photodegradation of $MoSe_2$ and WSe_2 with the use of *h*-BN. In their study, a three-layer cap of *h*-BN was found to sufficiently passivate the MX_2 materials.[58] Although, effective capping of these materials is a necessity. Nguyen 2017 observed this when capping $NbSe_2$ with graphene; a "wrinkle" in the graphene layer permitted oxidation of the exposed $NbSe_2$ section to Nb_2O_5 over the span of four months.[53] Thus, a capping material, such as graphene or *h*-BN, is a necessity to prevent 1*T*-$TiSe_2$ or 1*T*-$TaSe_2$ oxidation when creating low-dimensional devices.

1*T*-$TaSe_2$ → 2*H*-$TaSe_2$ Transformation. After 4 months of storage at ambient (benchtop) conditions, the originally golden 1*T*-$TaSe_2$ crystals turned gray in color. Under SEM, the surfaces of these aged crystals appeared to be much rougher than those of the smooth surfaces of freshly grown 1*T*-$TaSe_2$ crystals, see Figure 2.S9. Removal of the surface, however, revealed newly exposed material with the golden color and smooth appearance of the freshly grown 1*T*-$TaSe_2$

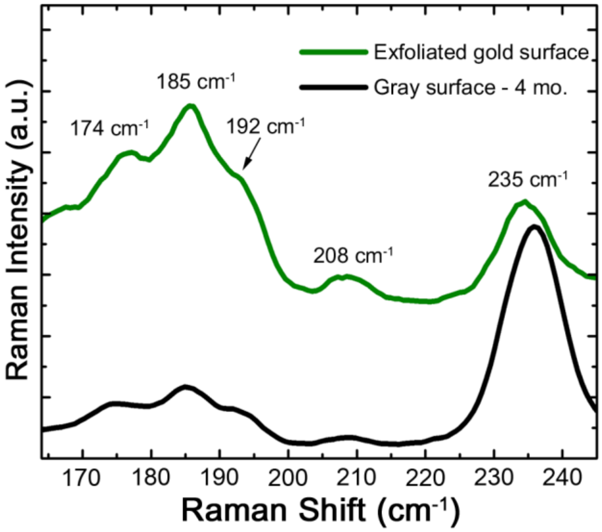

Figure 2.10 Raman spectra of 1*T*-$TaSe_2$ crystals after exposure to ambient conditions for 4 months (black) and the newly exposed golden surface (green).

crystals. EDS analysis of the aged surface provided atomic percentages of 28.6% tantalum, 55.1% selenium, and 16.3% oxygen, whereas analysis of newly exposed surface provided atomic percentages of 32.8% tantalum, 63.2% selenium, and 4.0% oxygen, indicating that oxidation is mainly confined to the surface.

To further examine changes to the crystal surface after prolonged, ambient exposure, Raman spectroscopy was performed on aged and newly exposed surfaces (Figure 2.10). The newly exposed surface shows peaks corresponding to the 1*T*-$TaSe_2$ form at 174, 185, and 192 cm^{-1} and smaller peaks at 208 and 235 cm^{-1}, congruent with previous Raman spectra of freshly grown 1*T*-$TaSe_2$ (Figure 2.S4a). The 4-month-aged surface, on the other hand, exhibited a dramatic change in peak intensities: the peak at 235 cm^{-1} is now dominant. The spectrum now exhibits characteristics of both 1*T* and 2*H*-$TaSe_2$ implying that both polymorphs are present. Thus, the prolonged exposure to ambient conditions provided sufficient energy to partially transform the surface from 1*T* to 2*H*-$TaSe_2$ in addition to oxidizing the surface. This conclusion is supported by the obvious color change from gold to gray after exposure, as well as the reappearance of golden material after surface removal to reveal fresh 1*T*-$TaSe_2$. Further, a dramatic reduction in the characteristic, 175 and 186 cm^{-1} Raman peaks, corresponding to the E_g and A_{1g} peaks of 1*T*-$TaSe_2$, was observed after just one week. These spectra can be seen in Figure 2.S10.

Conclusions

The oxidative behaviors of the $TiSe_2$ and $TaSe_2$ systems was explored revealing various pathways for oxidation to occur. Surface oxidation in 1*T*-$TiSe_2$ and 1*T*-$TaSe_2$ occurred upon heating in air at temperatures in excess of 300 °C after only 1 h with full oxidation occurring at 400 and 600 °C, respectively. 1*T*-$TaSe_2$ also exhibited polymorph changes to the 3*R* and then the

2*H* phases at 300 and 400 °C after 1 h, respectively. In addition, heating at 200 °C for several hours induced surface oxidation in both materials. When left in ambient conditions over long periods of time, surface oxidation occurs on 1*T*-$TiSe_2$, 1*T*-$TaSe_2$ and 2*H*-$TaSe_2$ as revealed by Raman spectroscopy. Oxidation in these materials initially occurs at edge sites, likely due to the presence of coordinately unsaturated metal atoms. Additionally, 1*T*-$TaSe_2$ crystals stored in ambient conditions for several months exhibited surface layer transformation to the 2*H*-$TaSe_2$ polymorph. However, both surface oxidation and polymorph transformation of $TaSe_2$ were restricted to the crystal surface and could be removed by delaminating surface layers.

These studies on the surface of heated and/or aged $TiSe_2$ and $TaSe_2$ crystals indicate that, if not stored under an inert atmosphere at ambient temperature, these crystals will become impure over time either through oxidation or transformation to a different polymorph. However, both conversions occur at the crystal surface, and thus, the unoxidized inner crystal can be exposed again by removal of the surface layers through methods such as delamination. To prevent these oxidative processes, the use of a capping material, such as graphene or *h*-BN, is necessary. By carefully controlling the material synthesis and utilizing proper storage precautions, fundamental studies of titanium and tantalum diselenide can be undertaken to greatly impact the world of future electronics.

Supplemental Information

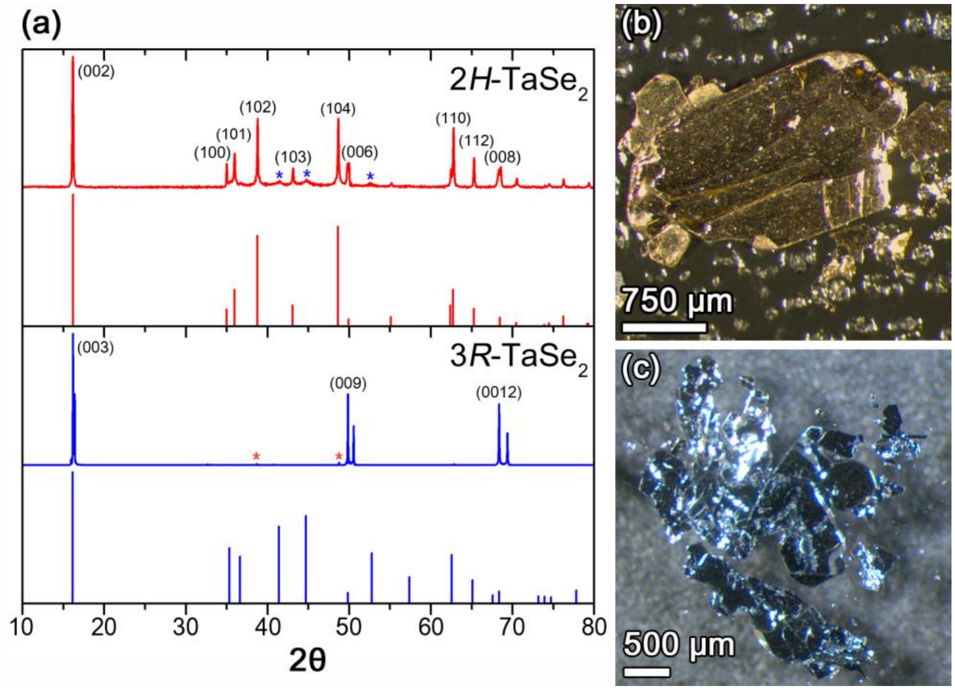

Figure 2.S1 PXRD patterns of (a) 2*H*-$TaSe_2$ and (b) 3*R*-$TaSe_2$ after CVT with the patterns matching to 2*H*-$TaSe_2$ (04-003-6787) and 3*R*-$TaSe_2$ (03-065-3567), respectively. Asterisks mark trace 2*H*-$TaSe_2$ (red) and 3*R*-$TaSe_2$ (blue) impurities where indicated. Optical images of (b) golden 1*T*-$TaSe_2$ crystals and (c) silver 2*H*-$TaSe_2$ crystals.

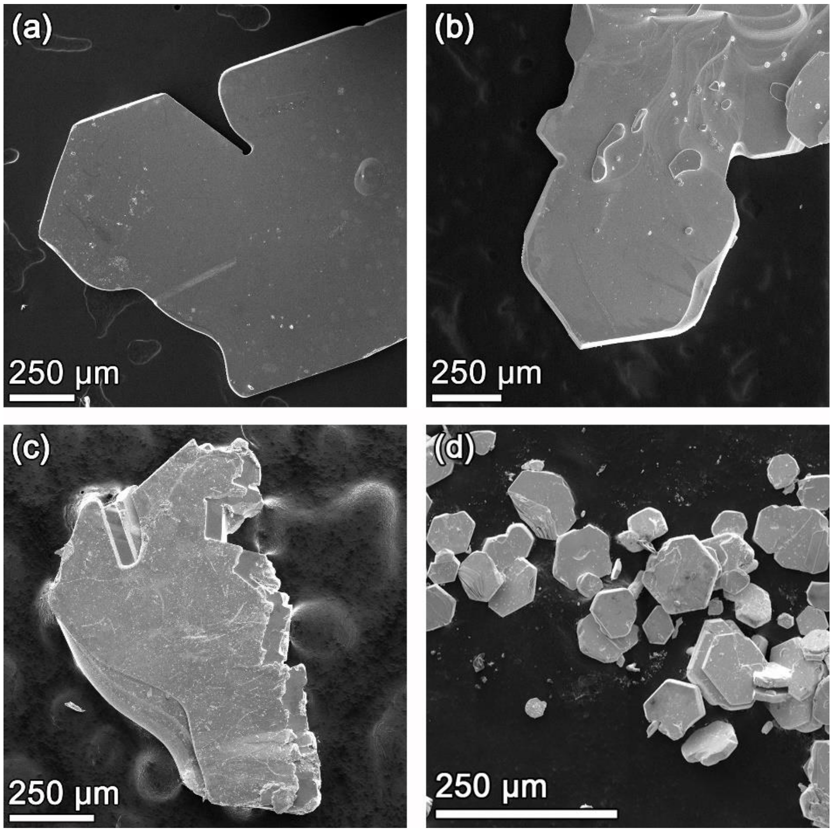

Figure 2.S2 SEM images of (a) 1*T*-$TiSe_2$, (b) 1*T*-$TaSe_2$, (c) 2*H*-$TaSe_2$, and (d) 3*R*-$TaSe_2$ crystals.

Table 2.S1 EDS data from 1*T*-$TiSe_2$ and 1*T*-$TaSe_2$ crystals shown in atomic percentages.

	1*T*-$TiSe_2$		**1*T*-$TaSe_2$**	
	Theor. at%	Exp. at%	Theor. at%[43]	Exp. Wt%
Ti	33.3	31.9	-	-
Ta	-	-	33.3	35.1
Se	66.7	68.1	66.7	64.9

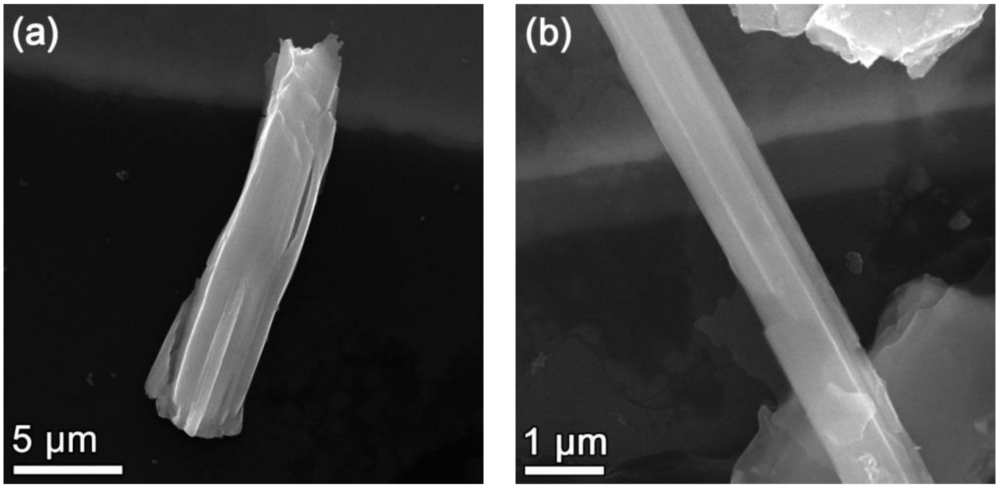

Figure 2.S3 SEM images of the iodine-doped rods (Figure 2.3b,c) after disassociation from crystal edges through sonication in isopropyl alcohol.

Table 2.S2 EDS data for iodine-doped rods. The Ta:Se ratio is observed to skew from a 1:2 ratio to a nearly 1:3 ratio. With the inclusion of iodine, the formula can be approximated as $Ta_{2.3}Se_{7.1}I_1$. This formula is like that observed by Gressier et. al.[59]

Element	**At %**
Ta	22.3
Se	68.1
I	9.6

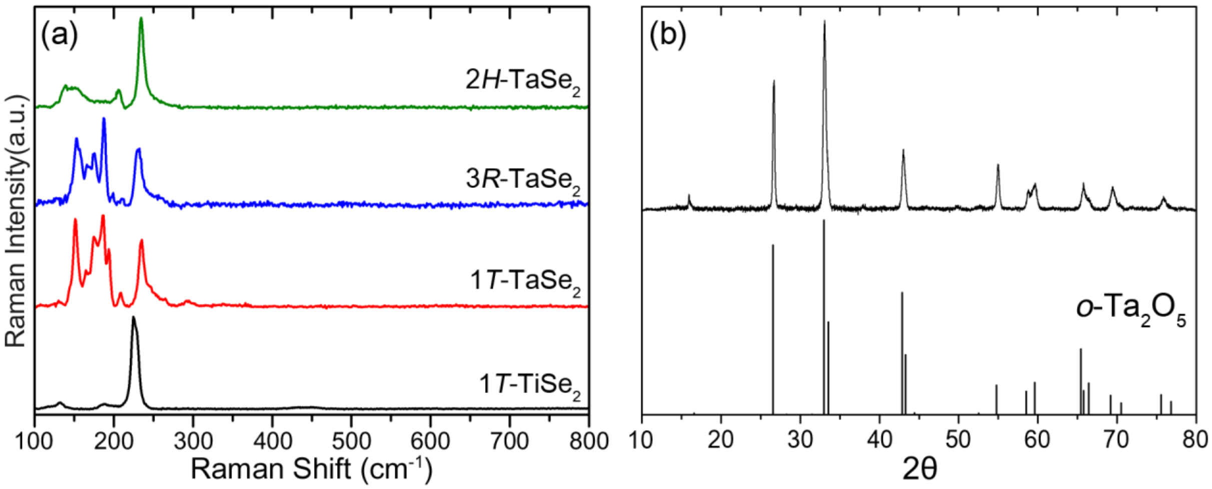

Figure 2.S4 (a) Raman spectra of 1T-TiSe$_2$, 1T-TaSe$_2$, 3R-TaSe$_2$, and 2H-TaSe$_2$ at room temperature. (b) PXRD of TaSe$_2$ heated at 600 °C for 1 h matching to o-Ta$_2$O$_5$ (ICDD 04-013-9608).

Table 2.S3 EDS data for 1T-TiSe$_2$ after heating in air for 1 h. The values below are the relative atomic % for each element at the specified temperature.

		Oxidized Surface			Exposed Surface		
		Ti	Se	O	Ti	Se	O
1T-TiSe$_2$	100 °C	28.9%	56.3%	10.6%	36.7 %	61.4 %	1.9 %
	200 °C	28.9%	57.2%	13.9%	33.7 %	63.0 %	3.3 %
	300 °C	24.1%	13.0%	62.9%	33.2 %	61.9 %	4.9 %
	400 °C	14.3%	3.1%	82.7%	-	-	-

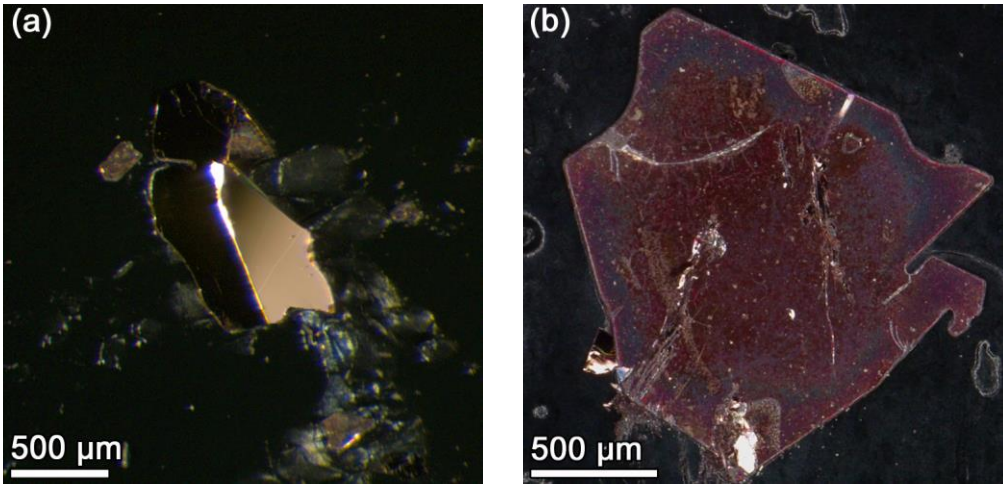

Figure 2.S5 Optical images of an oxidized 1*T*-$TiSe_2$ flake. Oxidation, distinguished by the matte finish, is evident over the entire surface (a); more extensive oxidation toward the edges of the flake is evidenced by the iridescent coloration. This unique coloration results from the formation of a thin film of TiO_2. The oxidation, however, is restricted to the surface; fresh 1*T*-$TiSe_2$ can be seen in (b) where the oxidized surface has been mechanically removed.

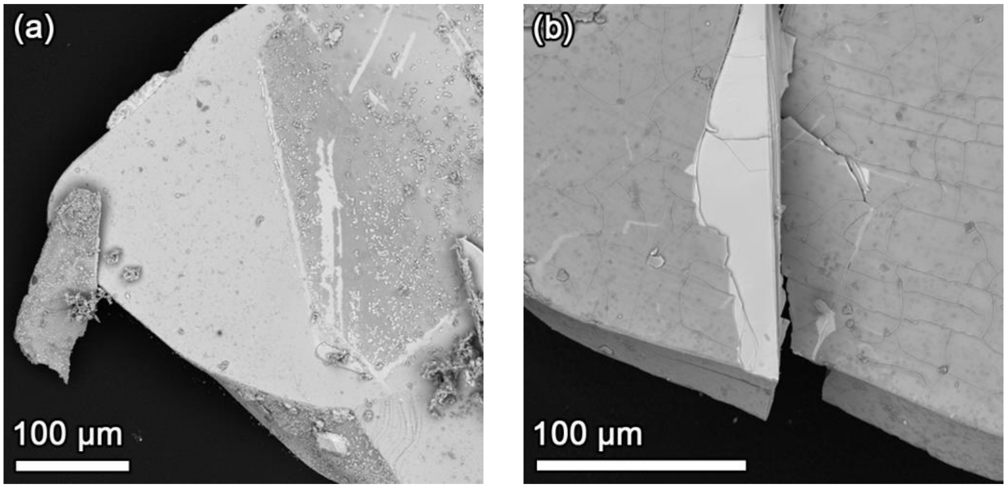

Figure 2.S6 SEM images of 1*T*-$TiSe_2$ after heating at (a) 100 °C and (b) 200 °C for 6 h. The change in contrast highlights freshly exposed 1*T*-$TiSe_2$ (lighter) versus the oxidized surface (darker). At 200 °C, the surface is a single, continuous oxide layer.

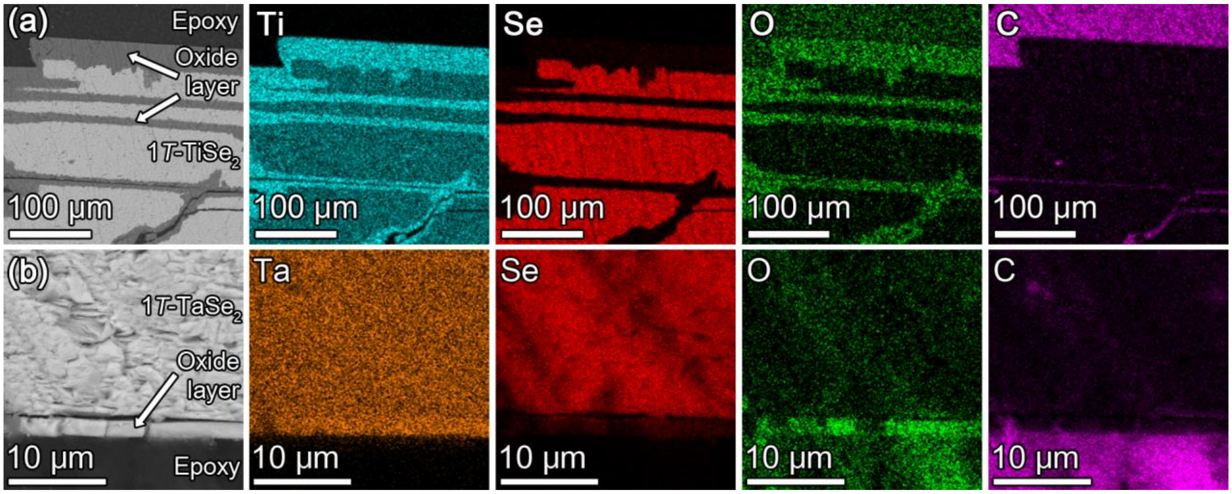

Figure 2.S7 SEM image and corresponding EDS maps for (a) 1*T*-$TiSe_2$ heated at 400 °C for 1 h, and (b) 1*T*-$TaSe_2$ heated at 300 °C for 6 h. The 1*T*-$TiSe_2$ images reveal veins of oxidation throughout the crystal indicating that oxidation starts at defects and surface cracks.

Figure 2.S8 Optical image of 1*T*-$TaSe_2$ crystals agglomerated during CVT and aged 2 years in Ar environment at room temperature. Much of the golden, 1*T*-$TaSe_2$ phase has transformed to the 2*H*,3*R* phases indicated by the overall gray color, however, some 1*T*- crystals remain visible throughout the agglomeration of crystals shown.

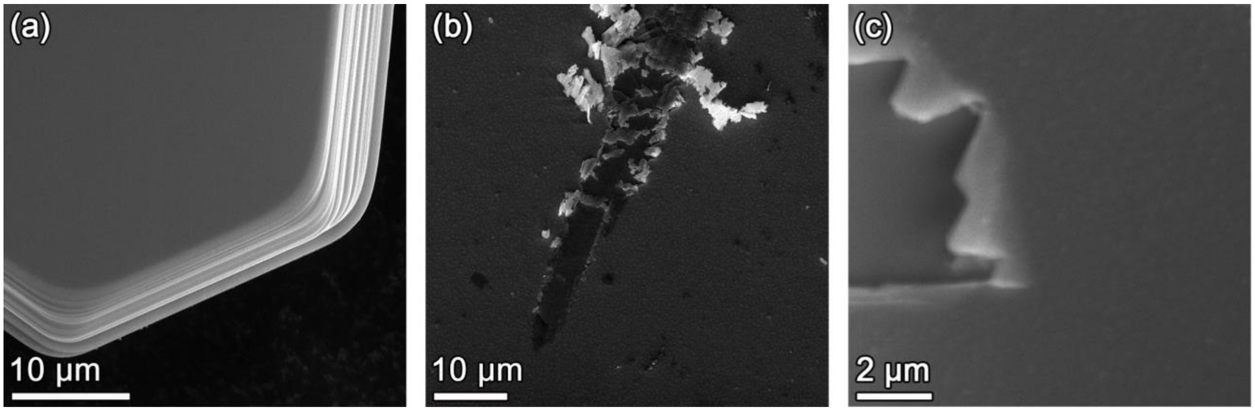

Figure 2.S9 SEM images of 1*T*-TaSe$_2$ (a) freshly grown, and (b,c) after exposure to ambient conditions for 4 months. Removal of the surface layer reveals the preserved, smooth 1*T*-TaSe$_2$ underneath.

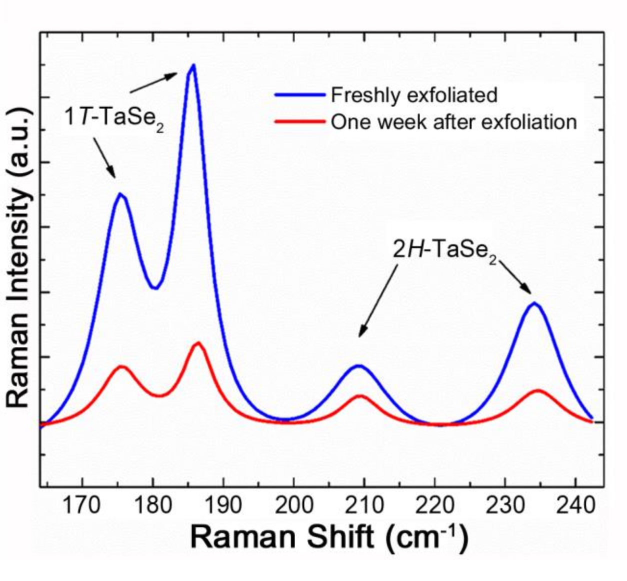

Figure 2.S10 Raman spectra of 1*T*-TaSe$_2$ crystals immediately following (blue) and 1 week after (red) mechanical exfoliation. These spectra were obtained under 633 nm laser excitation at room temperature.

References

1. Luo, H.; Xie, W.; Tao, J.; Inoue, H.; Gyenis, A.; Krizan, J. W.; Yazdani, A.; Zhu, Y.; Cava, R. J., *P. Natl. Acad. Sci. USA* **2015,** *112* (11), E1174-E1180.

2. Ozaydin, H. D.; Sahin, H.; Kang, J.; Peeters, F. M.; Senger, R. T., *2D Mater.* **2015,** *2* (4), 044002.

3. Gruner, G., *Rev. Mod. Phys.* **1988,** *60* (4), 1129-1182.

4. Moncton, D. E.; Axe, J. D.; Disalvo, F. J., *Phys. Rev. Lett.* **1975,** *34* (12), 734-737.

5. Dordevic, S. V.; Basov, D. N.; Dynes, R. C.; Ruzicka, B.; Vescoli, V.; Degiorgi, L.; Berger, H.; Gaál, R.; Forró, L.; Bucher, E., *Eur. Phys. J. B* **2003,** *33* (1), 15-23.

6. Li, L. J.; Zhao, W. J.; Liu, B.; Ren, T. H.; Eda, G.; Loh, K. P., *Appl. Phys. Lett.* **2016,** *109* (14), 141902.

7. Chen, P.; Chan, Y. H.; Fang, X. Y.; Zhang, Y.; Chou, M. Y.; Mo, S. K.; Hussain, Z.; Fedorov, A. V.; Chiang, T. C., *Nat. Commun.* **2015,** *6*, 8943.

8. Sugawara, K.; Nakata, Y.; Shimizu, R.; Han, P.; Hitosugi, T.; Sato, T.; Takahashi, T., *ACS Nano* **2016,** *10* (1), 1341-1345.

9. Lopez-Sanchez, O.; Lembke, D.; Kayci, M.; Radenovic, A.; Kis, A., *Nat. Nano* **2013,** *8* (7), 497-501.

10. Mak, K. F.; Lee, C.; Hone, J.; Shan, J.; Heinz, T. F., *Phys. Rev. Lett.* **2010,** *105* (13), 136805.

11. Goli, P.; Khan, J.; Wickramaratne, D.; Lake, R. K.; Balandin, A. A., *Nano Lett.* **2012,** *12* (11), 5941-5945.

12. Tsen, A. W.; Hovden, R.; Wang, D.; Kim, Y. D.; Okamoto, J.; Spoth, K. A.; Liu, Y.; Lu, W.; Sun, Y.; Hone, J. C.; Kourkoutis, L. F.; Kim, P.; Pasupathy, A. N., *P. Natl. Acad. Sci. USA* **2015,** *112* (49), 15054-15059.

13. Rasch, J.; Stemmler, T.; Manzke, R., *J. Alloy. Compd.* **2007,** *442* (1–2), 262-264.

14. Ramsdell, L. S., Studies on silicon carbide. *Am. Mineral.* **1947,** *32* (1-2), 64-82.

15. Lieth, R. M. A.; Terhell, J. C. J. M., Transition Metal Dichalcogenides. In *Preparation and Crystal Growth of Materials with Layered Structures*, Lieth, R. M. A., Ed. Springer Netherlands: Dordrecht, 1977; pp 141-223.

16. Yan, J.-A.; Cruz, M. A. D.; Cook, B.; Varga, K., *Sci. Rep. UK* **2015,** *5*, 16646.

17. Wilson, J. A.; Di Salvo, F. J.; Mahajan, S., *Phys. Rev. Lett.* **1974,** *32* (16), 882-885.

18. Sankar, R.; Narsinga Rao, G.; Muthuselvam, I. P.; Butler, C.; Kumar, N.; Senthil Murugan, G.; Shekhar, C.; Chang, T.-R.; Wen, C.-Y.; Chen, C.-W.; Lee, W.-L.; Lin, M. T.; Jeng, H.-T.; Felser, C.; Chou, F. C., *Chem. Mater.* **2017,** *29* (2), 699-707.

19. Lavik, M. T.; Medved, T. M.; Moore, G. D., *ASLE Trans.* **1968,** *11* (1), 44-55.

20. Godfrey, D.; Nelson, E. C., Oxidation Characteristics of Molybdenum Disulfide and Effect of Such Oxidation on its Role as a Solid-Film Lubricant. Aeronautics, N. A. C. f., Ed. Lewis Flight Propulsion Lab; Cleveland OH, United States, 1949; p 30.

21. Song, X.; Guo, Z.; Zhang, Q.; Zhou, P.; Bao, W.; Zhang, D. W., *Small* **2017,** *13* (35).

22. Gao, J.; Li, B.; Tan, J.; Chow, P.; Lu, T.-M.; Koratkar, N., *ACS Nano* **2016,** *10* (2), 2628-2635.

23. Wang, Z.; Zhang, Y.-J.; Liu, M.; Peterson, A.; Hurt, R. H., *Nanoscale* **2017,** *9* (17), 5398-5403.

24. Liu, Y.; Tan, C.; Chou, H.; Nayak, A.; Wu, D.; Ghosh, R.; Chang, H.-Y.; Hao, Y.; Wang, X.; Kim, J.-S.; Piner, R.; Ruoff, R. S.; Akinwande, D.; Lai, K., *Nano Lett.* **2015,** *15* (8), 4979-4984.

25. Woods, J. M.; Shen, J.; Kumaravadivel, P.; Pang, Y.; Xie, Y.; Pan, G. A.; Li, M.; Altman, E. I.; Lu, L.; Cha, J. J., *ACS Appl. Mater. Inter.* **2017,** *9* (27), 23175-23180.

26. Chae, S. H.; Jin, Y.; Kim, T. S.; Chung, D. S.; Na, H.; Nam, H.; Kim, H.; Perello, D. J.; Jeong, H. Y.; Ly, T. H.; Lee, Y. H., *ACS Nano* **2016,** *10* (1), 1309-1316.

27. El-Bana, M. S.; Wolverson, D.; Russo, S.; Balakrishnan, G.; Paul, D. M.; Bending, S. J., *Supercond. Sci. Tech.* **2013,** *26* (12), 125020.

28. Yamamoto, M.; Dutta, S.; Aikawa, S.; Nakaharai, S.; Wakabayashi, K.; Fuhrer, M. S.; Ueno, K.; Tsukagoshi, K., *Nano Lett.* **2015,** *15* (3), 2067-2073.

29. Li, Z.; Yang, S.; Dhall, R.; Kosmowska, E.; Shi, H.; Chatzakis, I.; Cronin, S. B., Layer *ACS Nano* **2016,** *10* (7), 6836-6842.

30. Lu, J.; Carvalho, A.; Chan, X. K.; Liu, H.; Liu, B.; Tok, E. S.; Loh, K. P.; Castro Neto, A. H.; Sow, C. H., *Nano Lett.* **2015,** *15* (5), 3524-3532.

31. Cucinotta, C. S.; Dolui, K.; Pettersson, H.; Ramasse, Q. M.; Long, E.; O’Brian, S. E.; Nicolosi, V.; Sanvito, S., *J. Phys. Chem. C* **2015,** *119* (27), 15707-15715.

32. Chen, L.; Feng, Y.; Zhou, X.; Zhang, Q.; Nie, W.; Wang, W.; Zhang, Y.; He, C., *ACS Appl. Mater. Inter.* **2017,** *9* (20), 17347-17358.

33. Han, J. H.; Lee, S.; Yoo, D.; Lee, J.-H.; Jeong, S.; Kim, J.-G.; Cheon, J., *J. Am. Chem. Soc.* **2013,** *135* (10), 3736-3739.

34. Chamlagain, B.; Cui, Q.; Paudel, S.; Cheng, M. M.-C.; Chen, P.-Y.; Zhou, Z., *2D Mater.* **2017,** *4* (3), 031002.

35. Pinilla-Cienfuegos, E.; Mañas-Valero, S.; Navarro-Moratalla, E.; Tatay, S.; Forment-Aliaga, A.; Coronado, E., *Appl. Sci.* **2016,** *6* (9), 250.

36. Yan, Z.; Jiang, C.; Pope, T. R.; Tsang, C. F.; Stickney, J. L.; Goli, P.; Renteria, J.; Salguero, T. T.; Balandin, A. A., *J. Appl. Phys.* **2013,** *114* (20), 204301.

37. *Preparation and crystal growth of materials with layered structures*. D. Reidel Publishing Company: Dordrecht, Holland, 1977; Vol. 1, p 280.

38. Revelli Jr, J. F.; Phillips, W. A., *J. Solid State Chem.* **1974,** *9* (2), 176–186.

39. Yan, Y.; Xia, B.; Ge, X.; Liu, Z.; Wang, J.-Y.; Wang, X., *ACS Appl. Mater. Inter.* **2013,** *5* (24), 12794-12798.

40. Renteria, J.; Samnakay, R.; Jiang, C.; Pope, T. R.; Goli, P.; Yan, Z.; Wickramaratne, D.; Salguero, T. T.; Khitun, A. G.; Lake, R. K.; Balandin, A. A., *J. Appl. Phys.* **2014,** *115* (3), 034305.

41. Huisman, R.; Jellinek, F., *J. Less-Common Met.* **1969,** *17* (1), 111-117.

42. Bjerkelund, E.; Kjekshus, A., *Acta Chem. Scand.* **1967,** *21* (2).

43. Samnakay, R.; Wickramaratne, D.; Pope, T. R.; Lake, R. K.; Salguero, T. T.; Balandin, A. A., *Nano Lett.* **2015,** *15* (5), 2965-2973.

44. Di Salvo, F. J.; Moncton, D.; Waszczak, J., *Phys. Rev. B* **1976,** *14* (10), 4321.

45. Cava, R. J.; Littlewood, P.; Fleming, R. M.; Dunn, R. G.; Rietman, E. A., *Phys. Rev. B* **1986,** *33* (4), 2439-2443.

46. Baganich, A. A.; Mikla, V. I.; Semak, D. G.; Sokolov, A. P.; Shebanin, A. P., *Phys. Status Solidi B* **1991,** *166* (1), 297-302.

47. Hanaor, D. A. H.; Sorrell, C. C., *J. Mater. Sci.* **2011,** *46* (4), 855-874.

48. Long, E.; O'Brien, S.; Lewis, E. A.; Prestat, E.; Downing, C.; Cucinotta, C. S.; Sanvito, S.; Haigh, S. J.; Nicolosi, V., *NPJ 2D Mater. Appl.* **2017,** *1* (1), 22.

49. Joseph, C.; Bourson, P.; Fontana, M. D., *J. Raman Spectrosc.* **2012,** *43* (8), 1146-1150.

50. Krishnan, R. R.; Gopchandran, K. G.; MahadevanPillai, V. P.; Ganesan, V.; Sathe, V., *Appl. Surf. Sci.* **2009,** *255* (16), 7126-7135.

51. Cartamil-Bueno, S. J.; Steeneken, P. G.; Tichelaar, F. D.; Navarro-Moratalla, E.; Venstra, W. J.; van Leeuwen, R.; Coronado, E.; van der Zant, H. S. J.; Steele, G. A.; Castellanos-Gomez, A., *Nano Res.* **2015,** *8* (9), 2842-2849.

52. Perez, I.; Enríquez Carrejo, J. L.; Sosa, V.; Perera, F. G.; Farias Mancillas, J. R.; Elizalde Galindo, J. T.; Rodríguez Rodríguez, C. I., *J. Alloy. Compd.* **2017,** *712*, 303-310.

53. Nguyen, L.; Komsa, H.-P.; Khestanova, E.; Kashtiban, R. J.; Peters, J. J. P.; Lawlor, S.; Sanchez, A. M.; Sloan, J.; Gorbachev, R. V.; Grigorieva, I. V.; Krasheninnikov, A. V.; Haigh, S. J., *ACS Nano* **2017,** *11* (3), 2894-2904.

54. Yu, Y.; Yang, F.; Lu, X. F.; Yan, Y. J.; ChoYong, H.; Ma, L.; Niu, X.; Kim, S.; Son, Y.-W.; Feng, D.; Li, S.; Cheong, S.-W.; Chen, X. H.; Zhang, Y., *Nat. Nano* **2015,** *10* (3), 270-276.

55. Windom, B. C.; Sawyer, W. G.; Hahn, D. W., *Tribol. Lett.* **2011,** *42* (3), 301-310.

56. Doganov, R. A.; O'Farrell, E. C. T.; Koenig, S. P.; Yeo, Y.; Ziletti, A.; Carvalho, A.; Campbell, D. K.; Coker, D. F.; Watanabe, K.; Taniguchi, T.; Neto, A. H. C.; Özyilmaz, B., *Nat. Commun.* **2015,** *6*, 6647.

57. Wang, L.; Meric, I.; Huang, P. Y.; Gao, Q.; Gao, Y.; Tran, H.; Taniguchi, T.; Watanabe, K.; Campos, L. M.; Muller, D. A.; Guo, J.; Kim, P.; Hone, J.; Shepard, K. L.; Dean, C. R., *Science* **2013,** *342* (6158), 614-617.

58. Ahn, S.; Kim, G.; Nayak, P. K.; Yoon, S. I.; Lim, H.; Shin, H.-J.; Shin, H. S., *ACS Nano* **2016,** *10* (9), 8973-8979.

59. Gressier, P.; Guemas, L.; Meerschaut, A., *Acta Crystallogr. B* **1982,** *38* (11), 2877-2879.

CHAPTER 3

PHASE CHANGE BEHAVIOR OF 1*T*-TaSe$_2$

Matthew A. Bloodgood, Protik Das, Roger Lake, Alexander A. Balandin, Tina T. Salguero. *To be submitted to the Journal of Physical Chemistry C.*

Abstract

The metallic transition metal dichalcogenide $TaSe_2$ is of interest for future electronics applications, however, several polymorphs of $TaSe_2$ exist. The metastable, 1*T* polymorph is especially interesting due to the above-room-temperature charge density wave transitions. It is prudent to understand the polymorphic stability and transitions of 1*T*-$TaSe_2$ at elevated temperatures. This chapter addresses the various phase transitions in 1*T*-$TaSe_2$ between room temperature and 1000 °C. Upon heating, golden 1*T*-$TaSe_2$ first transforms irreversibly into silver 3*R*-$TaSe_2$, then to 2*H*-$TaSe_2$ in the temperature range 310–450 °C. These transitions are followed by the appearance of the metastable 4*H*(*a*) and 4*H*(*c*) polymorphs at ~650 °C, collectively represented as 4*H*(*x*). The 3*R* → 2*H*-$TaSe_2$ and 2*H* → 4*H*(*x*) transitions are newly observed transitions, represent new transitional pathways, and more clearly define the available polymorphic transitions to 1*T*-$TaSe_2$.

Introduction

Transition metal dichalcogenides, first studied in the 1940's and 50's, have received renewed scrutiny during the past decade.[1-2] Because these materials exhibit a wide range of electrical properties spanning semiconducting,[3-4] metallic,[5-6] and superconductive states,[7-9] and because they are easily nanostructured into low-dimensional forms, they are relevant to photodetector,[10-11] photoconversion,[12-13] and microelectronics applications.[10-11, 14] For example, the group 5 transition metal MX_2 materials (VS_2, $NbSe_2$, $TaSe_2$, and their alloys) are metallic conductors that also exhibit temperature-dependent superconductivity and charge density wave (CDW) phenomena.[15-18] The metallic conductivity arises from the M(IV) oxidation state which leaves a single conducting electron in the partially filled *d* bands of the metal centers.[19-20] These properties make group 5 transition metal MX_2 compositions suitable for electrochemical cells, logic circuits, and charge density wave-based devices.[5, 21-22]

Polymorphism is common for MX_2 materials, and with seven established phases [1*T*, 2*H*, 3*R*, 4*H*(*a*), 4*H*(*b*), 4*H*(*c*) and 6*R*], $TaSe_2$ exhibits an especially high degree of polymorphism.[23 24-26] The most well-studied phases are 2*H*-$TaSe_2$, the room-temperature-stable phase, and 1*T*-$TaSe_2$, a high-temperature phase that can be isolated by quenching from beyond ~850 °C.[24] The structure of 1*T*-$TaSe_2$ (Figure 3.1a) is characterized by tantalum in octahedral coordination geometry and only one formula unit per tetragonal unit cell, whereas the structure of 2*H*-$TaSe_2$ (Figure 3.1b) is characterized by tantalum in trigonal prismatic coordination geometry and two formula units per hexagonal unit cell.[23] In addition, these phases differ in their layer stacking sequences, with 2*H*-$TaSe_2$ having an *ABAB* arrangement and 1*T*-$TaSe_2$ having an *AA* arrangement.

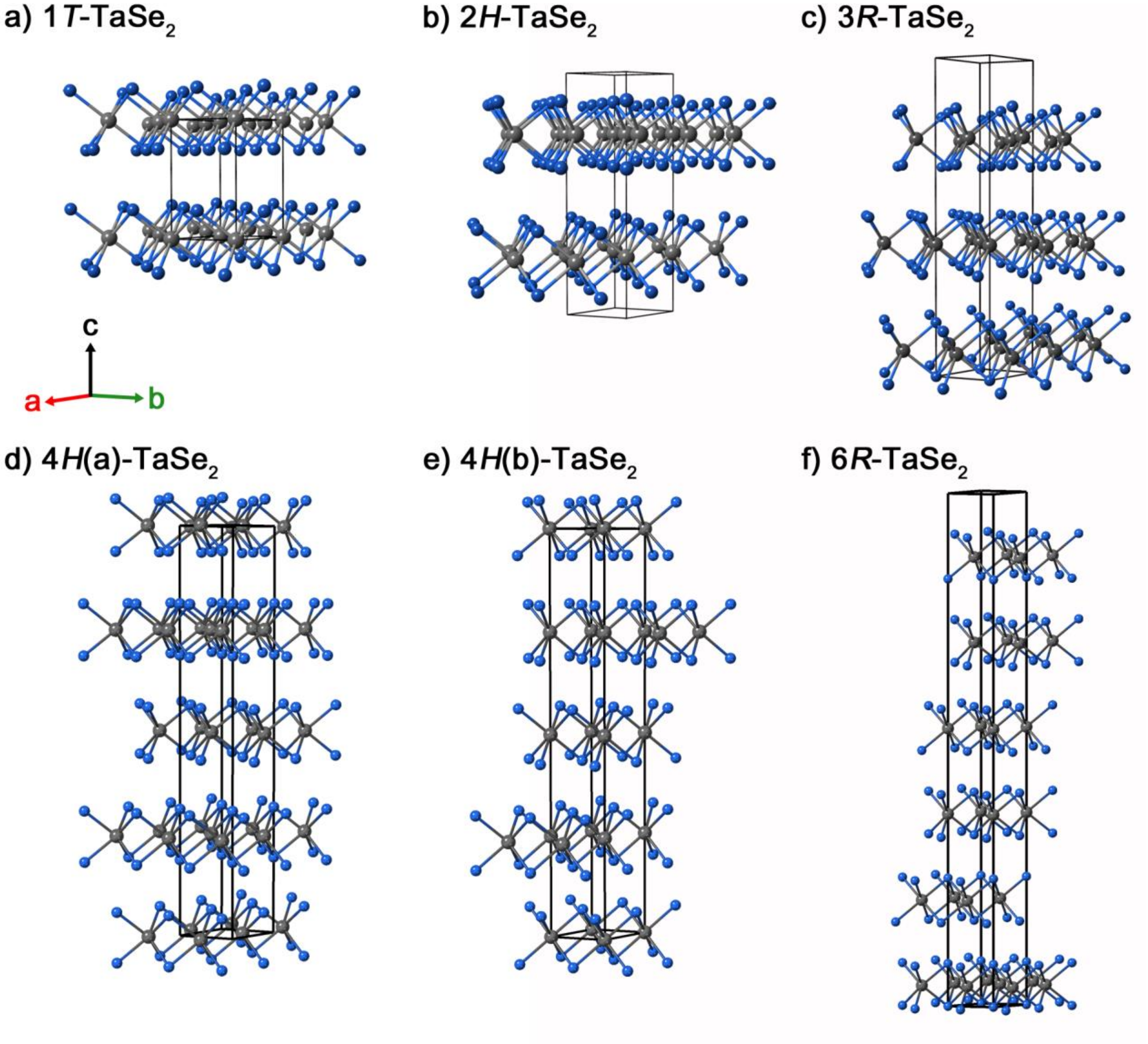

Figure 3.1 Perspective views of (a) 1*T*, (b) 2*H*, (c) 3*R*, (d) 4*H*(a), (e) 4*H*(b), and (f) 6*R*-TaSe$_2$; the Ta atoms shown in gray and the Se atoms in blue. The 2*H*, 3*R*, and 4*H*(a) polymorphs contain only a trigonal prismatic metal coordination, whereas the 1*T* polymorph contains only an octahedral coordination. 4*H*(b) and 6*R*-TaSe$_2$ contain alternating octahedral and trigonal prismatic coordination layers. A single unit cell is shown for each structure.

3*R*-TaSe$_2$ is a metastable phase that can be accessed from ~500 to ~800 °C.[24, 27] Like 2*H*-TaSe$_2$, 3*R*-TaSe$_2$ contains trigonal prismatic tantalum, yet its structure is characterized by three formula units per rhombohedral unit cell and layers stacking in an *AA´A´´* repeating order (Figure

3.1c). The three known 4*H* phases all contain four formula units per hexagonal unit cell and are differentiated by an (*a*), (*b*), or (*c*) nomenclature based on a modified Ramsdell notation. 4*H*(a)-$TaSe_2$ was first characterized by Kadijk, et al. in 1964.[27] This polymorph was discovered while mixed with other phases, 2*H* and 3*R*, when reactions were carried out between 600 and 900 °C.[25] 4*H*(*a*)-$TaSe_2$, containing only trigonal prismatic metal coordination layers in an *AA´BA´* stacking order (Figure 3.1d), is isostructural with 4*H*-$NbSe_2$.[28] Almost simultaneously in 1964, Brown and Beerntsen reported a second 4*H*-$TaSe_2$ polymorph containing alternating layers of octahedral and trigonal prismatic tantalum that result in an *ABA´B´* stacking order (Figure 3.1e).[29] The structure of this polymorph was later confirmed by Bjerkelund, et al., who isolated nearly phase-pure 4*H*(*b*)-$TaSe_2$ when quenching from 800 ℃.[26] Further study of 4*H*(*b*)-$TaSe_2$ led Huisman, et al. to find a third 4*H* phase, 4*H*(*c*)-$TaSe_2$. This phase contains only trigonal prismatic metal coordination but differs from 4*H*(*a*) in the layer stacking order: *AA´BA´* in 4*H*(*a*) vs. *ABB´A´* in 4*H*(*c*), which results in different space groups ($P\bar{6}m2$ vs. $P6_3mc$). Much like 4*H*(*b*)-$TaSe_2$, 6*R*-$TaSe_2$ contains alternating octahedral-trigonal prismatic tantalum layers (Figure 3.1f). This polymorph was first reported by Aslanov, et al. in 1962[30] and later confirmed by Kadijk, et al. in 1964.[27] The structure of 6*R*-$TaSe_2$ is characterized by six formula units per rhombohedral unit cell and an *ABA´B´A´´B´´* layer stacking order.

The different layer stacking orders and metal coordination geometries in the various polymorphs lead to variations in the electronic properties of $TaSe_2$. For example, a dramatic change in the CDW transition temperatures is observed in 2*H* vs. 1*T*-$TaSe_2$. In 1*T*-$TaSe_2$, two CDW transitions are observed significantly above room temperature at 473 and 600 K, whereas the same two CDW transitions in 2*H*-$TaSe_2$ occur at the significantly lower temperatures of 90 and 120 K.[23, 31] The electronic properties of 3*R*-$TaSe_2$ have received little attention, however, Cava

2015 studied the effects of Te doping in $TaSe_2$. Interestingly, they found that Te doping forced a polymorph change from 2*H* to 3*R* resulting in a superconductivity T_c of 2.4 K, the coexistence of CDWs and superconductivity, and a CDW transition near 100 K. Like the other polymorphs of $TaSe_2$, the Te-doped 3*R* variant was found to possess metallic conductivity.[32] 4*H*(*b*)-$TaSe_2$ has received some interest due to unique alternating layer structure. CDWs were observed in the octahedral layers, while simultaneous elastic coupling was observed in the trigonal prismatic layers.[33] This polymorph was also reported to be metallic above 600 K, the first of the two CDW transitions (410 and 600 K). A third CDW transition is observed at 75 K, although, it is believed that this transition originates in the trigonal prismatic layers.[34] Studies of the electronic properties of 4*H*(*a*), 4*H*(*c*), and 6*R*-$TaSe_2$ remain scarce, possibly due to the difficulty in synthetic accessibility.

Notably, the 1*T* phase is distinct from other $TaSe_2$ polymorphs in its color: gold rather than the silver/black of the 2*H* and 3*R* phases.[23] Color variations among polymorphs originating from electronic differences are known in other material systems, such as silicon carbide; for example, 6*H*-SiC is greenish whereas the 4*H*- and 15*R*-SiC are brown.[35,36] The role of electronic structure in the reflectivity of transition metal dichalcogenides, and the resulting implications, have not been explored, however.

In this chapter, the experimental exploration of the transitional behavior of 1*T*-$TaSe_2$ is discussed. Transitions were monitored by differential scanning calorimetry (DSC), non-ambient, powder x-ray diffraction (PXRD), and *ex situ* Raman spectroscopy experiments. We find that the gold to silver color change is associated with the 1*T* → 3*R*-$TaSe_2$ transition, which begins at ~310 °C. Shortly thereafter, the 3*R* → 2*H*-$TaSe_2$ transition occurs, followed by the appearance of 4*H*-$TaSe_2$ phases.

Experimental Methods

Synthesis of 1*T* and 3*R*-TaSe$_2$. Crystals of 1*T* and 3*R*-TaSe$_2$ were synthesized via a chemical vapor transport method using tantalum powder (STREM, 99.98%), and selenium powder (STREM, 99.99%) with iodine (J.T. Baker, 99.9%) at ~4 mg cm^{-3} as the transport agent. Ta and Se powders were ground together in a mortar and pestle before being placed into a quartz ampule (~18 mm x 1 mm) with iodine. The ampules were then evacuated and backfilled three times with Ar before sealing under vacuum. The filled ampules were then placed in a two-zone horizontal tube furnace. 1*T*-TaSe$_2$ crystals were grown at 975 °C with a ~100 °C gradient across the furnace for 336 h before quenching in salted ice water, whereas 3*R*-TaSe$_2$ crystals were grown at 750 °C with a ~100 °C gradient across the ampoule for 120 h and quenched in salted ice water.

***Ex situ* Heating of 1*T*-TaSe$_2$.** Several millimeter-sized 1*T*-TaSe$_2$ crystals were placed into a quartz ampule which was evacuated and backfilled 3 times with Ar before flame-sealing under vacuum (~20 mTorr). For optical microscopy, the sealed ampule was then heated to 100, 200, 300, 350 and 400 °C, held for 5 min, and then air quenched; the ampule was replaced in the furnace for heating to each successive temperature. For Raman spectroscopy, the ampules were heated at 370 or 450 °C, held for 5 min, then air quenched and opened to extract the crystals for analysis.

Characterization. Non-ambient, powder X-ray diffraction data were collected on a PANalytical Empyrean diffractometer with Cu-Kα radiation from 10 – 70° 2θ at a rate of 0.2 sec per step at 40 mA and 40 kV. The 1*T*-TaSe$_2$ crystals were mounted on a Si wafer in an Anton-Paar 1200 N Hot Stage furnace heated at 10 °/min from 25 to 900 °C; data was collected while holding at the specified temperatures. Scanning electron microscopy and energy dispersive spectroscopy data were obtained on a FEI Teneo FE-SEM operated between 5 and 20 keV. Differential scanning calorimetry was carried out in a Netzsch DSC 404 F1 Pegasus calorimeter from 25 – 1000 °C at

20 °C/min under an Ar flow of 50 mL/min. A Pt/Rh crucible with Al_2O_3 liner/Y_2O_3 coating was used to hold the sample during heating. *Ex situ* Raman spectroscopy data were acquired on a Renishaw InVia system at 50x magnification with 785 nm excitation $\leq$ 5 mW.

Results and Discussion

Evolution of Phases Starting From 1*T*-$TaSe_2$. In the experimental portion of this study, DSC was used to track the phase transformations of 1*T*-$TaSe_2$ from room temperature up to 1000 °C. A plot of the DSC data revealing several endothermic and a single exothermic transition can be seen in (Figure 3.2a), and we can compare these results to early work published by Bjerkelund and Kjekshus in 1967 and Huisman and Jellinek in 1969.[25-26]

Upon heating, 1*T*-$TaSe_2$ first undergoes a sudden, reversible, endothermic transition at approximately 190 °C. The onset temperature of this transition is comparable to the previously reported onset of the CDW transition from the commensurate to the incommensurate phases (200 °C) as established previously by Raman spectroscopy.[23, 37] PXRD at 190 and 225 °C (Figure 3.S1 and 3.S2) indicate shifts of ~1° 2θ in the peak positions, consistent with the small structural distortions related to the commensurate to incommensurate CDW transition. In their analysis of 1*T*-$TaSe_2$, Huisman and Jellinek also observed a transition at approximately 200 °C during a slow (10 °h^{-1}) heating experiment, however, an exothermic transition was reported being attributed to a 1*T* to 3*R* phase transition.[25] This transition is irreversible and exothermic, contrary to the endothermic peak observed here. Additionally, our powder diffraction pattern at 225 °C does not match to 3*R*-$TaSe_2$ but still matches 1*T*-$TaSe_2$ contrasting with the data reported by Huisman and Jellinek,[25] and Bjerkelund and Kjekshus.[26]

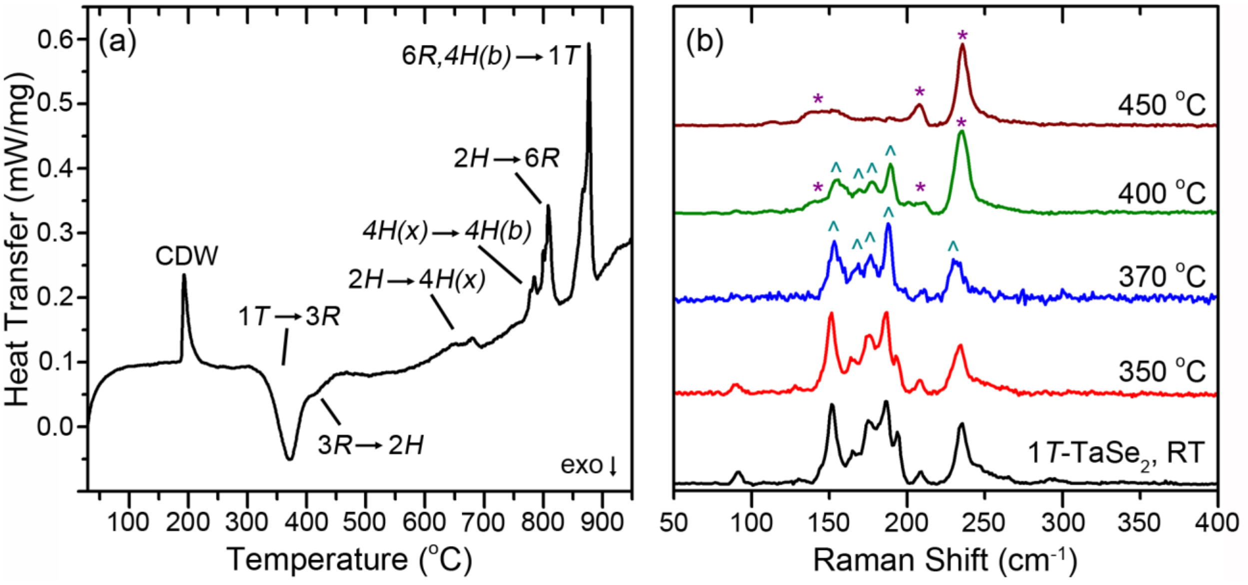

Figure 3.2 DSC and Raman plots of 1*T*-TaSe₂. The DSC plot (a) shows heating from room temperature to 950 °C under Ar. The thermic nature of each transition is indicated by the arrow in the lower right-hand corner: exothermic is down, endothermic is up. *Ex situ* Raman spectroscopy (b) shows the transition from 1*T*-TaSe₂ at room temperature to 3*R*-TaSe₂ (^) at 370 °C and then to 2*H*-TaSe₂ (*) at 450 °C.

As the temperature is increased, the next event appears as a large, exothermic peak with an onset of ~310 °C, consistent with an irreversible transition. Our PXRD at 310 °C shows a second polymorph alongside 1*T*-TaSe₂ indicating that a polymorph transformation is occurring (Figure 3.S2). The strong orientation effect, however, makes correct peak assignment to 2*H* or 3*R*-TaSe₂ difficult. *Ex situ* Raman spectroscopy aided the characterization of this transformation. After heating at 350 °C, the Raman spectrum of the TaSe₂ crystal shows small peak deviations at ~175 and 193 cm^{-1} compared with the spectrum of 1*T*-TaSe₂ at room temperature (Figure 3.2b), indicating the onset of a phase transition. A significant change is then observed at 370 °C with the loss of the peak at 193 cm^{-1}, a shift of the 235 cm^{-1} peak, and reduced intensity of the 175 cm^{-1} peak; these changes are consistent with the 1*T* → 3*R*-$TaSe_2$ phase change. An SEM image and a 3*R*-$TaSe_2$ Raman spectrum can be seen in Figure 3.3. A shoulder peak at ~400 °C is evident in the DSC plot, however, indicating a second transition in this temperature regime.

According to Bjerkelund and Kjekshus, the peak at 310 ℃ should correspond to the transition of 1*T*-$TaSe_2$ to the 3*R* polymorph, which was reported to occur between 300 and 500 ℃ with trace amounts of 2*H*-$TaSe_2$.[26] Although, Huisman and Jellinek reported this transition at 200 ℃, they also reported a 2*H*,3*R* mixture when slowly heating 6*R*-$TaSe_2$ to 225 °C showing that a mixture of these polymorphs can be achieved upon annealing a metastable phase.[25] Although the conditions are different in this study, our findings substantiate the transition reported by Bjerkelund and Kjekshus, and Huisman and Jellinek.[25-26]

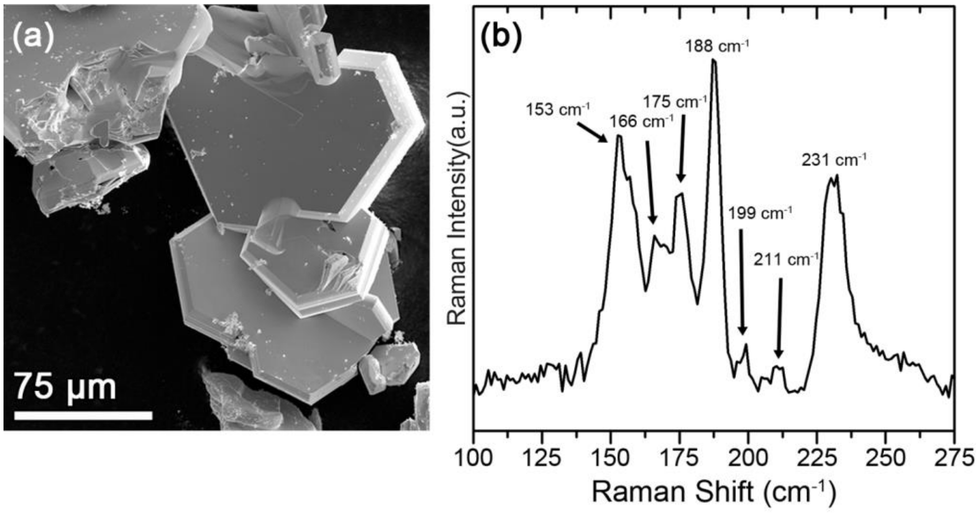

Figure 3.3 (a) SEM image and (b) Raman spectrum of 3*R*-$TaSe_2$ showing the characteristic peaks.

This transformation also is evident in the Raman spectra of 1*T*-$TaSe_2$ crystals heated at 400 °C. Between 140 and 220 cm^{-1}, new shoulder peaks are evident more closely matching the Raman spectrum of 2*H*-$TaSe_2$, implying that both the 3*R* and 2*H* phases are present. Also, the dominant peak at ~235 cm^{-1} becomes much stronger, and is accompanied by a shift down field, like that seen in 2*H*-$TaSe_2$. This transition is also visible in the DSC plot as a small shoulder at ~ 410 °C. With further heating to 450 °C, not only does the transition from 3*R* to 2*H*-$TaSe_2$ go to completion, but the transformation of 1*T*-$TaSe_2$ to the lower-temperature-stable phases is also complete.

The 3*R* → 2*H*-$TaSe_2$ transformation is in the temperature range used by Bjerkelund and Kjekshus to create 3*R*-$TaSe_2$, but has not been previously reported.[26] Further, Huisman and Jellinek state that 3*R*-$TaSe_2$ is the kinetic, and dominant, phase observed is in their heating experiments, yet is unstable at all temperatures.[25] Our observations support these statements with the appearance and disappearance of 3*R*-$TaSe_2$. The higher stability of the 2*H* phase is, most likely, the driving force for the latter phase transition with elevated temperature.

The polymorph transition from the 1*T* phase to a lower temperature stable phase is conveniently accompanied by a distinct color transition. To monitor the 1*T* → 3*R* transition, 1*T*-$TaSe_2$ crystals were placed in an evacuated, sealed quartz ampule, sequentially heated and held at increasing temperatures. This was followed by air-quenching from five different temperatures: 100, 200, 300, 350, and 400 °C. A gold → silver change in $TaSe_2$ with elevated temperature is indicative of the 1*T* → 3*R* transition. Optical microscopy images (Figure 3.4) were obtained at room temperature before heating in addition to after-holding for 5 minutes at each specified temperature to closely mirror the heating used in the DSC experiment.

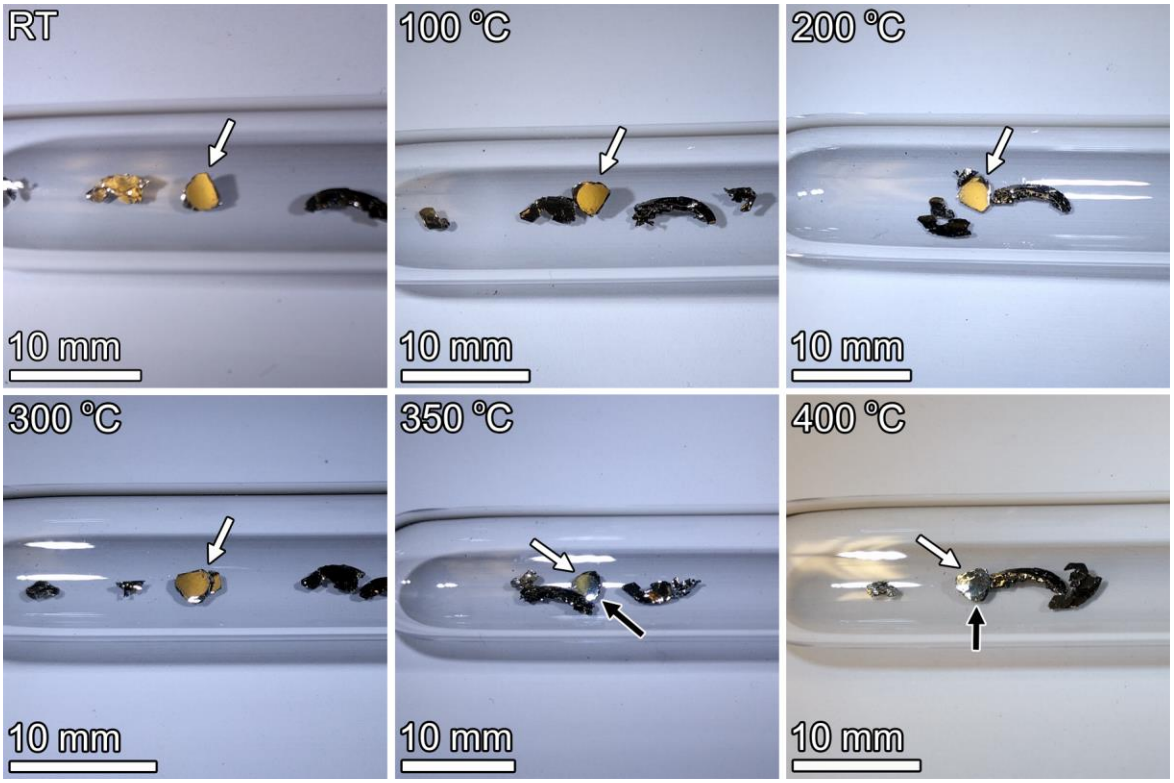

Figure 3.4 Optical microscopy images taken at RT of 1*T*-$TaSe_2$ crystals heated progressively at the indicated temperatures: unheated, 100 °C, 200°C, 300°C, 350 °C, and 400 °C. White arrows designate golden 1*T*-$TaSe_2$, while the black arrows indicate where transformation has occurred to silver 3*R*-$TaSe_2$.

At room temperature, the unheated 1*T*-$TaSe_2$ crystals are observed as the anticipated gold color.[23] This color remains unchanged after heating at 100, 200 and 300 °C, consistent with a lack of any polymorph transition. Indeed, no color change is to be expected in accordance with the DSC data (Figure 2a), where no polymorph change is observed until the large endotherm beginning at ~310 °C. Upon heating to 350 °C, the golden color appears significantly diminished, revealing a surface that is nearly 50% silver. A mix of colors on the surface shows that both polymorphs are present, i.e., the 1*T* → 3*R* transition of the flake is not yet complete. Additionally, the color change appears to start at the edges and progress towards the center of the $TaSe_2$ crystal, analogous to the oxidation of previously reported WSe_2 crystals.[38] After reaching 400 °C, little 1*T*-$TaSe_2$ remains on the crystal surface as evident by a surface that is ~90% silver, indicating a nearly complete transition from 1*T* to 3*R*. After experiment completion, the $TaSe_2$ flakes were allowed to sit overnight under in the unopened ampule. During this time, all flakes completely converted to the silver color of 2*H* and 3*R*-$TaSe_2$ indicating the completion of the irreversible transition. This transition is also reflected in Figure 2 with the 1*T* to 2*H*,3*R* transition reaching completion near 450 °C. $TaSe_2$ crystals heated at this temperature confirmed completion of the phase transition and were 100% silver 2*H*-$TaSe_2$ after heating (Figure S2).

Increasing the temperature to ~635 °C brings a small endothermic event which most likely results from a partial transformation of 2*H*-$TaSe_2$ to the 4*H*(*a*) and/or the 4*H*(*c*) polymorphs, a previously unreported transition. The formation of one or both 4*H*-$TaSe_2$ phases is further supported by the endothermic transition at 766 °C that is reported to belong to the 4*H*(*c*) → 4*H*(*b*) transition (770 °C).[25] Additionally, a small shoulder is observed on this peak which may in fact result from two transitions indicative of both the 4*H*(*a*) and 4*H*(*c*) to 4*H*(*b*)-$TaSe_2$ transitions. This transition could not be confirmed by PXRD, however, due to sample oxidation starting at 650 °C followed by complete at 680 °C. Oxygen outgassing is a known issue with the sample heating stage used in this study, which resulted in the observed sample oxidation.

Previous reports have shown that 4*H*(*a*) polymorph formation is a result of prolonged annealing above 800 °C followed by slow cooling back to room temperature.[25-26] This polymorph, however, was originally found alongside 2*H* and 3*R*-$TaSe_2$, demonstrating that polymorph coexistence is possible. On the other hand, 4*H*(*c*)-$TaSe_2$ was only obtained after heating the 4*H*(*b*) polymorph at 280 °C indicating that low temperature conversion to this phase is possible.[25]

Heating $TaSe_2$ beyond 770 °C brings another transition near 800 °C. This transition corresponds to the reversible $2H \rightarrow 6R$ phase transformation, a well-established transition.[24-25] The remaining endothermic peak begins near 850 °C and contains an obvious shoulder peak implying two concurrent transitions. The 847 °C onset temperature of this peak corresponds to the transformations of 6*R* (870 °C) and 4*H*(*b*)-$TaSe_2$ (880 °C) to the high temperature stable 1*T*-$TaSe_2$, respectively.[24-26] Due to the reversible nature of these transitions, retaining the 1*T* phase requires a quench from beyond 880 °C. To date, no higher temperature phases of $TaSe_2$ have been reported making 1*T*-$TaSe_2$ the predominant phase beyond 900 °C up to the yet undefined melting point.

Conclusions

The phase transitions in 1*T*-$TaSe_2$ were explored from room temperature up to 1000 °C. Differential scanning calorimetry revealed the commensurate to incommensurate CDW transition at ~190 °C, while DSC and *ex situ* Raman spectroscopy confirmed an initial transition from 1*T* to 3*R*-$TaSe_2$ at ~310 °C. This transition was then followed by the appearance of 2*H*-$TaSe_2$ at ~410 °C; Raman spectroscopy measurements showed the progress of the 3*R* to 2*H*-$TaSe_2$ transition between 350 and 450 °C. The 1*T* to 3*R* phase transition was also confirmed by optical microscopy as indicated by the observed gold to silver change in color. Additionally, a previously unreported transition from 2*H*-$TaSe_2$ to 4*H*(*x*)-$TaSe_2$, encompassing the 4*H*(*a*) and 4*H*(*c*) polymorphs, was observed at ~635 °C that is substantiated by the 4*H*(*x*) to 4*H*(*b*)-$TaSe_2$ transition observed at 766 °C.

Supplemental Information

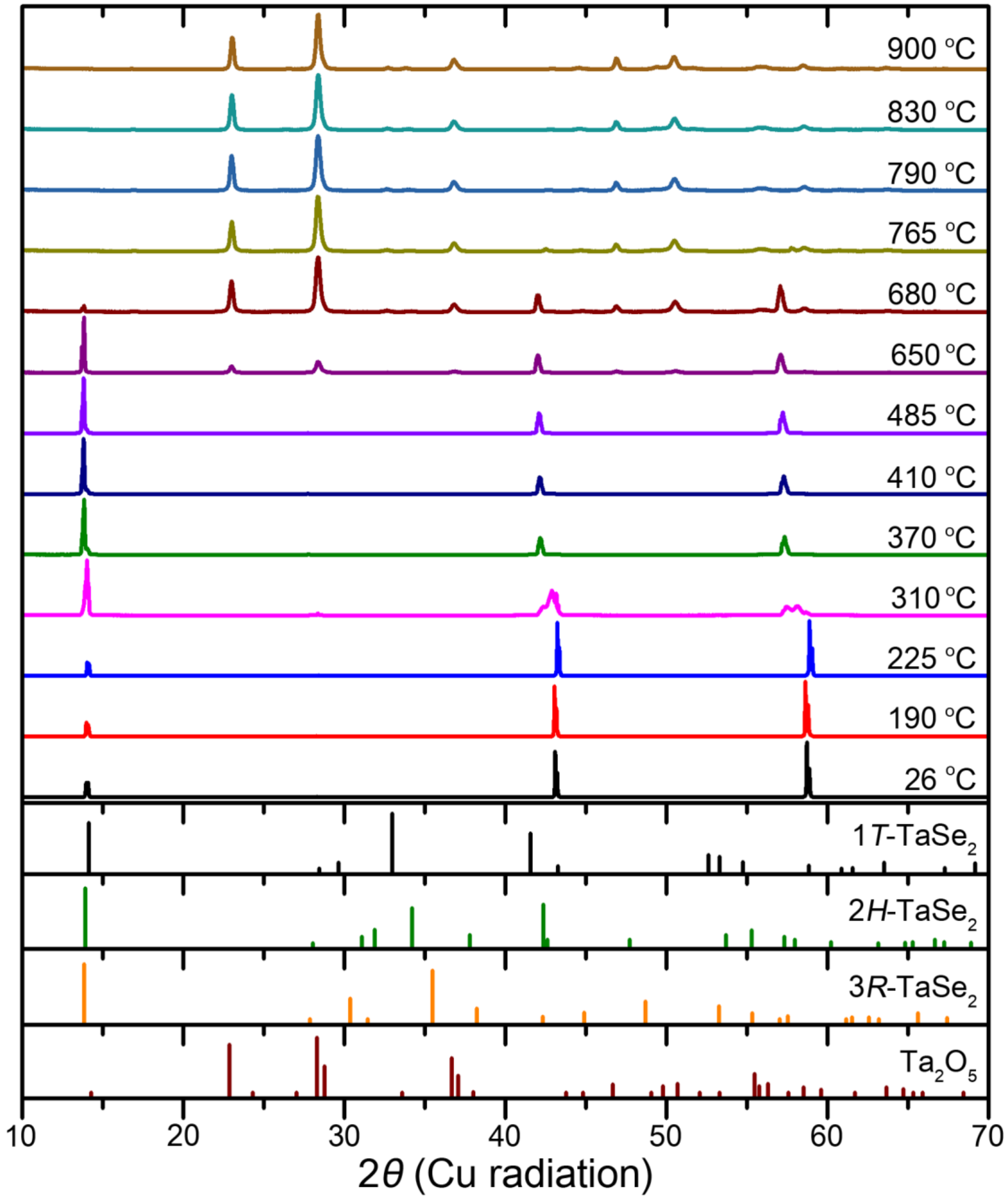

Figure 3.S1 Varied temperature XRD of 1*T*-$TaSe_2$ from room temperature up to 900 °C under N_2 flow. The droplines include the different phases present throughout the experiment including 1*T*-$TaSe_2$ (black, 01-073-1798), 2*H*-$TaSe_2$ (green, 04-008-0163), 3*R*-$TaSe_2$ (orange, 03-065-3657), and *o*-Ta_2O_5 (maroon, 04-013-9608). Some peaks at 310 °C also match to the Se-deficient phase $Ta_{1.11}Se_2$ (01-073-1804), but is completely diminished by 370 °C. Upon reaching 650 °C, a new phase emerges matching to *o*-Ta_2O_5.

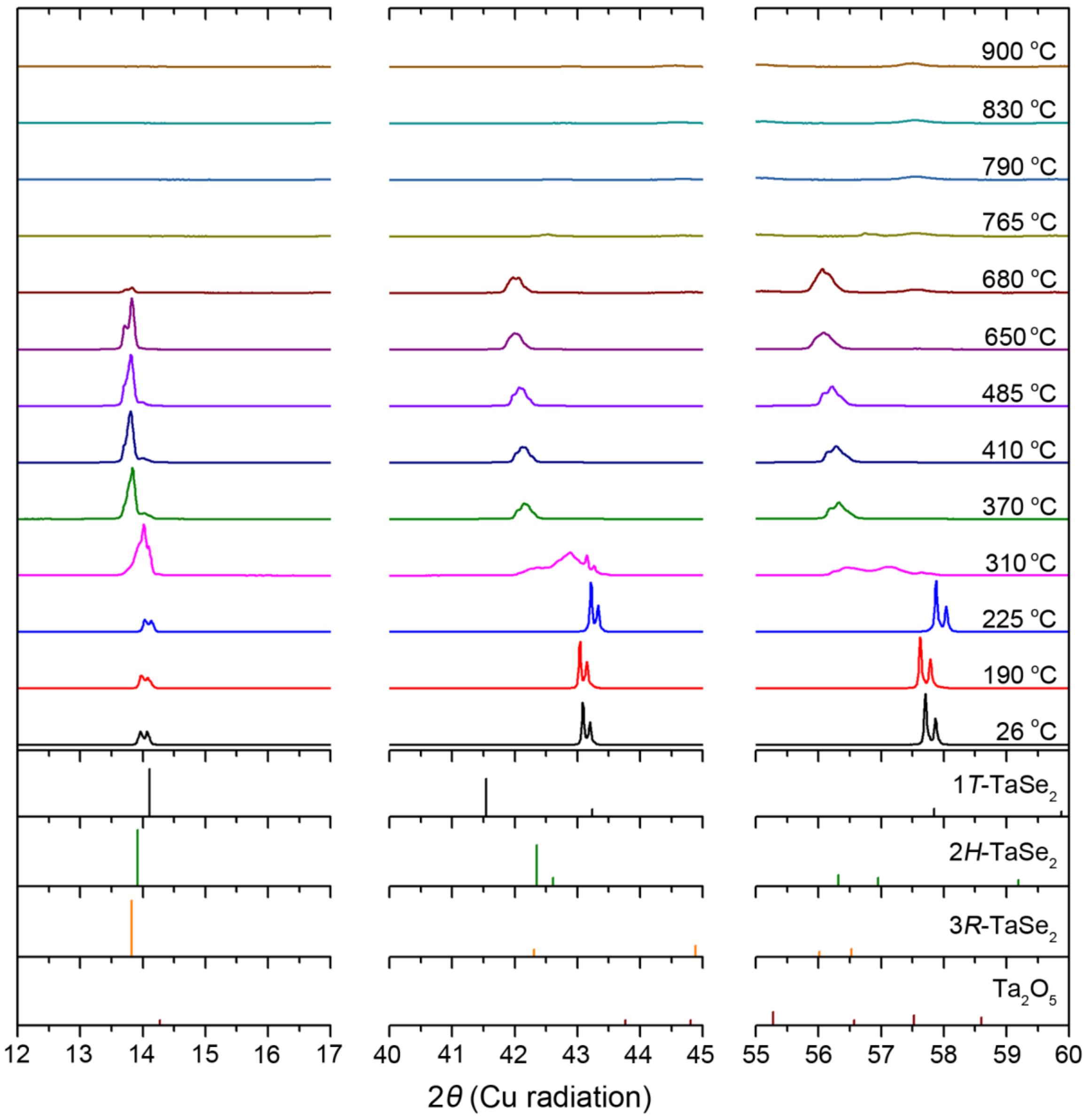

Figure 3.S2 Specific areas of the diffraction patterns revealing the pattern shifting. The two phases present at 310 °C include 1*T* and 3*R*-TaSe$_2$. Slight shifts in the TaSe$_2$ patterns can be assigned to thermal expansion of the unit cell with temperature. The larger shift at ~190 °C is attributed to the C to IC-CDW transition.

Figure 3.S3 Optical image of 1*T*-$TaSe_2$ after being heated at 450 °C. The golden color of 1*T*-$TaSe_2$ is replaced by the silver/black of 3*R*,2*H*-$TaSe_2$. At this temperature, $TaSe_2$ has proceeded through two phase transitions: 1*T* → 3*R*-$TaSe_2$ and then 3*R* → 2*H*-$TaSe_2$.

References

1. Ross, S.; Sussman, A., *J. Phys. Chem.* **1955,** *59* (9), 889-892.
2. Sorkin, V.; Pan, H.; Shi, H.; Quek, S. Y.; Zhang, Y. W., *CRC Cr. Rev. Sol. State* **2014,** *39* (5), 319-367.
3. Huang, Y. H.; Peng, C. C.; Chen, R. S.; Huang, Y. S.; Ho, C. H., *Appl. Phys. Lett.* **2014,** *105* (9), 093106.
4. Rasch, J.; Stemmler, T.; Manzke, R., *J. Alloy. Compd.* **2007,** *442* (1–2), 262-264.
5. Renteria, J.; Samnakay, R.; Jiang, C.; Pope, T. R.; Goli, P.; Yan, Z.; Wickramaratne, D.; Salguero, T. T.; Khitun, A. G.; Lake, R. K.; Balandin, A. A., *J. Appl. Phys.* **2014,** *115* (3), 034305.
6. Yu, Y.; Yang, F.; Lu, X. F.; Yan, Y. J.; ChoYong, H.; Ma, L.; Niu, X.; Kim, S.; Son, Y.-W.; Feng, D.; Li, S.; Cheong, S.-W.; Chen, X. H.; Zhang, Y., *Nat. Nano* **2015,** *10* (3), 270-276.
7. Sipos, B.; Kusmartseva, A. F.; Akrap, A.; Berger, H.; Forro, L.; Tutis, E., *Nat. Mater.* **2008,** *7* (12), 960-965.

8. Tsen, A. W.; Hovden, R.; Wang, D.; Kim, Y. D.; Okamoto, J.; Spoth, K. A.; Liu, Y.; Lu, W.; Sun, Y.; Hone, J. C.; Kourkoutis, L. F.; Kim, P.; Pasupathy, A. N., *P. Natl. Acad. Sci. USA* **2015,** *112* (49), 15054-15059.

9. Costanzo, D.; Jo, S.; Berger, H.; Morpurgo, A. F., *Nat. Nano* **2016,** *11* (4), 339-344.

10. Li, Z.; Yang, S.; Dhall, R.; Kosmowska, E.; Shi, H.; Chatzakis, I.; Cronin, S. B., *ACS Nano* **2016,** *10* (7), 6836-6842.

11. Lopez-Sanchez, O.; Lembke, D.; Kayci, M.; Radenovic, A.; Kis, A., *Nat. Nano* **2013,** *8* (7), 497-501.

12. Li, H.; Lu, G.; Wang, Y.; Yin, Z.; Cong, C.; He, Q.; Wang, L.; Ding, F.; Yu, T.; Zhang, H., *Small* **2013,** *9* (11), 1974-1981.

13. Lewerenz, H. J.; Heller, A.; DiSalvo, F. J., *J. Am. Chem. Soc.* **1980,** *102* (6), 1877-1880.

14. Yamamoto, M.; Dutta, S.; Aikawa, S.; Nakaharai, S.; Wakabayashi, K.; Fuhrer, M. S.; Ueno, K.; Tsukagoshi, K., *Nano Lett.* **2015,** *15* (3), 2067-2073.

15. Chatterjee, U.; Zhao, J.; Iavarone, M.; Di Capua, R.; Castellan, J. P.; Karapetrov, G.; Malliakas, C. D.; Kanatzidis, M. G.; Claus, H.; Ruff, J. P. C.; Weber, F.; van Wezel, J.; Campuzano, J. C.; Osborn, R.; Randeria, M.; Trivedi, N.; Norman, M. R.; Rosenkranz, S., *Nat. Commun.* **2015,** *6*, 6313.

16. Beal, A. R.; Hughes, H. P.; Liang, W. Y., *J. Phys. C Solid State* **1975,** *8* (24), 4236.

17. Sun, X.; Yao, T.; Hu, Z.; Guo, Y.; Liu, Q.; Wei, S.; Wu, C., *Phys. Chem. Chem. Phys.* **2015,** *17* (20), 13333-13339.

18. Yuan, J.; Wu, J.; Hardy, W. J.; Loya, P.; Lou, M.; Yang, Y.; Najmaei, S.; Jiang, M.; Qin, F.; Keyshar, K.; Ji, H.; Gao, W.; Bao, J.; Kono, J.; Natelson, D.; Ajayan, P. M.; Lou, J., *Adv. Mater.* **2015,** *27* (37), 5605-5609.

19. Chhowalla, M.; Shin, H. S.; Eda, G.; Li, L.-J.; Loh, K. P.; Zhang, H., *Nat. Chem.* **2013,** *5* (4), 263-275.

20. Kratochvilova, M.; Hillier, A. D.; Wildes, A. R.; Wang, L.; Cheong, S.-W.; Park, J.-G., *NPJ Quant. Mater.* **2017,** *2* (1), 42.

21. Hitz, E.; Wan, J.; Patel, A.; Xu, Y.; Meshi, L.; Dai, J.; Chen, Y.; Lu, A.; Davydov, A. V.; Hu, L., *ACS Appl. Mater. Inter.* **2016,** *8* (18), 11390-11395.

22. Liu, G.; Debnath, B.; Pope, T. R.; Salguero, T. T.; Lake, R. K.; Balandin, A. A., *Nat. Nano* **2016,** *11* (10), 845-850.

23. Samnakay, R.; Wickramaratne, D.; Pope, T. R.; Lake, R. K.; Salguero, T. T.; Balandin, A. A., *Nano Lett.* **2015,** *15* (5), 2965-2973.

24. Lieth, R. M. A.; Terhell, J. C. J. M., Transition Metal Dichalcogenides. In *Preparation and Crystal Growth of Materials with Layered Structures*, Lieth, R. M. A., Ed. Springer Netherlands: Dordrecht, 1977; pp 141-223.

25. Huisman, R.; Jellinek, F., *J. Less-Common Met.* **1969,** *17* (1), 111-117.

26. Bjerkelund, E.; Kjekshus, A., *Acta Chem. Scand.* **1967,** *21* (2).

27. Kadijk, F.; Huisman, R.; Jellinek, F., *Recl. Trav. Chim. Pay-B* **1964,** *83* (7), 768-775.

28. Revolinsky, E.; Brown, B. E.; Beerntsen, D. J.; Armitage, C. H., *J. Less-Common Met.* **1965,** *8* (1), 63-72.

29. Brown, B. E.; Beerntsen, D. J., *Acta Crystallogr.* **1965,** *18* (1), 31-36.

30. Aslanov, L. A.; Ukrainskii, Y. M.; Simanov, A. V., *Zh. Neorg. Khim.+* **1963,** *8* (8), 5.

31. Yan, J.-A.; Cruz, M. A. D.; Cook, B.; Varga, K., *Sci. Rep. UK* **2015,** *5*, 16646.

32. Luo, H.; Xie, W.; Tao, J.; Inoue, H.; Gyenis, A.; Krizan, J. W.; Yazdani, A.; Zhu, Y.; Cava, R. J., *P. Natl. Acad. Sci. USA* **2015,** *112* (11), E1174-E1180.

33. Lüdecke, J.; van Smaalen, S.; Spijkerman, A.; de Boer, J. L.; Wiegers, G. A., *Phys. Rev. B* **1999,** *59* (9), 6063-6071.

34. Olaoye, O.; Erasmus, N.; Haupt, K.; Schwoerer, H., *J. Phys. B-At. Mol. Opt.* **2016,** *49* (6), 064011.

35. Lambrecht, W. R. L.; Limpijumnong, S.; Rashkeev, S. N.; Segall, B., *Mater. Sci. Forum* **2000,** *338-342*, 6.

36. Lebedev, A. A., *Semicond. Sci. Tech.* **2006,** *21* (6), 18.

37. Tsang, J. C.; Smith, J. E.; Shafer, M. W.; Meyer, S. F., *Phys. Rev. B* **1977,** *16* (10), 4239-4245.

38. Liu, Y.; Tan, C.; Chou, H.; Nayak, A.; Wu, D.; Ghosh, R.; Chang, H.-Y.; Hao, Y.; Wang, X.; Kim, J.-S.; Piner, R.; Ruoff, R. S.; Akinwande, D.; Lai, K., *Nano Lett.* **2015,** *15* (8), 4979-4984.

CHAPTER 4

MONOCLINIC STRUCTURES OF NIOBIUM TRISULFIDE

Matthew A. Bloodgood, Pingrong Wei, Ece Aytan, Krassimir N. Bozhilov, Alexander A. Balandin, and Tina T. Salguero, *APL Materials*. 2018, *6*, 026602. Reprinted here with permission of AIP Publishing.

Abstract

Two new polymorphs of niobium trisulfide are established by single crystal x-ray diffraction. NbS_3-IV crystallizes in the monoclinic space group $P2_1/c$ with lattice parameters a = 6.7515(5) Å, b = 4.9736(4) Å, c = 18.1315(13) Å, β = 90.116(2)°. Its structure is based on chains of [NbS_6] trigonal prisms containing Nb–Nb pairs with a bond length of 3.0448(8) Å; this pairing causes the chains to corrugate slightly along their axis, a feature also present in triclinic NbS_3-I that leads to semiconductor properties. The stacking arrangement of chains is different in these polymorphs, however, with NbS_3-I having an ABCDE repeating sequence of chain bilayers and NbS_3-IV having an AB repeating sequence. HRTEM studies show the presence of topotactically-oriented intergrown zones and numerous dislocations, which result in mosaic structuring. A second new polymorph, NbS_3-V, crystallizes in the monoclinic space group $P2_1/m$ with lattice parameters a = 4.950(5) Å, b = 3.358(4) Å, c = 9.079(10) Å, β = 97.35(2)°. In contrast to NbS_3-IV, NbS_3-V maintains fixed a Nb–Nb bond distance of 3.358(4) Å along the chains, and it has an ABCDE repeating sequence of chain bilayers similar to NbS_3-I. HR-STEM imaging of an exfoliated NbS_3-V nanoribbon shows the continuous [NbS_6] chains oriented along the b-axis. These results provide the first firmly-established structural data for monoclinic NbS_3. In addition, SEM images show the formation of NbS_3 rings and cylinders, and a combination of powder x-ray diffraction and Raman spectroscopy provides a way to distinguish between NbS_3 polymorphs.

Letter

Many classes of materials have been proposed as replacements for semiconductor-based electronics technology as it progresses in complexity and miniaturization.[1] Transition metal chalcogenides are leading candidates in the current "beyond-graphene" milieu.[2] Metal dichalcogenide (MX_2) and trichalcogenide (MX_3) compositions, together with their polymorphs and alloys, provide a diverse set of materials exhibiting low dimensionality,[3-5] wide ranging electrical properties,[6,7-9] and reasonable processing options.[10-11] In recent work, we and others have investigated nanostructured MX_3 materials for electronic device applications.[6-7, 9, 12-13] The unique properties of these materials result from their dual low-dimensional nature, i.e., quasi-one-dimensional and two-dimensional (Q1D-2D). Their primary structural unit is [MX_6] trigonal prisms, which are fused end-to-end into continuous chains; this motif leads to quasi-one-dimensional electronic character as well as distinct anisotropy. Additional metal-chalcogenide interactions between neighboring chains result in bilayer sheets that can be flat (e.g., $ZrSe_3$) or corrugated (e.g., $TaSe_3$). These two-dimensional sheets, stacked and held together by van der Waals bonding, then make up the three-dimensional structure. Depending on the composition, structure, and morphology of any particular MX_3 sample, either one- or two-dimensional character may dominate. Much like MX_2 materials, MX_3 materials are amenable to mechanical or chemical exfoliation along the van der Waals gap,[6, 14] and recent studies show that their properties can be maintained or even enhanced by nanostructuring.[12, 15]

Here we consider NbS_3, arguably the least-well-understand metal trichalcogenide. The niobium–sulfur system contains a rich cornucopia of phases, including an unknown number of NbS_3 polymorphs, varying compositions from NbS to $Nb_{21}S_8$, and the possibility of non-stoichiometric phases.[16-19] Offsetting this complexity and piquing our interest are intriguing reports about the electrical and charge density wave (CDW) properties of certain NbS_3 samples, including multiple CDW transitions and room temperature charge transport.[3,20,21] However, further progress has been impeded by the absence of well-established structural information, spectroscopic characterization, or even reproducible synthetic details. Therefore, in this contribution we aim to clarify the polymorphism of NbS_3 as part of the foundation required to understand its electronic properties.

To date, NbS_3 has been reported to crystallize in four forms: types I, II, and III, as well as a high-pressure phase (Table 1). Jellinek and coworkers first proposed a monoclinic $ZrSe_3$-type NbS_3 structure in 1960.[16] They reported a definitive structure in 1978, using single crystal x-ray diffraction data to refine the NbS_3 structure with a triclinic unit cell (notably having $\alpha = \gamma = 90°$).[22] This polymorph is known as NbS_3-I in the literature. Compared to other MX_3 structures, NbS_3-I has several unique features. The most remarkable is Nb–Nb pairing along the NbS_3 chain axis that manifests as alternating Nb–Nb bonds (~3.0 Å) and gaps (~3.7 Å). This linear Peierls distortion at room temperature causes NbS_3-I to be semiconducting, with an experimentally determined band gap in the range of 0.66 to 1 eV (based on transport, optical transmittance, and photoconduction measurements), rather than metallic.[23-27] Another consequence is the doubling of the *b*-axis (6.730 Å) compared to other MX_3 structures (typically ~3.3 Å), which is needed to accommodate Nb–Nb pairs in the unit cell (Fig. 4.1). A recent report by Fedorov and coworkers demonstrated the solution-based exfoliation of NbS_3-I into nanoribbons.[11]

Table 4.1 Unit cell and synthesis parameters for previously reported NbS_3 polymorphs as well as new polymorphs NbS_3-IV and NbS_3-V.

Polymorph	**Synthesis Conditions**	**Space Group**	**Unit Cell Parameters**		Z	**Nb···Nb (Å)**	**Ref.**
			a, b, c, **(Å)**	α, β, γ **(deg)**			
NbS_3-I	NbS_2Cl_2; 588 → 569 °C, 48 h; slow cool	$P\bar{1}$	4.963 6.730 9.144	90 97.17 90	4	3.045 3.702	[22]
NbS_3-HP	Nb + S; 700 °C at 2 GPa, 0.5 h	$P2_1/m$	9.68 3.37 14.83	90 109.9 90	6	3.370	[29]
NbS_3-II (proposed)	Nb + S; 600 → 580 °C, 15 d	$P2_1/m$	9.9 3.4 18.3	90 97 90	…	…	[26, 27]
NbS_3-II (proposed)	Nb + S; 500 °C	…	9.1–9.6 18.7–19.9 3.4	90 97–98 90	8	…	[25]
NbS_3-III (proposed)	NbS_2 + S; 550 °C, 21 days, 400 °C 48 h, air quench	…	~5 … ~9	90 98–99 90	…	…	[20]
NbS_3-IV	Nb + S, I_2 transport; 670 → 570 °C, 10 days	$P2_1/c$	6.7515(5) 4.9736(4) 18.1315(13)	90 90.116(2) 90	4 (8)	3.0448(8) 3.7087(8)	This work
NbS_3-V	Nb + S, 10% S transport; 700 → 670 °C, 10 days	$P2_1/m$	4.950(5) 3.358(4) 9.079(10)	90 97.35(2) 90	2	3.358(4)	This work

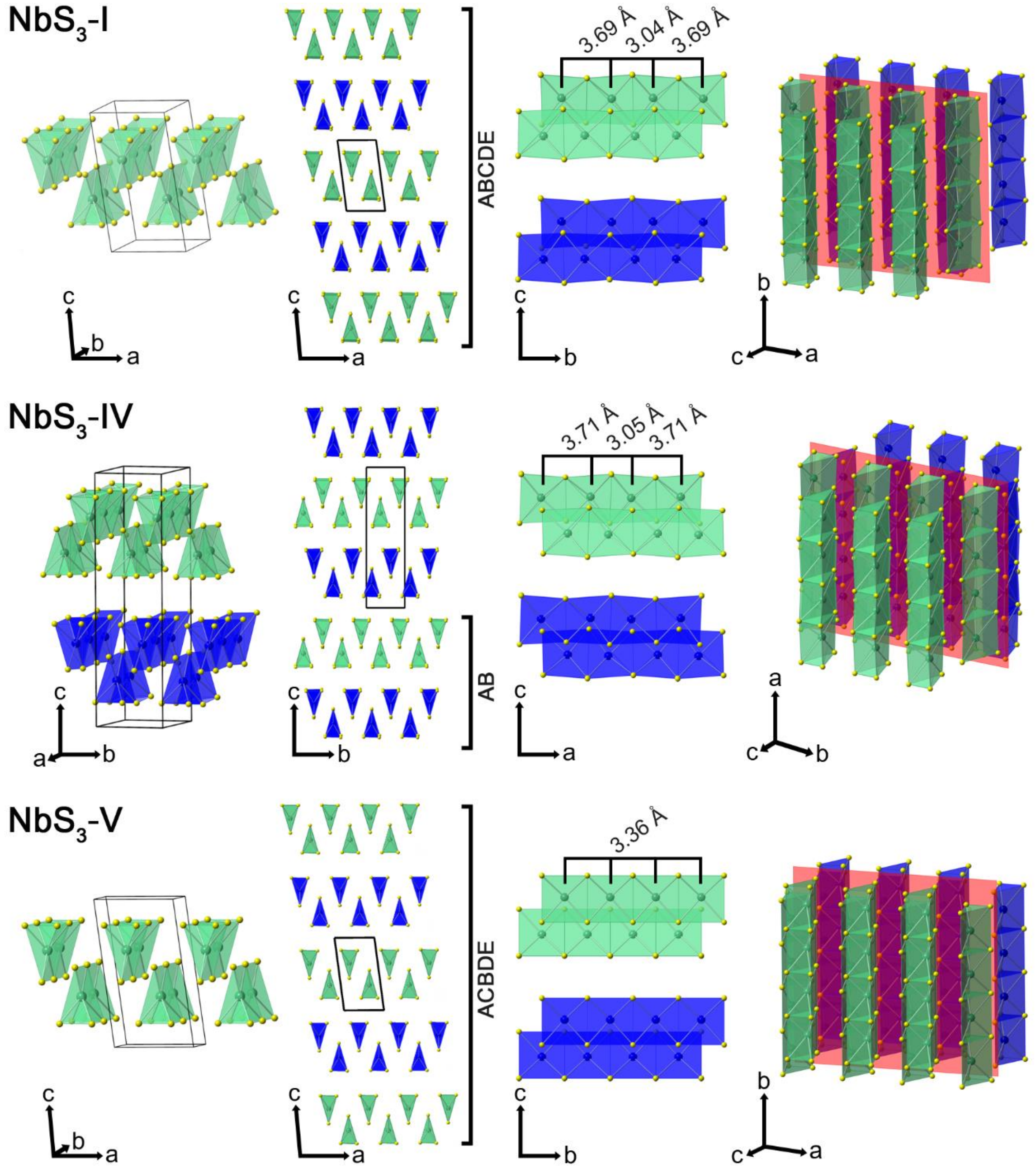

Figure 4.1 Views of NbS_3-I, IV, and V: from left to right including unit cell, chain cross section, layer, and perspective views. The NbS_3 bilayers are differentiated by color to illustrate the van der Waals gaps, which is further illustrated with a red plane in each perspective view. The structures of these three polymorphs have been established by single crystal x-ray diffraction.

A second polymorph, NbS_3-II, was identified in 1978 based on electron diffraction studies, which showed inter-row pairs of satellite diffraction lines that resolved into rows of spots with varying temperature.[28] These rows occurred at irrational positions with similar separations as NbS_3-I, leading to the proposal that NbS_3-II was a superstructure of NbS_3-I with different chain stacking. Several years later, Prodan and coworkers introduced a model monoclinic NbS_3-II unit cell with lattice parameters $2a'$, $b'/2$, $2c'$, β' based on the NbS_3-I unit cell (lattice parameters a, b, c, β) (Table 1).[29,30] In parallel, Roucau and coworkers proposed a closely related model monoclinic NbS_3-II unit cell with lattice parameters $2a''$, $2c''$, $b''/2$, β'' based on a different multiple of the NbS_3-I unit cell (Table 4.1).[26, 31-32] In the almost forty years since NbS_3-II was identified, however, its atomic structure has remained unsolved. During this time, continued interest in this polymorph has been motivated by its three CDWs: a low temperature transition at 150 K, a second transition at 330-370 K, and a high temperature transition at 620-650 K.[21, 26] The transition at 330-370 K, just above room temperature, is an unusual one for CDW transport, and according to Zybtsev and coworkers, this CDW exhibits high transport velocities and sliding coherence.[21]

A high-pressure modification of NbS_3 prepared at 700 °C with 2 GPa pressure was reported by Kikkawa and coworkers in 1982.[33] The monoclinic unit cell deduced from powder x-ray diffraction data is similar to that of monoclinic $NbSe_3$ (Table 4.1), but atomic positions for NbS_3-HP could not be determined.[33] Yet another polymorph, designated NbS_3-III, was reported by Zettl and coworkers in 1982. In this case, powder x-ray diffraction data provided only partial lattice parameters. However, NbS_3-III can be distinguished by a characteristic CDW transition at 155 K.[20] Subsequent electrical measurements by Zybtsev and coworkers on "low-ohmic" and "high-ohmic" NbS_3 samples showed that low-ohmic NbS_3 exhibits CDW transitions at both 150 and 360 K whereas high-ohmic NbS_3 exhibits a single CDW transition at 150 K.[3] On this basis, it has been postulated that low-ohmic and high-ohmic NbS_3 correspond to NbS_3-II and NbS_3-III, respectively; an alternate interpretation is that low- and high-ohmic NbS_3 as well as NbS_3-III are sub-phases of NbS_3-II.[21]

This letter reports the growth and characterization of two new monoclinic polymorphs of NbS_3, designated NbS_3-IV and NbS_3-V following the nomenclature currently in place. Interestingly, we isolated NbS_3-IV under synthetic conditions previously reported to produce NbS_3-I and NbS_3-V under synthetic conditions previously reported to produce NbS_3-II.[3, 34] Single crystal x-ray diffraction studies of both NbS_3-IV and NbS_3-V provide unambiguous structural information about these polymorphs. Such definitive characterization is necessary for accurate identification, especially because NbS_3 polymorphs form under similar conditions and often more than one can be found in the same crystal growth batch.[28] Furthermore, electron microscopy analysis provides information about structural defects in NbS_3-IV and atomic order in NbS_3-V, and Raman spectroscopy of NbS_3-IV and NbS_3-V provides data that can be used to distinguish between polymorphs.

Niobium trisulfide samples were synthesized using niobium powder (99.99%, STREM) and sublimed sulfur powder (Baker, >99%) using a chemical vapor transport method. Iodine (Baker, 98%) at 4 – 6 mg/cm^3 was used for the growth of the NbS_3-IV phase, whereas excess sulfur (~10%) was utilized as the transport agent for the growth of NbS_3-V crystals. For all syntheses, niobium and sulfur were lightly ground by mortar and pestle before being placed in a quartz ampule (~13 cm^3). The ampules were then evacuated and backfilled with argon three times before flame sealing under vacuum (~10^{-2} Torr). Reactions were placed in a two-zone furnace with a fixed gradient for 10 – 14 days; upon completion, the ampule/furnace was allowed to cool to room temperature naturally.

NbS_3-IV crystals used for x-ray diffraction analysis were prepared at 670 °C with a 100 °C gradient (670 °C source zone → 570 °C growth zone). This synthesis temperature is comparable to temperatures used to prepare NbS_3-I,[11, 27, 34] and the only difference here is the use of I_2 as a transport agent. This NbS_3 polymorph crystallizes in a monoclinic unit cell, and the structure was solved using space group $P2_1/c$. Additional details are provided in Tables 4.S1 and 4.S2, and crystallographic data have been deposited with the Cambridge Crystallographic Data Centre (structure number 1574381).

The unit cell of NbS_3-IV is larger than that of NbS_3-I because the *c*-axis is doubled, resulting in twice as many chains per unit cell (Fig. 4.1). The asymmetric unit of NbS_3-IV is Nb_2S_6, making Z formally 4, which becomes 8 when normalized to the formula NbS_3. Also, in contrast to other MX_3 structures, the chain axis in NbS_3-IV is the *a*- rather than the *b*-axis (Fig. 4.1). Looking down the *a*-axis, the structure of NbS_3-IV in cross section is similar to the model $ZrSe_3$-type structure, specifically the "A-variant".[35] However, a difference between these structures is their layer-stacking order. This is clearly seen when examining multiple unit cells of each polymorph (Fig. 4.1). The chains in NbS_3-I realign every five bilayers, where a bilayer is defined as a pair of chains bounded by van der Waals gaps (Fig. 4.1 where pairs of blue or green chains designate the bilayers). Thus, the repeat sequence is ABCDE. However, NbS_3-IV experiences a realignment of the chain after only two bilayers, making the repeat sequence AB.

In the chain cross-section, three sulfur atoms surround a niobium atom to form acute, isosceles triangles. The bases of the triangles are made of a 2.015 Å S–S bond; the presence of this bond is consistent with the formulation of NbS_3 as $Nb(S_2)S$.[22] The sides of the triangles are separated by longer $S\cdots S$ distances of 3.404-3.418 Å in one chain type and 3.787-3.828 Å in another chain type. Two interchain Nb–S bonds of 2.623 and 2.654 Å exist between each chain, which hold the bilayer together. Each bilayer is separated from the next by a distance of ~2.8 Å, the van der Waals gap.

Looking down the *b*-axis (Fig. 4.1), we see that NbS_3-IV contains Nb–Nb pairing with a bond distance of 3.0448 Å, much like NbS_3-I. Thus NbS_3-IV demonstrates that it is possible to have Nb–Nb pairing within a space group with $P2_1/m$ symmetry, i.e., it is not essential to reduce the symmetry to triclinic as in NbS_3-I. It is curious that Jellinek and coworkers published two papers prior to their report of NbS_3-I's triclinic structure in which they reported monoclinic unit cells extremely similar to what we have found for NbS_3-IV.[16-17] It is possible that they actually made NbS_3-IV in earlier work, which was based on the synthesis of NbS_3 from the elements, whereas their structural study was conducted on NbS_3 crystals generated through the thermal decomposition of NbS_2Cl_2.[22] The differences in preparative conditions may have led to the formation of NbS_3-I *versus* NbS_3-IV. In addition, van Smaalen has re-interpreted the triclinic space group $P\bar{1}$ of NbS_3-I as a monoclinic superspace group, proposing that this is an uncommon example of a modulated structure.[36]

The relatively high *wR* value (11.38%) associated with the refinement of NbS_3-IV reflects the presence of structural disorder, possibly including sulfur vacancies, faulting or slippage along the van der Waals planes, and twinning, all of which have been observed in various MX_3 materials.[28, 35, 37] To identify the specific disorder in NbS_3-IV, TEM analysis was performed on a Thermo Fisher Scientific Themis 300 instrument, fitted with X-FEG electron gun and CETA 4Kx4K CMOS camera, at an accelerating voltage of 300 kV. Specimens were prepared by dispersing a small amount of as-synthesized NbS_3-IV powder in distilled water without grinding, and depositing a droplet of the resulting suspension onto lacey carbon grids. The TEM study revealed that the sample consists of three types of particles: (1) long thin whiskers with aspect ratios >100 and thicknesses <100 nm that are elongated parallel to the *a*-axis [Fig. 4.2(a)]; (2) prismatic crystals with aspect ratios <20, with a long side parallel to the *a*-axis, a short side parallel to the *b*-axis, and thicknesses <100 nm along the *c*-axis [Fig. 4.2(b)]; (3) small aggregates consisting of isometric particles <50 nm in diameter.

The fibers of NbS_3-IV are twisted around their long axis, resulting in the development of numerous dislocations that can be identified through disruptions of the lattice fringes parallel to {001} [Fig. 4.2(a)]. The prismatic particles consist of topotactically-intergrown zones 5 to 50 nm wide parallel to the *b*-axis and several microns long parallel to the *a*-axis [Fig. 4.2(b)]. They are coherently intergrown with interfaces parallel to the {010} planes. The individual crystals exhibit

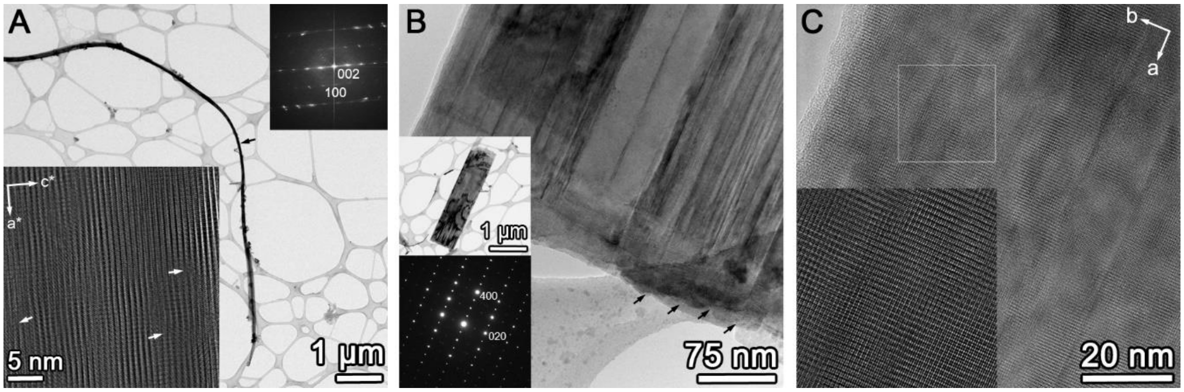

Figure 4.2 (a) Bright field TEM image of a NbS_3-IV fiber. Insets show (i) HRTEM image (lower left) of the crystal along the *b*-axis and (ii) the corresponding indexed FFT pattern (upper right). The location of the HRTEM image is indicated by a black arrow. In the HRTEM inset, multiple disruptions of the lattice fringes parallel to {001} are visible; some dislocations are indicated by white arrows. (b) Bright field high magnification TEM image of a prismatic NbS_3-IV particle. Insets shown are (i) low magnification BF TEM image of the whole particle (upper) and (ii) the corresponding selected area electron diffraction pattern along the c-axis, which confirms the single crystal nature of the whole particle. The topotactically-oriented individual intergrown zones are clearly visualized, with some of the coherent interfaces between zones indicated by black arrows. (c) HRTEM image of the particle in (b). Inset shows a magnified view of the area marked by a white box. The complex lattice contrast and the mosaic structure of low-angle domains is revealed here; the slight tilt of the domains causes considerable change in the lattice fringe contrast, which prevents the reliable interpretation of any stacking disorder that might be present parallel to the *c*-axis.

mosaic structure with fine domains about 10 nm in diameter [Fig. 4.2(c)] that are coherently intergrown with small angular mis-orientation around the *c*-axis, which cause changes in the contrast and appearance of the lattice fringes resolved by HRTEM imaging. It is possible that the observed variations in the lattice images along the *c*-axis are caused by stacking defects; it is possible to resolve such features by imaging down the *a*-axis, but this has not been done here due to the unfavorable particle shapes.

Further exploration of the NbS_3 system provided yet another monoclinic NbS_3 polymorph, NbS_3-V. It was prepared at 700 °C with a 30 °C gradient (700 °C source zone → 670 °C growth zone) using 10% excess sulfur for transport. This polymorph also crystallizes in the $P2_1/m$ space group. Additional details are provided in Tables 4.S1 and 4.S2, and crystallographic data have been deposited with the Cambridge Crystallographic Data Centre (structure number 1574382). As illustrated in Fig. 4.1, the unit cell of NbS_3-V is similar to that of NbS_3-I but with a halved *b*-axis; the lattice parameters can be expressed as a', $b'/2$, c', β' based on the NbS_3-I unit cell (Table 1). These dimensions result in two chains per unit cell, albeit the unit cell is only one $[MX_6]$ trigonal prism wide ($Z = 2$). This unit cell is smaller than those proposed for NbS_3-II.

In the chain cross-section of NbS_3-V, three sulfur atoms surround a niobium atom to form acute isosceles triangles with bases composed of 2.020 Å S–S bonds and sides formed by S···S distances of 3.576-3.612 Å. Interestingly, the interchain Nb–S interactions alternate in pairs of 2.619 Å and 2.635 Å Nb–S bonds, which results in a small but measurable chain pairing within the bilayer sheet. Although NbS_3-V features the same ABCDE stacking that occurs in NbS_3-I (Fig 4.1), it contains a single, uniform Nb–Nb distance of 2.358 Å, leading to ideal (non-corrugated) $[MX_6]$ chains. Theoretically, NbS_3 with such an undistorted structure should display metallic conductivity due to a single electron remaining on each Nb^{4+} after creation of the [NbS_6] chains.[23, 38]

NbS_3-IV and -V can be exfoliated in a similar fashion as other MX_3 materials.[5-6, 13] Fig. 4.3 shows HAADF-STEM images of a ~40 nm wide NbS_3-V nanoribbon exfoliated by sonication in ethanol. The high-resolution image in panel B reveals the [NbS_6] chains along the *b*-axis. Both the Nb–Nb bonds with 3.37 Å spacing and the van der Waals gap between chains are clearly visible. There are no defects visible at this magnification in this particular area of the sample or others imaged along this nanoribbon, although the high *wR* value (21.99%) associated with the refinement of NbS_3-V points to the presence of significant structural disorder in the larger crystal used for x-ray diffraction analysis.

In experimental materials research, powder x-ray diffraction (PXRD) is usually the initial characterization method used to identify crystalline phases and evaluate phase purity. The patterns for NbS_3-I, IV, and V are compared in Fig. 4.4(a). Although the theoretical patterns (calculated from single-crystal XRD structures) of NbS_3-I and NbS_3-IV are similar, each has distinct peaks in the range 10-40° 2θ that should make polymorph identification unambiguous. In practice, however, the experimental peak intensities of NbS_3-IV (powder mount) are altered by orientation effects, such that the resulting pattern can be matched to either NbS_3-I or NbS_3-IV. In the case of NbS_3-V, its theoretical pattern is essentially identical to that of NbS_3-I, but experimentally NbS_3-V powder generates a distinct pair of peaks at ~22° 2θ. Thus, we caution that PXRD alone is not sufficient to differentiate between all NbS_3 polymorphs.

Raman spectroscopy provides additional data to differentiate NbS_3-IV and -V. As shown in Fig. 4.4(b), the spectra of these polymorphs are clearly different. However, the spectrum of NbS_3-V is not as clearly resolved as that of NbS_3-IV, which may be due to the structural disorder present. The spectrum of NbS_3-IV is similar but not identical to data published for NbS_3-I.[11,39-40,41] The specific differences are: (1) the relative intensities of the two peaks at 145-155 nm are switched, and (2) the literature spectra for NbS_3-I show a single peak at ~190 nm [assigned as ν(Nb···S_2) in Ref. 38], whereas the spectrum of NbS_3-IV in Fig. 4(b) has two peaks at this position. This latter difference is reasonable based on the asymmetric unit of Nb_2S_6 in NbS_3-IV, which should lead to two distinct ν(Nb···S_2) modes.

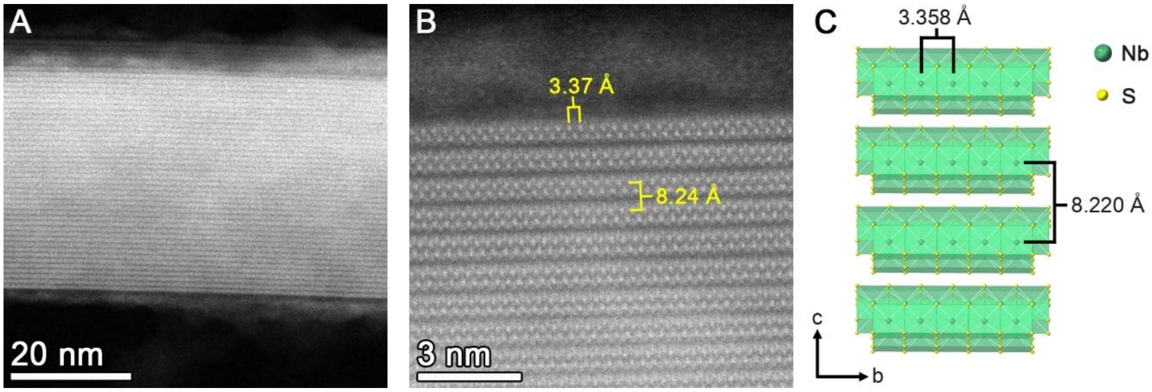

Figure 4.3 HAADF-STEM images of an exfoliated NbS_3-V nanoribbon along the *b*-axis at low (a) and high magnifications (b), together with a structural model for the observed atomic spacings (c).

SEM images [Figs. 4.4(c)-4.4(f)] show that the morphology of NbS_3-IV and -V is fibrous. NbS_3-IV crystals generally appear as wider, straight fibers, whereas NbS_3-V crystals look more like flexible wires. These morphological observations are similar to descriptions of NbS_3-I (larger, straighter needles) and NbS_3-II (finer, bent whiskers) in the literature.[22, 30, 34] In addition to the fibers, both products contain numerous cylinders and rings in various stages of winding/unwinding [Fig. 4.4(d) and 4.4(e)]. Moreover, EDS analysis indicates that these microstructures have a NbS_3

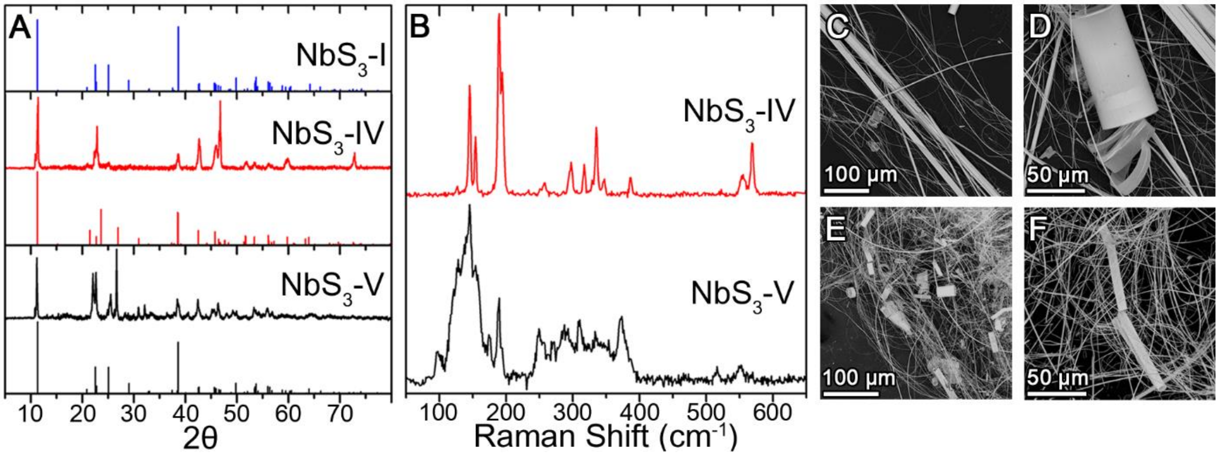

Figure 4.4 (a) Powder x-ray diffraction patterns of NbS_3-I, NbS_3-IV, and NbS_3-V; drop lines for NbS_3-I are from JCPDS card no. 04-007-1130. Powder x-ray diffraction data for NbS_3-IV, and NbS_3-V were collected on a Bruker Advance D8 diffractometer with Co-Kα radiation at 35 kV and 40 mA from 5 – 80 degrees 2θ with a 0.01 step size at 0.4 s/step. (b) Raman spectroscopy of NbS_3-IV and NbS_3-V. Raman data were collected on a Renishaw InVIA microscope at 785 nm with a 50x objective lens. SEM images of NbS_3-IV [(c) and (d)] and NbS_3-V [(e) and (f)]. SEM was conducted on a FEI Teneo FE-SEM instrument equipped with an Oxford Instruments X-MAX^N detector at 5–20 keV.

stoichiometry identical to the fibers. Such "topological crystals," previously observed for TaS_3, $NbSe_3$, and $TaSe_3$, apparently form when droplets of molten elemental chalcogen template crystal growth.[42-44,45-46] Indeed, Enyashin and Ivanovskiĭ have provided a theoretical basis indicating that NbS_3 ring structures are energetically favorable.[47] Continuing work will be required to understand the formation mechanism of such morphologies in the NbS_3 system and characterize the distortions that accompanying crystal bending.

In summary, the crystal structures of two new niobium trisulfide polymorphs, NbS_3-IV and NbS_3-V, greatly enrich our understanding of this system. Both polymorphs crystallize in monoclinic unit cells, which fills a long-standing gap of knowledge about monoclinic NbS_3. We find that the structure of NbS_3-IV is related to triclinic NbS_3-I with respect to Nb–Nb pairing along the chain axis. In comparison, the structure of NbS_3-V is undistorted along the chain axis but contains subtle chain pairing. This structural information will be extremely helpful for the interpretation of spectroscopic data and modeling the electronic properties of NbS_3-IV and NbS_3-V.

Supplemental Information

Table 4.S1 Crystallographic details for NbS_3-IV and -V. Single crystal x-ray diffraction was carried out at room temperature and 100 K on a Bruker D8 Quest PHOTON 100 CMOS X-ray diffractometer with Mo-Kα radiation utilizing a phi and omega-scan technique. 1660 frames were collected using 10 s exposure times.

	NbS_3-IV	**NbS_3-V**
Formula	Nb_2S_6	NbS_3
F.W. (g/mol)	378.18	189.10
Space group	$P2_1/c$ (no. 14)	$P2_1/m$ (no. 11)
Z	4	2
a (Å)	6.7515(5)	4.950(5)
b (Å)	4.9736(4)	3.358(4)
c (Å)	18.1315(13)	9.079(10)
V (Å^3)	608.84(8)	149.7(3)
Absorption coefficient	Numerical	Semi-empirical from equivalents
μ (mm^{-1})	5.684	5.780
θ range (deg.)	3.759 – 25.979	4.151 – 26.002
hkl ranges	$-8 \leq h \leq 8$ $-6 \leq k \leq 6$ $-22 \leq l \leq 22$	$-5 \leq h \leq 6$ $-4 \leq k \leq 4$ $-10 \leq l \leq 10$
No. reflections; R_{int}	1190; 0.0273	318; 0.0485
No. parameters	73	25
R_1; wR_2	0.0351; 0.1138	0.0886; 0.2199
Goodness of Fit	1.060	1.065
Diffraction peak and hole (e$^-$/Å^3)	2.414; -1.686	3.479; -1.241
Temperature (K)	297	100.

Table 4.S2 Atomic coordinates for NbS_3-IV and -V with equivalent isotropic displacement parameters ($Å^2$). U_{eq} is defined as 1/3 of the orthogonalized trace of the Uij tensor.

	NbS_3-IV				**NbS_3-V**			
Atom	x	y	z	U_{eq}	x	y	z	U_{eq}
Nb1	0.4013(1)	0.6367(1)	0.3279(1)	0.003(1)	0.7147(4)	0.7500	0.3483(3)	0.039(1)
Nb2	0.8521(1)	0.6372(1)	0.3233(1)	0.003(1)				
S1	0.1227(2)	0.4335(3)	0.4068(1)	0.007(1)	0.4683(13)	0.2500	0.1738(8)	0.038(2)
S2	0.1237(2)	0.8386(2)	0.4079(1)	0.007(1)	0.8756(12)	0.2500	0.1711(8)	0.035(2)
S3	0.1339(2)	0.6375(2)	0.2277(1)	0.004(1)	0.7606(12)	0.2500	0.5538(8)	0.035(2)
S4	0.6328(2)	0.8336(2)	0.4222(1)	0.008(1)				
S5	0.6332(2)	0.4288(3)	0.4189(1)	0.008(1)				
S6	0.6146(2)	0.6371(2)	0.2181(1)	0.003(1)				

References

1. Kuc, A., Low-dimensional transition-metal dichalcogenides. In *Chemical Modelling: Volume 11*, The Royal Society of Chemistry: 2015; Vol. 11, pp 1-29.

2. Song, X.; Guo, Z.; Zhang, Q.; Zhou, P.; Bao, W.; Zhang, D. W., *Small* **2017**, 1700098-n/a.

3. Zybtsev, S. G.; Pokrovskii, V. Y.; Nasretdinova, V. F.; Zaitsev-Zotov, S. V., *Physica B* **2012,** *407* (11), 1696-1699.

4. Hor, Y. S.; Xiao, Z. L.; Welp, U.; Ito, Y.; Mitchell, J. F.; Cook, R. E.; Kwok, W. K.; Crabtree, G. W., *Nano Lett.* **2005,** *5* (2), 397-401.

5. Jin, Y.; Li, X.; Yang, J., *Phys. Chem. Chem. Phys.* **2015,** *17* (28), 18665-18669.

6. Stolyarov, M. A.; Liu, G.; Bloodgood, M. A.; Aytan, E.; Jiang, C.; Samnakay, R.; Salguero, T. T.; Nika, D. L.; Rumyantsev, S. L.; Shur, M. S.; Bozhilov, K. N.; Balandin, A. A., *Nanoscale* **2016,** *8* (34), 15774-15782.

7. Liu, G.; Rumyantsev, S.; Bloodgood, M. A.; Salguero, T. T.; Shur, M.; Balandin, A. A., *Nano Lett.* **2017,** *17* (1), 377-383.

8. Grisel, A.; Lévy, F.; Wieting, T. J., *Physica B & C* **1980,** *99* (1), 365-370.

9. Island, J. O.; Barawi, M.; Biele, R.; Almazán, A.; Clamagirand, J. M.; Ares, J. R.; Sánchez, C.; van der Zant, H. S. J.; Álvarez, J. V.; D'Agosta, R.; Ferrer, I. J.; Castellanos-Gomez, A., *Adv. Mater.* **2015,** *27* (16), 2595-2601.

10. Poltarak, P. A.; Artemkina, S. B.; Bulavchenko, A. I.; Podlipskaya, T. Y.; Fedorov, V. E., *Russ. Chem. B+* **2015,** *64* (8), 1850-1856.

11. Fedorov, V. E.; Artemkina, S. B.; Grayfer, E. D.; Naumov, N. G.; Mironov, Y. V.; Bulavchenko, A. I.; Zaikovskii, V. I.; Antonova, I. V.; Komonov, A. I.; Medvedev, M. V., *J. Mater. Chem. C* **2014,** *2* (28), 5479-5486.

12. Island, J. O.; Molina-Mendoza, A. J.; Barawi, M.; Biele, R.; Flores, E.; Clamagirand, J. M.; Ares, J. R.; Sánchez, C.; van der Zant, H. S. J.; D'Agosta, R.; Ferrer, I. J.; Castellanos-Gomez, A., *2D Mater.* **2017,** *4* (2), 022003.

13. Lipatov, A.; Wilson, P. M.; Shekhirev, M.; Teeter, J. D.; Netusil, R.; Sinitskii, A., *Nanoscale* **2015,** *7* (29), 12291-12296.

14. Yan, Z.; Jiang, C.; Pope, T. R.; Tsang, C. F.; Stickney, J. L.; Goli, P.; Renteria, J.; Salguero, T. T.; Balandin, A. A., *J. Appl. Phys.* **2013,** *114* (20), 204301.

15. Wu, J.; Wong, D.; Liu, H.; Woon-Ming, L.; Liu, L., *RSC Adv.* **2015,** *5*, 9.

16. Jellinek, F.; Brauer, G.; Muller, H., *Nature* **1960,** *185* (4710), 376-377.

17. Kadijk, F.; Jellinek, F., *J. Less-Common Met.* **1969,** *19* (4), 421-430.

18. Kurdi, M.; Marie, A.-M.; Danot, M., *Solid State Commun.* **1987,** *64* (4), 395-399.

19. Mishchenko, A.; Yushina, I.; Fedorov, V., *Zh. Neorg. Khim.+* **1988,** *33* (2), 437-442.

20. Zettl, A.; Jackson, C. M.; Janossy, A.; Grüner, G.; Jacobsen, A.; Thompson, A. H., *Solid State Commun.* **1982,** *43* (5), 345-347.

21. Zybtsev, S. G.; Pokrovskii, V. Y.; Nasretdinova, V. F.; Zaitsev-Zotov, S. V.; Pavlovskiy, V. V.; Odobesco, A. B.; Pai, W. W.; Chu, M. W.; Lin, Y. G.; Zupanič, E.; van Midden, H. J. P.; Šturm, S.; Tchernychova, E.; Prodan, A.; Bennett, J. C.; Mukhamedshin, I. R.; Chernysheva, O. V.; Menushenkov, A. P.; Loginov, V. B.; Loginov, B. A.; Titov, A. N.; Abdel-Hafiez, M., *Phys. Rev. B* **2017,** *95* (3), 035110.

22. Rijnsdorp, J.; Jellinek, F., *J. Solid State Chem.* **1978,** *25* (4), 325-328.

23. Bullett, D. W., *J. Solid State Chem.* **1980,** *33* (1), 13-16.

24. Itkis, M. E.; Nad, F. Y.; Zaitsev-Zotov, S. V.; Lévy, F., *Solid State Commun.* **1989,** *71* (11), 895-898.

25. Itkis, M. E.; Nad, F. Y.; Levy, F., *Synthetic Met.* **1991,** *43* (3), 3969-3972.

26. Wang, Z. Z.; Monceau, P.; Salva, H.; Roucau, C.; Guemas, L.; Meerschaut, A., *Phys. Rev. B* **1989,** *40* (17), 11589-11593.

27. Nasretdinova, V.; Zaitsev-Zotov, S., *Physica B* **2012,** *407* (11), 1874-1877.

28. Cornelissens, T.; Van Tendeloo, G.; Van Landuyt, J.; Amelinckx, S., *Phys. Status Solidi A* **1978,** *48* (1), K5-K9.

29. Boswell, F. W.; Prodan, A., *Physica B & C* **1980,** *99* (1), 361-364.

30. Prodan, A.; Budkowski, A.; Boswell, F. W.; Marinkov, V.; Bennett, J. C.; Corbett, J. M., *J. Phys. C Solid State* **1988,** *21* (23), 4171.

31. Roucau, C., *J. Phys. Colloques* **1983,** *44* (C3), C3-1725-C3-1728.

32. Meerschaut, A., *J. Phys. Colloques* **1983,** *44* (C3), C3-1615-C3-1622.

33. Kikkawa, S.; Ogawa, N.; Koizumi, M.; Onuki, Y., *J. Solid State Chem.* **1982,** *41* (3), 315-322.

34. Pokrovskii, V. Y.; Zybtsev, S. G.; Nikitin, M. V.; Gorlova, I. G.; Nasretdinova, V. F.; Zaitsev-Zotov, S. V., *Phys.-Usp.+* **2013,** *56* (1), 29.

35. Guilmeau, E.; Berthebaud, D.; Misse, P. R. N.; Hebert, S.; Lebedev, O. I.; Chateigner, D.; Martin, C.; Maignan, A., *Chem. Mater.* **2014,** *26*, 7.

36. van Smaalen, S., *Phys. Rev. B* **1988,** *38* (14), 9594-9600.

37. Bolotina, N. B.; Gorlova, I. G.; Verin, I. A.; Titov, A. N.; Arakcheeva, A. V., *Crystallogr. Rep.+* **2016,** *61* (6), 923-930.

38. Endo, K.; Ihara, H.; Watanabe, K.; Gonda, S.-I., *J. Solid State Chem.* **1981,** *39* (2), 215-218.

39. Sourisseau, C.; Cavagnat, R.; Fouassier, M.; Maraval, P., *J. Raman Spectrosc.* **1990,** *21* (6), 337-349.

40. Sourisseau, C.; Cavagnat, R.; Fouassier, M.; Maraval, P., *J. Mol. Struct.* **1990,** *219*, 183-188.

41. Zwick, A.; Renucci, M. A.; Carles, R.; Saint-Cricq, N.; Renucci, J. B., *Physica B & C* **1981,** *105* (1), 361-365.

42. Tanda, S.; Kawamoto, H.; Shiobara, M.; Sakai, Y.; Yasuzuka, S.; Okajima, Y.; Yamaya, K., *Physica B: Condensed Matter* **2000,** *284–288, Part 2*, 1657-1658.

43. Matsuura, T.; Tanda, S.; Asada, K.; Sakai, Y.; Tsuneta, T.; Inagaki, K.; Yamaya, K., *Physica B* **2003,** *329–333, Part 2*, 1550-1551.

44. Tsuneta, T.; Tanda, S., *J. Cryst. Growth* **2004,** *264* (1–3), 223-231.

45. Kumagai, G.; Matsuura, T.; Ichimura, K.; Tanda, S., *Physica B* **2010,** *405* (11, Supplement), S284-S287.

46. Tsubota, M.; Inagaki, K.; Matsuura, T.; Tanda, S., *Cryst. Growth Des.* **2011,** *11* (11), 4789-4793.

47. Enyashin, A. N.; Ivanovskiĭ, A. L., *Phys. Solid State+* **2006,** *48* (4), 780-785.

CHAPTER 5

CONCLUSIONS

Conclusions

Low-dimensional materials will continue to become an indispensable part of future electronics as technology progresses toward the nanoscale. These nanoscale applications will require new materials and advanced fabrication techniques to fully explore device capabilities. To date, there are several research areas working toward nanoscale solutions, including medicine, [1-2] computing,[3] and electronics.[4] Low-dimensional materials can be utilized in a variety of applications providing extremely high surface area, with a minimized cross-section, ideal for nanoscale sensors or flexible electronics. Low-dimensional materials, like the 1D and 2D transition metal chalcogenides, will make an important contribution to technological development and innovation by improving upon and replacing conventional materials. Transition metal chalcogenides are of interest due to their electrical and charge density wave properties, as well as their ease of processing. These characteristics make them ideal candidates for a variety of future applications.

In this dissertation, the chemistry and structure of low-dimensional transition metal chalcogenides were explored. Due to their possible use in future electronics applications, the oxidative stability of $1T$-$TiSe_2$ and $1T$-$TaSe_2$ were characterized at various temperatures in chapter II. Additionally, the various phase transitions of $1T$-$TaSe_2$ were characterized between room temperature and 1000 °C in chapter III. Beyond 2D chalcogenides, the structures and chemistry of two new polymorphs of NbS_3 are characterized in chapter IV.

The studies defined in chapter II investigate the transport agent concentrations during synthesis as well as the oxidative properties of 1*T*-$TiSe_2$ and 1*T*-$TaSe_2$. This information is vital for future electronics applications due to the dramatic differences in conductivity between the transition metal chalcogenide, and the corresponding metal oxide. Our studies find a significance to the concentration of transport agent used in chemical vapor transport reactions. A concentration range between 3 and 5 mg/cm^3 was found to be ideal for successful vapor transport with little to no observed iodine doping on approximately one quarter of the observed crystals. Above this range, small, rod-like crystals were observed at the edges ~85% of the examined crystals. These small rod-like crystals contained nearly 10 atomic % iodine. Therefore, transport agent concentration is an important consideration to produce high-quality crystals during chemical vapor transport crystal growth reactions.

This study also explored the oxidative behaviors of 1*T*-$TiSe_2$ and 1*T*-$TaSe_2$ at elevated temperatures. Both materials experience the onset of oxidation at similar temperatures, ~300 °C, however, further temperature elevation reveals the varied stability between these two systems. The $TaSe_2$ system was found to have a higher oxidative stability than $TiSe_2$. This conclusion is supported by the temperature at which each fully oxidizes: 400 °C for 1*T*-$TiSe_2$ and 600 °C for 1*T*-$TaSe_2$. Oxidation was found to commence at defect and edge sites most likely due to the coordinately unsaturated metal atoms. The lack of full coordination makes these atoms less energetically stable and, thus, more reactive towards ambient oxygen. The stability of the $TaSe_2$ system is further helped by the presence of polymorphs more stable than the 1*T* phase.

During these studies, $TaSe_2$ polymorph transitions were observed. The crystals first transitioned from 1*T* to 3*R*-$TaSe_2$, and then from 3*R* to 2*H*-$TaSe_2$. The presence of the 3*R* and 2*H* phases most likely limited oxidation to some extent due to their stability at the observed temperatures. This phase stability, however, was eventually overcome resulting in the complete oxidation of the examined crystals. A 4-month, ambient study supports this conclusion with the observation of oxidation, 2*H*-$TaSe_2$ and 1*T*-$TaSe_2$. The 2*H* polymorph was found only near the surface just below an oxide layer; 1*T*-$TaSe_2$ remained beneath these two layers, easily obtained through mechanical exfoliation. The oxide/2*H*-$TaSe_2$ surface implies that some surface passivation is taking place, effectively protecting the 1*T* polymorph below. The presence of lower-temperature-stable polymorphs and their effective surface passivation increase the oxidative stability of the $TaSe_2$ making the systems more stable towards oxidation than the $TiSe_2$ system.

Oxidative behavior studies on transition metal chalcogenides are an important area of study. Future studies could be extended to other polymorphic systems such as TaS_2, $NbSe_2$ and NbS_2. The TaS_2 and $NbSe_2$ systems would be an interesting comparison to $TaSe_2$ due to the similarities in polymorphic extent and structures, whereas NbS_2 presents a system that sits between $TiSe_2$ (1 polymorph) and the Ta systems (many polymorphs) with two well-known polymorphs.

The observation of polymorph transitions during heating inspired further study of the polymorph transitions in the 1*T*-$TaSe_2$ system in chapter III. Several previously phase transitions were observed, however, a close investigation also revealed two previously unreported polymorph transitions. These newly observed transitions include the 3*R* to 2*H*, and the 2*H* to 4*H*(*x*) polymorph transitions, where $x = a$ or c.

Previous studies have shown a wide stability range of 3*R*-$TaSe_2$ during heating under inert conditions, however, this study definitively shows the 3*R* phase transitioning to 2*H*-$TaSe_2$, analogous to the findings in chapter II. This is a relatively low energy transition as indicated in the DSC data by the low intensity, transition peak. Logically, this transition should be present due to the higher stability of the 2*H* versus the 3*R* phase. *Ex situ* Raman spectroscopy conclusively shows the two-step transition from 1*T* to 3*R* to 2*H*-$TaSe_2$, with the Raman spectrum of 3*R*-$TaSe_2$ shown for the first time. With increased temperature, a second small, previously unreported set of transitions were observed at ~635 °C. These two peaks did not fit with previously accepted polymorph transition temperatures. Although, two closely spaced peaks at higher temperature matched with the previously observed 4*H*(*c*) to 4*H*(*b*) polymorph transition.[5] This transition then necessitated the presence of 4*H*(*c*)-$TaSe_2$ indicating that the transition at ~635 °C must correspond with the appearance of this phase. However, two peaks near both transition temperatures imply that two transitions are occurring, thus, the 635 °C transition has been designated as the 2*H* to 4*H*(*x*) polymorph transition encompassing the arrival of both 4*H*(*a*) and 4*H*(*c*). With the techniques used in this study, further transition temperature differentiation between these two transitions was impossible due to the reversibility of the transition. The transition to the 4*H*(*x*) phases results from a slight rearrangement of the layers giving an expanded unit cell, while maintaining the hexagonal symmetry. Transitioning from the 4*H*(*a*) and 4*H*(*c*) polymorphs to 4*H*(*b*)-$TaSe_2$ then commences indicating the lower temperature stability of the octahedral coordination geometry found in the 4*H*(*b*), 6*R*, and 1*T* phases.

Further study is required to distinguish the polymorph transitions from 2*H* to 4*H*(*a*) and 4*H*(*c*)-$TaSe_2$; there has been little study of these phases since their discovery in the 1960's. There has, however, been some reports on 4*H*(*b*)-$TaSe_2$ indicating accessible charge density wave transitions due to the octahedral coordination present in some layers.[6] This same interest could then extend to the 6*R* polymorph, which has also received little attention in the literature. In addition to 6*R*-$TaSe_2$, the 3*R* polymorph has a limited presence in the literature with the electronic and charge density wave properties remaining unexplored. Although, the lack of attention may be due to the difficulty in, not only, obtaining high quality crystals, but also pure 3*R*-$TaSe_2$ samples.

The investigation of polymorphism continues in chapter IV while examining the transition metal trichalcogenide system, NbS_3. NbS_3, the least well-known transition metal trichalcogenide system, previously contained three ill-defined polymorphs. This study details the discovery and characterization of two new polymorphs, designated NbS_3-IV and NbS_3-V. Both polymorphs were found as monoclinic structures with space groups $P2_1/c$ and $P2_1/m$, respectively. These two polymorphs were also found to be structurally similar to the previously reported polymorphs: NbS_3-IV is similar to NbS_3-I, and NbS_3-V is similar to NbS_3-II.

NbS_3-I and IV both possess alternating short and long Nb-Nb distances implying that intrachain Nb-Nb bonding is present resulting in corrugated, structural chains. This, in turn, indicates a semiconducting nature like that found in NbS_3-I. These two structures differ however in their symmetry. The structural layers are arranged in different orders which results in varied crystal symmetry. Layer stacking in NbS_3-IV results in a higher monoclinic (versus triclinic) symmetry and a larger unit cell with a doubled *c*-axis relative to NbS_3-I. High-resolution microscopy also showed that this polymorph experienced twisting around the *a*-axis of the fiber as well as exhibited structural defects and dislocations. An investigation of the structure reveals the van der Waals gap to be perpendicular to the [001] direction, however, the analyzed Fast Fourier Transform (FFT) indicates that the view is down the [010], a counterintuitive observation. Close inspection of the same and other NbS_3-IV particles, however, shows the expected planes implying that the studied fiber was twisting. The fiber twisting exemplifies the flexibility of this quasi-1D material. Further study of the defects and dislocations, however, was impeded by intergrown zones within the crystals. Cross-sectional microscopy is needed in a future study to further characterize these crystal defects.

The NbS_3-V structure is quite similar to the proposed structures for NbS_3-II. Unlike NbS_3-I and IV, only a single Nb-Nb distance is evident within the structural chains resulting in no Nb-Nb pairing and noncorrugated chains. High-resolution microscopy of this polymorph showed similar fiber twisting. The fiber observed under HR-STEM matched well to the {100} plane, perpendicular to the van der Waals gap in the structure. This implies that a degree of fiber twisting was observed analogous to that seen in NbS_3-IV.

With polymorphism, differentiation between phases is a necessity. Interestingly, powder x-ray diffraction was unable to differentiate between these two phases; the structural variations are too slight. Scanning electron microscopy revealed minor differences in fiber widths: NbS_3-IV was generally observed as wider than NbS_3-V. Although, the best technique for polymorph NbS_3 polymorph differentiation is Raman spectroscopy. The two spectra vary significantly making for easy polymorph distinction, however, local heating of NbS_3-V was observed transforming it to NbS_3-IV. Thus, NbS_3-IV is the lower-temperature-stable phase evidenced by the local heating in Raman spectroscopy and the lower synthesis temperature, whereas NbS_3-V requires higher synthesis temperatures and is the less stable polymorph of these two.

The NbS_3 system still requires further study with many more polymorphs possible. Within the scope of these two polymorphs however, more study is required for proper NbS_3-V synthetic parameters as well the reproducible synthesis of NbS_3 tubes and rings. These tube and ring topologies could provide fascinating platforms for closed system, charge density wave investigation. Beyond NbS_3, there is only one other known transition metal trichalcogenide that exhibits polymorphism: TaS_3. Much like NbS_3, the TaS_3 system is structurally ill-defined. Of the two known polymorphs, the monoclinic phase is the only phase to have a defined crystal structure, while the orthorhombic structure remains unclear. TaS_3 represents another structurally interesting system that also exhibits charge density waves and metallic conductivity for specific polymorphs.

This dissertation has described the chemistry and structures in various, low-dimensional transition metal chalcogenide systems. The oxidation characteristics were established for 1*T*-$TiSe_2$ and 1*T*-$TaSe_2$, including oxidation onset at elevated temperatures, oxide layer thickness, and any associated polymorph transitions. Polymorphism was studied in the $TaSe_2$ and NbS_3 systems. Polymorph transitions were followed for 1*T*-$TaSe_2$ revealing previously unreported transitions, whereas the structures of two new polymorphs were established for NbS_3. These studies further our knowledge of low-dimensional transition metal chalcogenides enabling viable device studies in the future.

References

1. Huang, X.; El-Sayed, M. A., *J. Adv. Res.* **2010,** *1* (1), 13-28.
2. Cabuzu, D.; Cirja, A.; Puiu, R.; Grumezescu, A. M., *Curr. Top. Med. Chem.* **2015,** *15* (16), 1605-1613.
3. Zhang, G.; Tateno, K.; Gotoh, H.; Sogawa, T., *NTT Tech. Rev.* **2010,** *8* (8), 7.
4. Stolyarov, M. A.; Liu, G.; Bloodgood, M. A.; Aytan, E.; Jiang, C.; Samnakay, R.; Salguero, T. T.; Nika, D. L.; Rumyantsev, S. L.; Shur, M. S.; Bozhilov, K. N.; Balandin, A. A., *Nanoscale* **2016,** *8* (34), 15774-15782.
5. Huisman, R.; Jellinek, F., *J. Less-Common Met.* **1969,** *17* (1), 111-117.
6. Olaoye, O.; Erasmus, N.; Haupt, K.; Schwoerer, H., *J. Phys. B-At. Mol. Opt.* **2016,** *49* (6), 064011.